On the Creation and Measurement of Rare Isotopes

or,

How Rare Is Rare?

`A Practical Guide to Cross Sections at the Limits of Stability`

Shane Watters[*]

on behalf of the Rare Isotope Research Group

Version 1.1.5 from February 25th, 2026

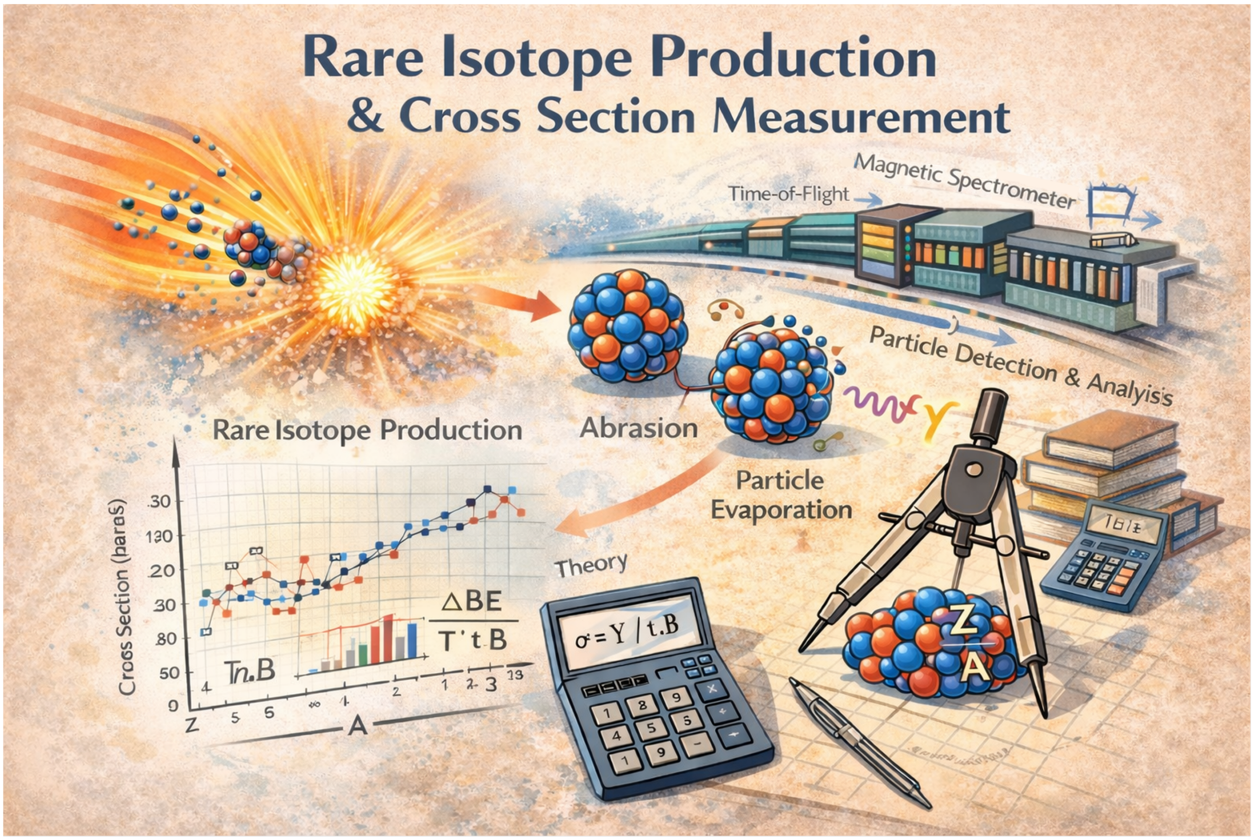

ChatGPT's Graphical Summary of this Manual

FRIB

ARIS
The Advanced Rare Isotope Separator

NSF

---

[*] watterss@frib.msu.edu

Contents

1 Introduction

The purpose of this manual is to guide researchers through the complete analysis of rare isotope production cross sections. The workflow described here is designed to be sufficiently detailed that a new investigator, with a background in nuclear physics, can carry out a full analysis independently, while also serving as a practical reference for experienced users. The procedures are tailored to in-flight rare isotope production experiments employing magnetic fragment separators and event-by-event particle identification.

Although the methodology is broadly applicable to in-flight separator systems, this manual has been developed specifically for use with the Advanced Rare Isotope Separator (ARIS) [1, 2]. As such, ARIS provides the concrete implementation context for the concepts discussed throughout. Examples are drawn from its operation wherever specificity clarifies the discussion. A schematic overview of ARIS is shown in Figure 1, and a detailed discussion of its optics is provided in Appendix C.

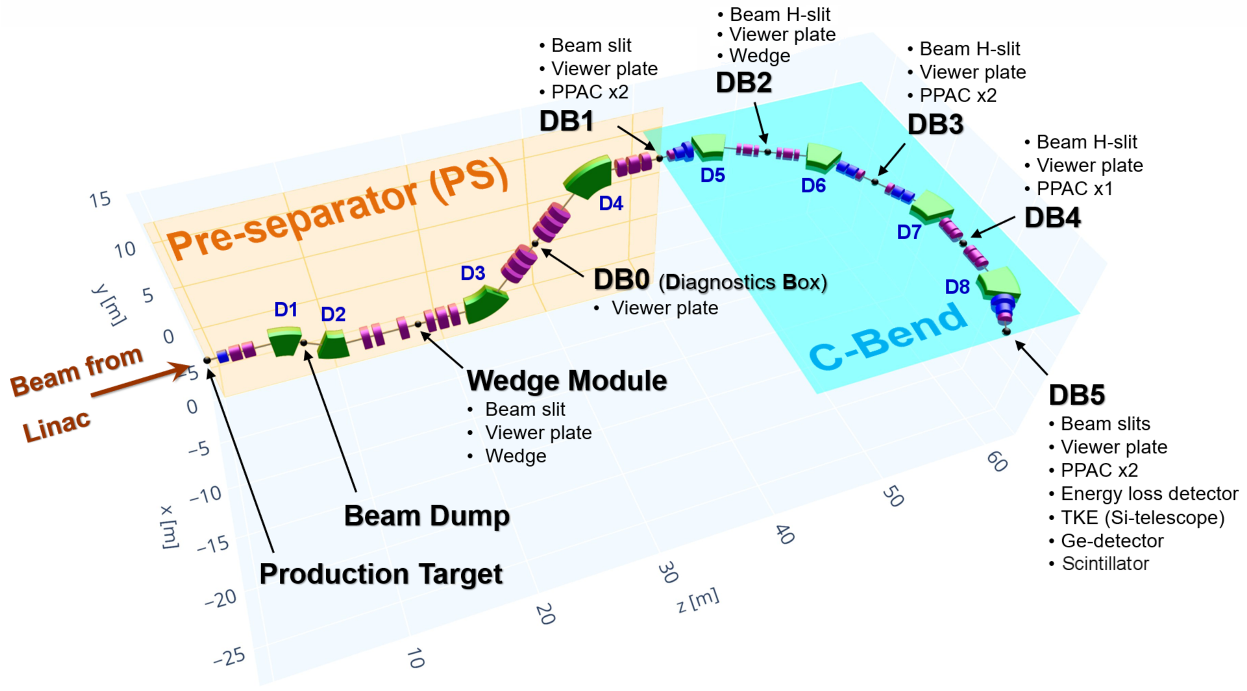

Figure 1: A schematic overview of the Advanced Rare Isotope Separator. Detector and material locations are shown.

The extraction of rare isotope production cross sections is inherently multi-stage and interdisciplinary. It requires careful integration of detector calibration, data cleaning, ion optics, nuclear reaction modeling, and statistical uncertainty analysis. This manual assumes familiarity with foundational techniques such as energy loss, magnetic rigidity, and time-of-flight methods, but does not assume prior experience with this specific analysis framework. First-time analysts are strongly encouraged to read the manual in its entirety before beginning the analysis in order to understand the overall structure and interdependence of the individual stages.

Because each stage builds upon the previous one, errors introduced early in the analysis can propagate forward and significantly affect the final cross sections. Accordingly, this manual emphasizes not only the procedural steps required to complete the analysis, but also the physical reasoning underlying each step. The sequence of operations is intentional: later stages rely critically on the stability, calibration quality, and physical validity established earlier in the workflow.

The manual is organized into five overarching components that mirror the natural progression from raw data to physics interpretation:

1. Experimental data calibration and cleaning,
2. Extraction of experimental parameters,
3. Transmission analysis,
4. Cross section calculation and uncertainty propagation, and
5. Interpretive analysis of the extracted cross sections.

Implementation details that are not essential to understanding the analysis logic are deferred to the appendices. References to external documentation and published resources are provided throughout for readers who wish to explore specific methods in greater depth.

1.1 Data Analysis Workflow

At a high level, rare isotope production cross section analysis proceeds through the following sequence:

1. Raw experimental data are calibrated to convert detector signals into physically meaningful observables, including magnetic rigidity, time-of-flight, energy loss, and total kinetic energy.
2. A series of physics-motivated gates is applied to remove nonphysical events and background contributions while preserving true reaction products.
3. Cleaned and calibrated particle identification spectra are used to extract elemental and isotopic yields.
4. Transmission corrections are applied to account for ion-optical acceptance, reactions in materials, charge-state effects, and higher-order transport effects that are not directly accessible in the experimental data.
5. Production cross sections are calculated from the corrected yields, and uncertainties are propagated to obtain final error estimates.

The remainder of this manual follows this sequence explicitly. Each section explains both how a given analysis step is performed and why it is necessary, with particular attention paid to common failure modes and sources of systematic uncertainty.

Appendix A and Appendix B provide software startup instructions and user-interface references that are used throughout the text; these appendices are recommended reading for first-time analysts. This manual does not attempt to document the full functionality of `SpecTcl`[1], `SpecTk`[2], or `LISE`$^{++}$[3]. Instead, it presents a validated and reproducible analysis pathway for extracting physically meaningful production cross sections.

2 Experimental Data Analysis

The purpose of the experimental data analysis is to transform raw detector signals into clean, calibrated fragment yields suitable for cross section (σ) extraction. This stage forms the foundation of the entire analysis chain. Errors introduced here propagate directly into transmission estimates and, ultimately, into the reported cross sections.

The analysis is performed using `SpecTcl` and `SpecTk`, which together provide tools for histogramming, gating, calibration, and yield extraction. Although these programs are highly flexible, the procedures outlined below define a standard, reproducible workflow that should be followed unless a a compelling experimental reason dictates otherwise.

2.1 Overview of the Workflow

At a high level, the experimental data analysis proceeds through the following steps:

1. Launch `SpecTcl` and `SpecTk` and load the appropriate experiment configuration files.
2. Verify detector readout integrity and establish diagnostic spectra.
3. Perform detector calibrations (timing, position, energy, and charge).
4. Apply physics-motivated data-cleaning cuts to remove unphysical or corrupted events.
5. Construct particle identification (PID) spectra.
6. Extract fragment yields and associated statistical uncertainties.

Before beginning the analysis, ensure that both `SpecTcl` and `SpecTk` are installed and configured correctly. Startup instructions are provided in Appendix A, and user interface basics are presented in Appendix B.

Start `SpecTcl` from the command line. Once `SpecTcl` is running, launch `SpecTk` and connect it to the active session.

Upon successful connection, verify that:

- Spectra can be created and updated,
- Event rates appear reasonable,

---

[1] FRIBDAQ and SpecTcl documentation are available at `https://docs.frib.msu.edu/daq/newsite/index.php`.

[2] SpecTk documentation is available at `https://lise.frib.msu.edu/spectk/spectk_home.html`.

[3] `https://lise.frib.msu.edu/lise.html`

- No error messages related to missing parameters or channels are present.

Any unexpected errors at this stage must be resolved before proceeding. Many downstream analysis problems originate from configuration or mapping issues introduced here.

Additional analysis failures can arise from subtle issues introduced early in the workflow, such as incomplete data cleaning, miscalibrated timing offsets, or residual kinematic correlations. These often manifest later as poor PID separation, unstable Gaussian fits, or anomalous transmission behavior. For this reason, each step should be validated before moving to the next.

2.2 Data Calibration and Cleaning

Once `SpecTcl` and `SpecTk` are running and the experimental data have been loaded, calibration begins. At minimum, this includes magnetic rigidity ($B\rho$), time-of-flight (ToF), and total kinetic energy (TKE). These observables directly determine the reconstructed particle identification parameters A/q and Z, whose relationships are summarized in Appendix E.

Calibration steps must be performed in a consistent order, since later stages depend implicitly on earlier ones. In particular, magnetic rigidity and time-of-flight must be stable before attempting total kinetic energy calibration. The quality of these calibrations ultimately determines the reliability of the extracted fragment yields.

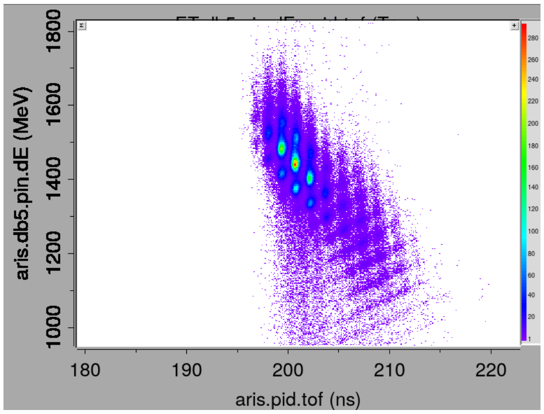

Figure 2: Example of an uncleaned and uncalibrated particle identification plot.

The process of calibration converts raw electronic signals into physically meaningful quantities such as time-of-flight, position, and energy-loss. Calibration procedures vary by detector type but generally follow the same principle: known reference points are used to define a transformation from raw channels to physical units. An example of converted (but uncalibrated) detector output (time-of-flight in nanoseconds and energy-loss in MeV) is shown in Figure 2. Note that the blobs are ambiguous in their identity. The goal of PID is to increase the resolution and to determine who they are.

All calibration files are kept in the `calibration` folder, locally inside the `SpecTcl` build. The exception is the `brho_raw.csv` file, which is shared across builds. This file should not be modified unless the user is confident in the validity of the changes. This file sets the baseline $B\rho$ used in all calculations. Exploratory modifications should be performed on a local copy, with the file path updated in `/calibrPID/brho.tcl`.

A valuable diagnostic tool during detector calibration is the ARIS scaler report. During data acquisition, scaler readouts record the integrated rates of selected detector and logic channels over the duration of a run. Each scaler counts the number of times a specified logic signal – typically the output of a discriminator, trigger, or coincidence condition – fires within the scaler gate. Because scalers are generally free-running and insensitive to

DAQ dead time, they provide a robust means of monitoring detector performance, trigger stability, and overall run conditions. It is important to note that the scalers represent time-integrated rates rather than event-by-event measurements and do not contain energy, timing, or correlation information. Accordingly, scaler values should be routinely monitored both online and during post-experiment analysis. These reports may be accessed from `/user/arisdaq/vme/ARISscaler`.

2.2.1 Magnetic Rigidity Calibration

The first observable to calibrate is the magnetic rigidity, $B\rho$. Rigidity is a primary component of the reconstructed mass-to-charge ratio A/q, which, together with atomic number Z and charge-state q, uniquely identifies each fragment.

After verifying that the raw magnetic rigidities correspond to the measured dipole magnetic fields for the run, trajectory reconstruction corrections must be applied. These corrections compensate for first-order optical correlations between position, angle, and rigidity. A detailed discussion of the underlying ion optics is provided in Appendix C. The reconstruction is obtained using transfer matrices calculated in the `LISE`$^{++}$ extended configuration.

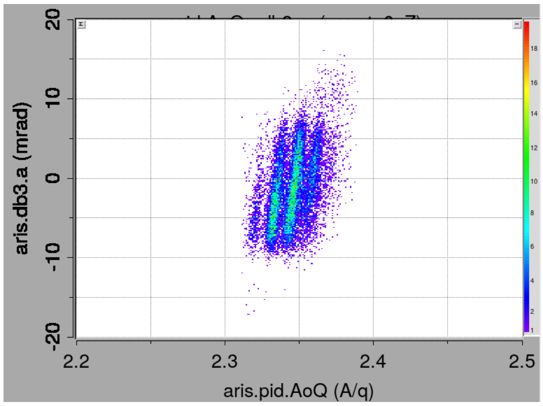

Figure 3: A/q vs DB3 x-angle before kinematic corrections are applied.

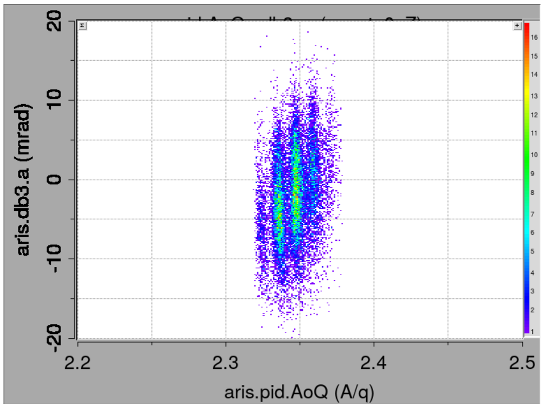

Figure 4: A/q vs DB3 x-angle after kinematic corrections are applied.

2.2.1.1 Trajectory Reconstruction Transfer Matrices

The extended configuration is distributed in the `LISE`$^{++}$ package (`/examples/FRIB/eARIS/eL_ARIS_k3cb2`). Configure the extended file to match the experimental setup[4].

Once the general experimental parameters are set, load an experimental saveset into the extended configuration. Savesets contain snapshots of the magnet settings at a given time (e.g., during tuning or for a specific run). Savesets are currently saved in `/departments/ARIS /info/FTC_ARIS`.

The extended configuration is now ready to calculate the transfer matrices between Diagnostic Boxes (DBs) 3-4 and DB4-5. In the main `LISE`$^{++}$ window, click `Experimental Settings` → `Optics` → `Calculate matrix`

---

[4] The information can be found in an experimental planning `LISE`$^{++}$ file. Parameters to set include primary beam, energy, fragment of interest, target thickness and composition, wedge thickness(es) and composition, and detectors.

`between two selected blocks`. In the dialog box that appears choose the starting and ending points for the transfer matrix calculation. For DB3-4, use DB3 PPAC 1 to DB4 PPAC0; for DB4-5, use DB4 PPAC0 to DB5 PPAC 1[5]. Convert these matrix elements into a form that SpecTcl can read; previous examples are located inside the SpecTcl calibration folder: `/calibrPID/matrix`.

2.2.1.2 Implementing Kinematic Corrections

To enable the kinematic corrections to $B\rho$, change the `Brho_method` in the `/calibrPID/CSV/pid_values` spreadsheet. Multiple $B\rho$ reconstruction methods have been implemented in `SpecTcl` to mitigate sensitivity to detector resolution and optical aberrations at different focal planes. Method 34 utilizes the matrix between DB3-4, while method 45 utilizes the matrix between DB4-5.

Start with method 34. Reload the experimental data in `SpecTcl` and gate on an individual Z line in the PID plot (Z vs A/q)[6]. Apply this gate to the position and angle vs A/q plots and look for any correlation in the plots at the focal planes.

Proper kinematic correction removes first-order correlations, producing vertical distributions in A/q versus position or angle with minimal residual structure. If the `LISE`$^{++}$ matrix elements do not perfectly negate the first-order correlations, adjust the matrix elements until the correlations disappear. An example of before and after kinematic corrections are applied is shown in Figures 3 and 4, respectively.

Sometimes, there exist second-order aberrations in the data. These are non-linear residual curvatures that usually manifest as tails on the ends of the data, forming a ‘C’-shape. Second-order corrections can be applied to the data. In order to enable them, change the value of ‘fine’ column in the `pid_values` spreadsheet from 0 to 1. Next, make adjustments in the spreadsheet `pid_fine_values` to correct for the aberrations. It is important that these corrections are generally small – on the order of 10^{-4} or less.

As the kinematic corrections are applied and refined, the A/q resolution should increase (that is, the sigma of the blobs should decrease). Once `brho_method` 34 is refined, move to method 45 and repeat the process. After refining both methods, take their average with method 345. This average will further enhance the resolution of A/q (if both 34 and 45 are well-behaved). Figures 6 and 7 show the increased resolution between method 1 and method 345.

If either method 34 or 45 is unsuitable for the analysis at hand, use only the well-behaved method. In instances where neither is appropriate (e.g., when the DB4 PPAC is not used), default to method 1, which sets all particle rigidities to the measured value at DB5.

2.2.2 Time-of-Flight Calibration

Time-of-flight (ToF) is the second measured component of the mass-to-charge ratio A/q. It is calibrated between DB3 and DB5 using detector pairs selected for optimal timing resolution.

---

[5] See `https://lise.frib.msu.edu/work/SpecTcl/ARISmatrices_withLISE.pdf` for an illustrated guide.

[6] The element with the brightest blobs is usually recommended, regardless of whether or not it contains the fragment of interest.

The locations of detectors along the beam path are stored in the `/calibrPID/locations.tcl` file. SpecTcl automatically calculates the path length between pairs of given detectors; this quantity is held fixed for the purposes of the time-of-flight analysis.

When multiple independent timing measurements are available, they should be averaged to improve resolution. Each detector provides an estimate of the same physical quantity – the particle's flight time – but is subject to uncorrelated statistical fluctuations arising from detector response, electronics jitter, and signal processing. Averaging suppresses these random fluctuations, reducing the timing uncertainty approximately as $1/\sqrt{N}$ for N **independent** measurements.

The increased resolution of the particle identification when an averaged ToF method is used is shown in Figures 5 and 6. Note that the PID shifts due to calibration differences between the time-of-flights. Physically, the increased resolution reflects the fact that while any single detector may register an early or late time by chance, it is unlikely that all detectors fluctuate in the same direction by the same amount. Averaging therefore suppresses random timing noise while preserving the true flight time, leading to narrower ToF distributions and improved downstream quantities such as A/q, charge-state separation, and PID resolution.

After new detectors have been installed, it may be of interest to perform a principal component analysis. This analysis estimates the intrinsic timing resolution of the individual detectors after removing the global jitter from the signals. This analysis allows one to see block jitter – the way all detectors on the same module fluctuate relative to others – as well as reveal any other statistical correlation between the detectors. This has the power to reveal improvements that can be made through electronics adjustments. Additionally, this analysis will inform the best signals to combine to reduce the overall ToF variance.

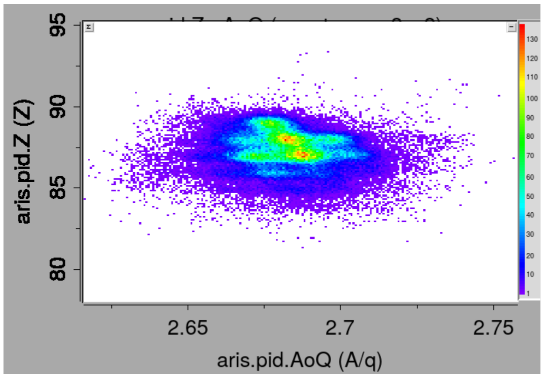

Figure 5: Before kinematic corrections (`Brho_method` 1) with single time-of-flight method. $\sigma(A/q) = 0.0038$.

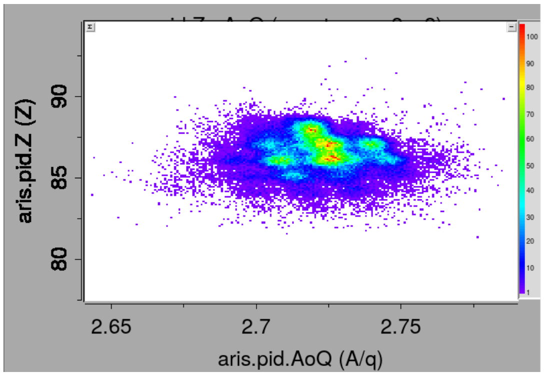

Figure 6: Averaged time-of-flight method used but no kinematic corrections. $\sigma(A/q) = 0.0031$.

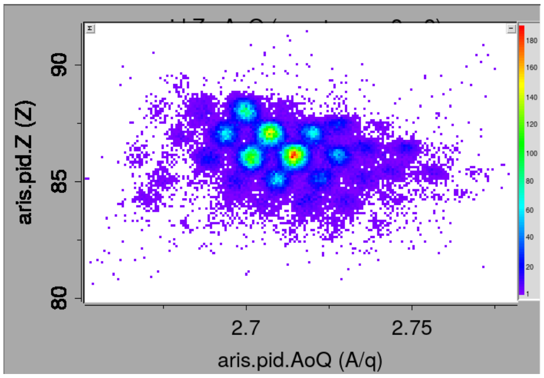

Figure 7: Averaged time-of-flight method and kinematic corrections used. $\sigma(A/q) = 0.0021$.

Alternatively, a brute-force approach may be used in which the standard deviation of every unique combination of detectors is calculated to find the best overall resolution[7].

The timing method to use is specified in the `pid_values` spreadsheet. The various methods of the ToF are defined in the file `/source/CAris_pid/CAris_pid_LenToF.cpp`. New averaged methods may be added with a new index number. Note that `SpecTcl` must be recompiled after changes are made to a .cpp file.

Timing offsets are used to move the measured ToF to agree with physically-reasonable values. These values are determined by a `LISE`$^{++}$ Monte Carlo simulation. Using the pre-configured experimental `LISE`$^{++}$ file, calculate the time-of-flight between DB3 and DB5[8]. Use the mean ToF value as the baseline calibration. Final adjustments will be made as dictated by the particle identification.

To calibrate individual pairs of detectors, use the files `/calibrPID/CSV/tof_offsets`. Once this has been achieved (accuracy need not be perfect), the averaged time-of-flight method may be set in the `pid_values` spreadsheet. Note that the global ToF offset is also located in this sheet and is how the averaged method ToF will be adjusted, if necessary[9].

The final ToF calibration is to ensure that the PID lines up where expected. During beam tuning online, particle identification (PID) should already have been determined[10]. Adjust the global ToF offset to align the PID pattern (A/q vs Z). If PID needs to be performed from scratch, see Appendix E.

2.2.3 Data Cleaning

With PID finalized, the next step is data cleaning. Cleaning is performed by applying physics-motivated gates to remove nonphysical or background events (colloquially referred to as “bad counts”) while preserving true reaction products. There are many ways to remove these bad counts; the ones presented here are the most general. Representative examples of common cleaning gates are shown in Figures 8–10.

These gates constitute a first-pass cleaning and may be refined later as the analysis progresses. It is important to emphasize that over-cleaning can bias yields by preferentially removing valid low-statistics events. Cleaning gates should therefore be as tight as necessary, but no tighter, and should always be validated by inspecting their effect on PID and yield stability. When uncertainty exists, gates should be applied conservatively and adjusted incrementally while monitoring PID stability and yield consistency. Quantitative gate analysis is discussed in Appendix D. The gate analysis is critical for new isotope searches or data sets with many low-statistics fragments.

For high-Z beams, an additional charge-state gate should also be employed after the total kinetic energy calibration; see subsubsection 2.2.4.

---

[7] It should be noted that this becomes infeasible as the number of detectors at both DB3 and DB5 become large. An Excel spreadsheet has been made to calculate standard deviations of up to 5 timing signals.

[8] For quick calibrations, a typical flight time between DB3 and DB5 is approximately 130 ns.

[9] It is good practice to set this value to 0 at the beginning of a new analysis, as this global offset is applied in addition to any local offsets (e.g., detector pair offsets).

[10] This information is located in the Olog: `https://controls.frib.msu.edu/logbook/`

PPAC Sum Gates

Parallel Plate Avalanche Counters (PPACs) play a critical role in event validation due to their detector design and fast signal response. These detectors consist of thin electrodes separated by a narrow gas gap and operated under a strong electric field. When a charged particle traverses the detector, it produces an electron avalanche that results in a prompt electrical signal [3]. The minimal material budget ensures negligible energy-loss and preserves the fragment trajectory[11].

PPACs provide both precise timing and position information. Timing signals are generated at both ends of the readout structure, allowing the construction of a timing sum, typically defined as the sum of the left and right timing signals for a given PPAC [4]. For particles traversing the detector normally and within the active area, this timing sum is approximately constant and largely independent of hit position. As a result, the timing sum serves as a powerful discriminator of valid detector traversal.

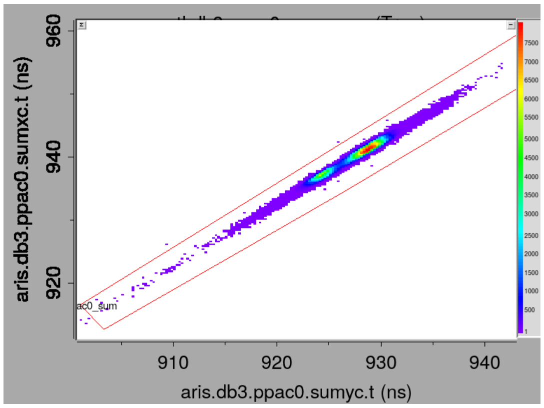

Figure 8: Example of a PPAC sum gate. Valid events lie along the main diagonal.

Events that do not correspond to physically meaningful trajectories are readily identified through deviations in the timing sum. Examples include particles that clip the detector edges, traverse the detector at large angles, scatter upstream, or originate from secondary reactions. Such events often produce delayed, asymmetric, or incomplete signals, leading to broadened or shifted timing-sum distributions. By applying gates on the timing sum, these unphysical events can be efficiently rejected. An example of this is shown in the sum spectra of Figure 8.

When a pair of PPACs is installed at the same focal plane, the particle trajectory angle can be reconstructed from the two position measurements. A particularly powerful diagnostic is the tracking spectrum formed by connecting these two positions, which directly visualizes the reconstructed particle paths between the PPACs. Large-angle particles are readily identifiable in this representation. During beam tuning, this capability provides a fast and intuitive check of the angular distribution of the beam at the focal plane.

When multiple PPACs are installed along the beamline, additional consistency checks become possible. Valid fragments exhibit correlated timing sums and positions across successive PPACs, consistent with the expected transport through the magnetic optics. Events that fail to register in one PPAC, or that show inconsistent timing or position correlations between detectors, are indicative of scattering, charge-changing reactions in degraders, or partial loss of acceptance.

PPAC-based conditions therefore act as geometric and kinematic filters that are largely independent of energy-loss observables. This independence is particularly valuable for high-

---

[11] It is important to note, however, that for high-Z beams, charge-exchange may occur within the gas volume. This can be observed as a difference in the reconstructed momentum between segments 34 and 45, as seen in Figure 10

Z beams and high-rate conditions, where pileup and reaction-induced background are more prevalent. Applying PPAC timing-sum and correlation gates early in the analysis chain suppresses artificial broadening in PID and isotopic spectra and improves the stability of downstream calibrations, including total kinetic energy calibration and yield extraction.

Energy-Loss Gates

Energy-loss gates are applied between successive detectors in the silicon stack to suppress light reaction products and other sources of background that do not correspond to the ions of interest. These gates exploit the fact that, for a charged particle traversing thin layers of material at fixed velocity, the specific energy-loss is determined by its charge and velocity, and is only weakly sensitive to small variations in detector thickness or entrance angle. As a result, identical particles passing through adjacent thin silicon detectors are expected to deposit nearly the same amount of energy in each layer, producing a narrow, correlated locus in ΔE–ΔE space (Fig. 9).

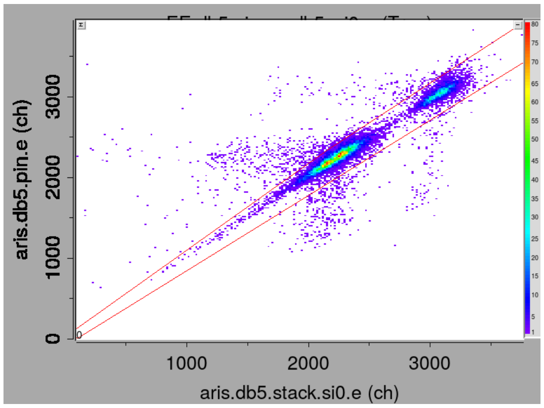

Figure 9: Example of an energy-loss gate. Valid events lie along the main diagonal.

In contrast, light reaction products, scattered beam particles, and partially stopped ions typically exhibit different charge-to-velocity combinations or undergo significant energy degradation between layers, leading to broader or displaced energy-loss correlations. By selecting events consistent with the expected ΔE–ΔE behavior of the isotope of interest, energy-loss gates provide an effective and largely model-independent means of rejecting these backgrounds while preserving high efficiency for fully transmitted heavy ions.

Dispersion Gates

Finally, a dispersion-ratio gate between Dip34 and Dip45 is applied when using the $B\rho$ method 345 to ensure optical consistency of the reconstructed trajectories. In a first-order achromatic beam line, the horizontal position at a dispersive focal plane is proportional to the particle's magnetic rigidity, such that ions with unchanged charge-state and momentum experience the same relative dispersion at successive dipoles. Consequently, the reconstructed dispersions at Dip34 and Dip45 are expected to scale linearly, producing a narrow locus along a 45° line when plotted against one another. This is shown in Figure 10, for many charge-states. The ions whose charge-state changed by the same amount form 45° lines in the spectrum. Both the charge-state and dq are labeled.

Events that deviate from this correlation typically correspond to particles that have undergone nuclear reactions, charge-changing processes, or large-angle scattering between the two dipoles, all of which alter the particle's effective magnetic rigidity and disrupt the expected dispersion matching. By gating on the 45° correlation, the dispersion-ratio cut provides a robust means of rejecting such non-ideal trajectories while retaining ions that are cleanly transported through the spectrometer and are therefore suitable for reliable $B\rho$ reconstruction.

2.2.3.1 Sources of Background in Cleaned Spectra

Even after careful calibration and the application of well-designed cleaning gates, residual background is unavoidable in rare isotope data. Understanding the physical and instrumental origins of this background is essential for interpreting low-statistics yields and for avoiding overly aggressive cleaning.

One common source of background arises from the high-σ tails of neighboring PID peaks. Finite detector resolution in time-of-flight, energy-loss, and magnetic rigidity produces non-Gaussian wings that extend beyond the nominal centroid of each isotope. For fragments with large production cross sections, these tails can populate the PID space of rarer neighboring isotopes, particularly along directions of strong parameter correlation (e.g., A/q–ToF or Z–dE). This effect becomes more pronounced when the yield ratio between adjacent isotopes is large.

Background may also originate from unresolved charge-states. Partially stripped ions can form secondary bands that overlap or intersect the fully stripped PID loci. If not explicitly separated or accounted for, these charge-state contaminants may leak into otherwise well-defined isotope gates, especially at lower velocities or for high-Z fragments.

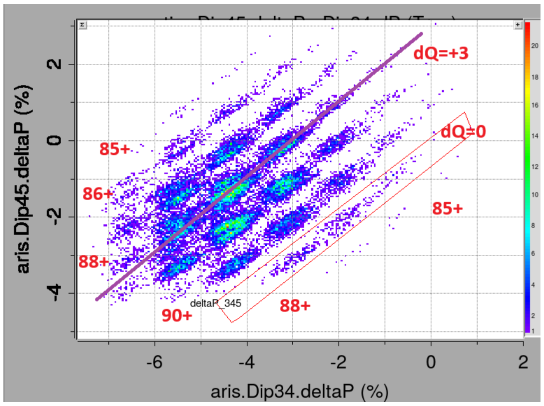

Figure 10: Example of a dispersion gate. The different horizontal and vertical lines represent charge-states. Diagonal lines represent constant charge change.

Secondary reactions in detectors or degraders constitute another irreducible background source. Nuclear interactions within the target, wedge, or detector material can produce fragments that mimic valid PID signatures but do not correspond to direct projectile fragmentation products. These events often populate diffuse regions of PID space and are difficult to remove without simultaneously sacrificing good events.

Finally, random coincidences and electronic effects – such as pile-up, multi-hit ambiguities, or imperfect signal reconstruction – can generate isolated or sparsely populated background events. While these contributions are typically small, they become significant when extracting yields for the most exotic, lowest-cross-section fragments, and are principally why new isotope discoveries require two counts for positive identification [5].

For these reasons, cleaning gates should be designed to suppress dominant background contributions while preserving physically plausible tails of genuine isotope distributions. Residual background is best treated as a systematic contribution to the yield uncertainty rather than eliminated entirely.

2.2.4 Total Kinetic Energy Calibration

Total kinetic energy (TKE) calibration enables charge-state separation and is essential for high-Z beams. TKE calibration should only be performed after PID and data cleaning are stable. In addition, detector bias voltages and detector thicknesses must be verified before proceeding. Failure to address these prerequisites will result in unphysical or meaningless TKE calibrations.

It is critical that the fragments stop before or in the last silicon detector in the stack. Particles that punch through the stack do not yield a valid TKE measurement. Punch-through is readily identified by examining the signal in the last silicon detector: a large population of events with amplitudes comparable to or greater than those in upstream detectors indicates insufficient stopping power. Correcting punch-through requires reducing the fragment energy, either by increasing wedge thickness or by lowering the selected magnetic rigidity, $B\rho$[12].

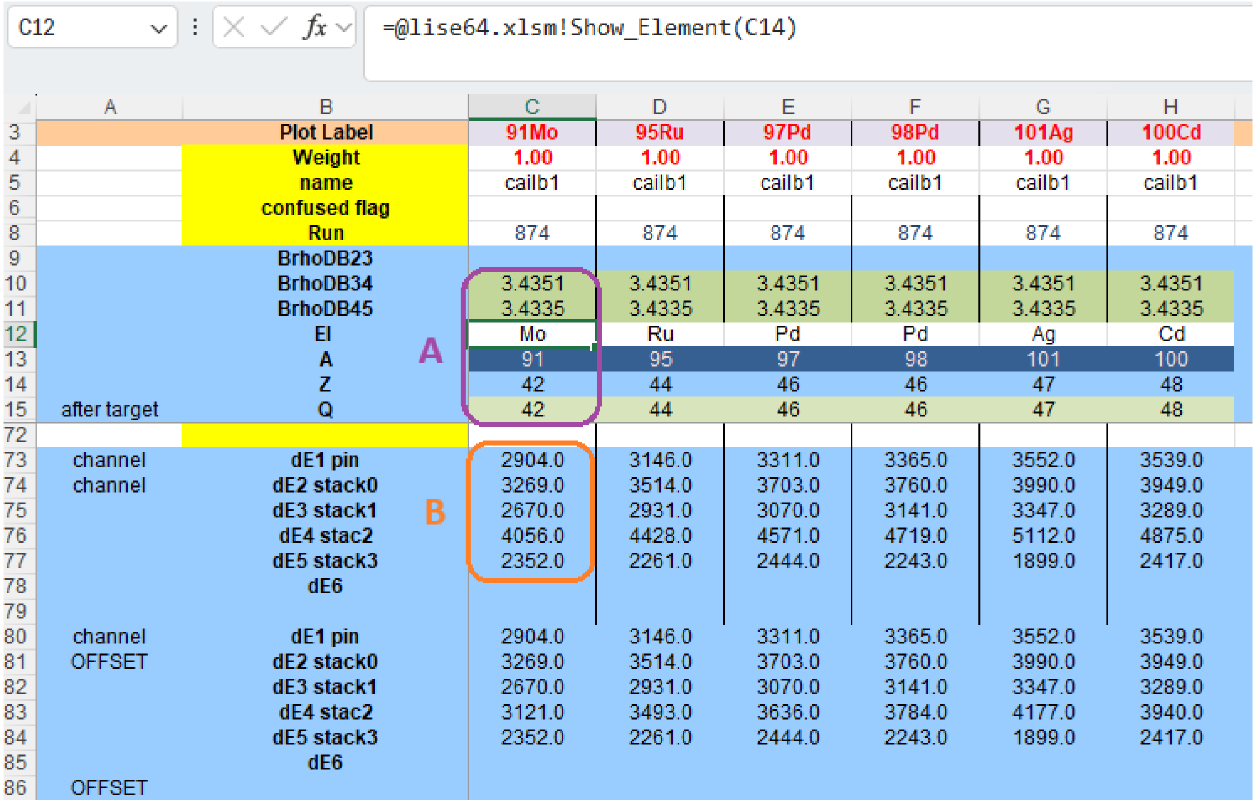

C12

=@lise64.xlsm!Show_Element(C14)

	A	B	C	D	E	F	G	H
3		Plot Label	91Mo	95Ru	97Pd	98Pd	101Ag	100Cd
4		Weight	1.00	1.00	1.00	1.00	1.00	1.00
5		name	cailb1	cailb1	cailb1	cailb1	cailb1	cailb1
6		confused flag						
8		Run	874	874	874	874	874	874
9		BrhoDB23						
10		BrhoDB34	3.4351	3.4351	3.4351	3.4351	3.4351	3.4351
11		BrhoDB45	3.4335	3.4335	3.4335	3.4335	3.4335	3.4335
12		El	Mo	Ru	Pd	Pd	Ag	Cd
13		A	91	95	97	98	101	100
14		Z	42	44	46	46	47	48
15	after target	Q	42	44	46	46	47	48
72								
73	channel	dE1 pin	2904.0	3146.0	3311.0	3365.0	3552.0	3539.0
74	channel	dE2 stack0	3269.0	3514.0	3703.0	3760.0	3990.0	3949.0
75		dE3 stack1	2670.0	2931.0	3070.0	3141.0	3347.0	3289.0
76		dE4 stac2	4056.0	4428.0	4571.0	4719.0	5112.0	4875.0
77		dE5 stack3	2352.0	2261.0	2444.0	2243.0	1899.0	2417.0
78		dE6						
79								
80	channel	dE1 pin	2904.0	3146.0	3311.0	3365.0	3552.0	3539.0
81	OFFSET	dE2 stack0	3269.0	3514.0	3703.0	3760.0	3990.0	3949.0
82		dE3 stack1	2670.0	2931.0	3070.0	3141.0	3347.0	3289.0
83		dE4 stac2	3121.0	3493.0	3636.0	3784.0	4177.0	3940.0
84		dE5 stack3	2352.0	2261.0	2444.0	2243.0	1899.0	2417.0
85		dE6						
86	OFFSET							

Figure 11: Input page (`LISE_eloss`) of the total kinetic energy calibration workbook. The main inputs are the particle identification information (Box **A**) and the mean energy-loss channel for each detector (Box **B**).

A related issue arises from improperly biased detectors. An underbiased detector will saturate, causing most events to accumulate in the overflow bin. This condition is easily corrected by adjusting the detector bias voltage. A discussion and example of improper

---

[12] Assuming, of course, that additional energy-loss detectors cannot be inserted.

detector depletion is given in Ref. [6]. Any change in detector bias invalidates previous energy-loss calibrations, and therefore must be redone after voltage adjustments.

Once proper detector biasing and stopping power is confirmed, TKE calibration may proceed. Conceptually, the TKE calibration enforces consistency between measured detector responses and the expected energy-loss and stopping behavior of identified ions. This approach is also called the “global calibration” [6], as it utilizes all of the experimental parameters (energy loss, time-of-flight, magnetic rigidity and dispersion) and physical constraints to inform the fit. In practice, this means calibrating detector response functions so that reconstructed energies agree with the particle’s trajectory and flight time through the system, along with the well-established heavy-ion stopping calculations. This global approach also permits validation of assumed thicknesses of other materials in the beamline that are not directly measured (e.g., the PPACs or the silicon telescope segments themselves).

The physics-informed approach provides powerful constraints on the calibration. Results that are not physical are greatly suppressed through the weighting that is given to ensure consistency of the other experimental observables.

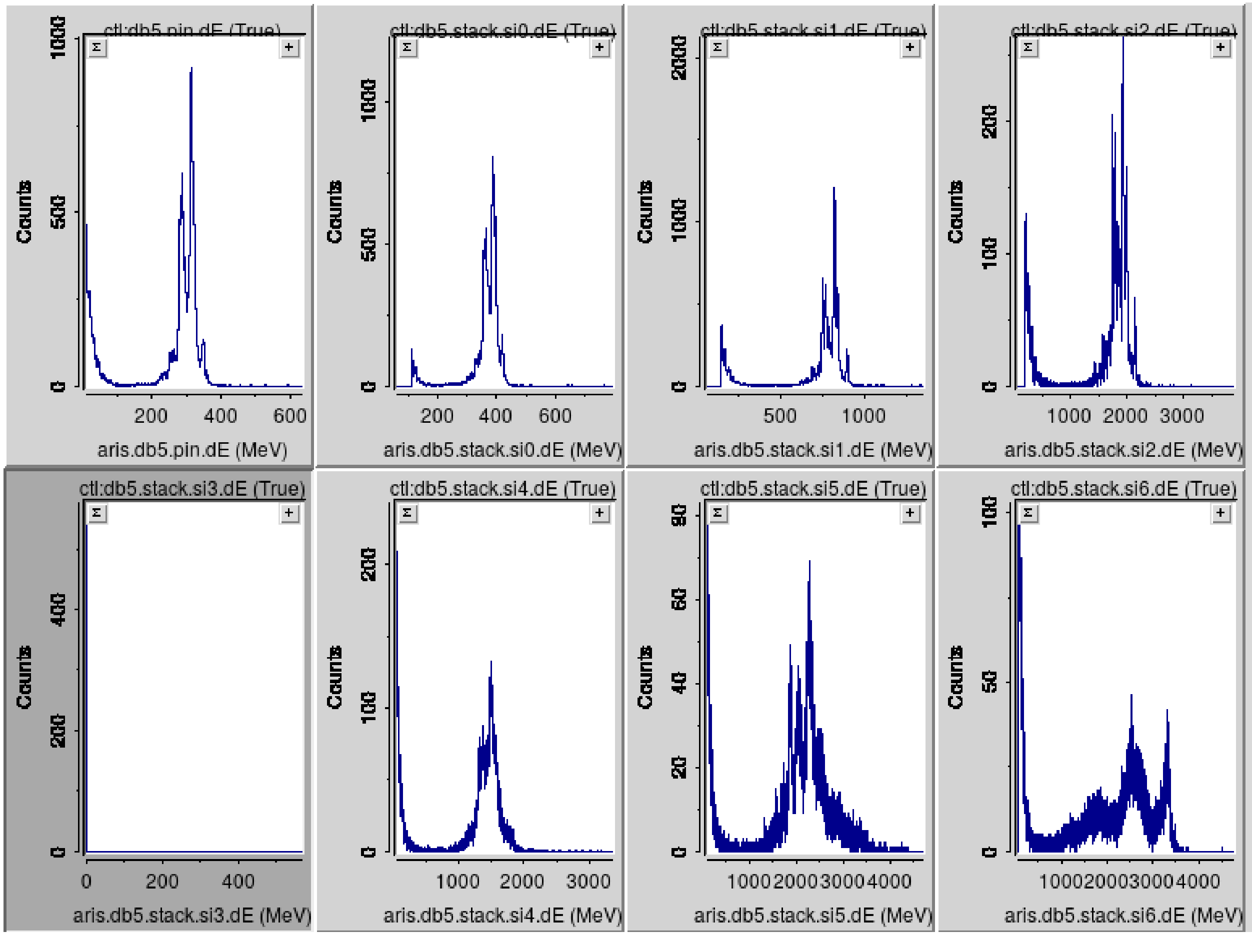

Figure 12: Example of run with invalid energy-loss signals: stack 3 is absent, and it is unclear if the particles stop in the last detector (stack 6)

On the PID spectrum, create 4-6 isotope identification gates spanning the full fragment distribution. These isotope gates, together with the previously defined cleaning gates, are applied to one-dimensional magnetic rigidity and energy-loss spectra to extract average detector channel values for each fragment. Ensure that all detectors registering a valid signal are included, up to and including where the fragment stops[13].

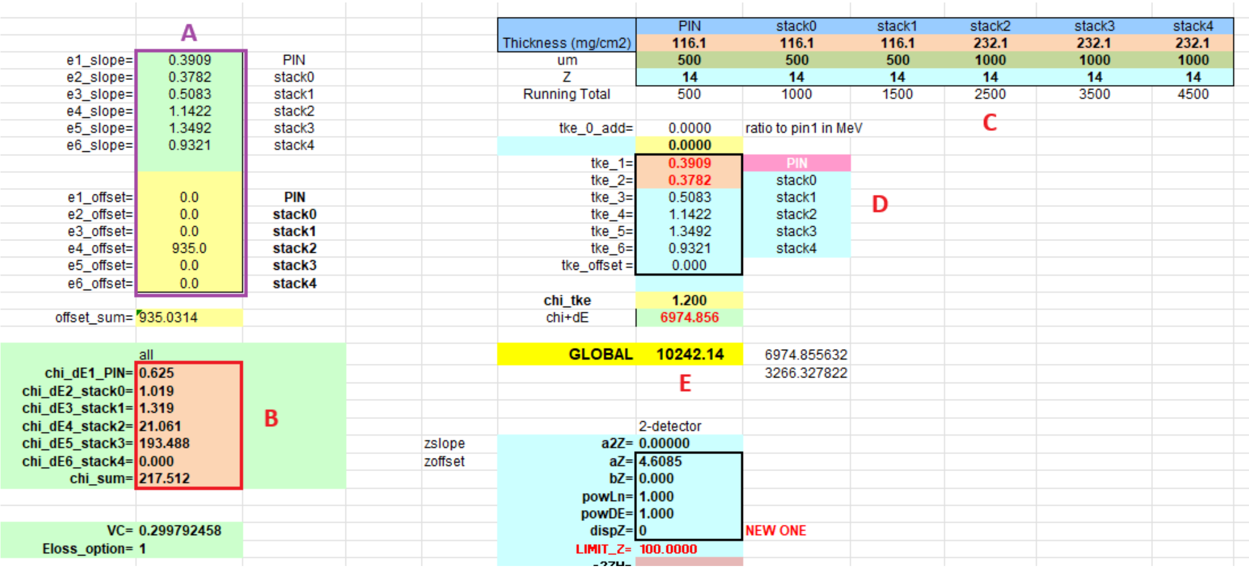

e1_slope= 0.3909 PIN
e2_slope= 0.3782 stack0
e3_slope= 0.5083 stack1
e4_slope= 1.1422 stack2
e5_slope= 1.3492 stack3
e6_slope= 0.9321 stack4

e1_offset= 0.0 **PIN**
e2_offset= 0.0 **stack0**
e3_offset= 0.0 **stack1**
e4_offset= 935.0 **stack2**
e5_offset= 0.0 **stack3**
e6_offset= 0.0 **stack4**

offset_sum= 935.0314

all
chi_dE1_PIN= 0.625
chi_dE2_stack0= 1.019
chi_dE3_stack1= 1.319
chi_dE4_stack2= 21.061
chi_dE5_stack3= 193.488
chi_dE6_stack4= 0.000
chi_sum= 217.512

VC= 0.299792458
Eloss_option= 1

	PIN	stack0	stack1	stack2	stack3	stack4
Thickness (mg/cm2)	**116.1**	**116.1**	**116.1**	**232.1**	**232.1**	**232.1**
um	**500**	**500**	**500**	**1000**	**1000**	**1000**
Z	**14**	**14**	**14**	**14**	**14**	**14**
Running Total	500	1000	1500	2500	3500	4500

tke_0_add= 0.0000 ratio to pin1 in MeV
0.0000
tke_1= 0.3909 PIN
tke_2= 0.3782 stack0
tke_3= 0.5083 stack1
tke_4= 1.1422 stack2
tke_5= 1.3492 stack3
tke_6= 0.9321 stack4
tke_offset = 0.000

chi_tke 1.200
chi+dE **6974.856**

GLOBAL 10242.14 6974.855632
3266.327822

2-detector
zslope **a2Z= 0.00000**
zoffset **aZ= 4.6085**
bZ= 0.000
powLn= 1.000
powDE= 1.000
dispZ= 0 NEW ONE
LIMIT_Z= 100.0000

Figure 13: Fitting page (`parameters`) of the total kinetic energy calibration workbook. Box **A** contains the fitted slope and offset parameters, which are ultimately used in `SpecTcl`.

The TKE calibration is performed using a dedicated Excel workbook that compares measured energy-loss and magnetic rigidity values with expectations calculated by LISE^{++}. The workbook determines detector slopes and offsets that best reproduce the simulated stopping behavior. For correct operation, the `lise64` Excel file must be the first Excel file to be opened; ensure that all macros and external content are enabled. Opening `lise64` while another Excel file is open may cause Excel to crash. The workbook can be found in `"/Program Files/LISEcute/lise64.xlsm"`.

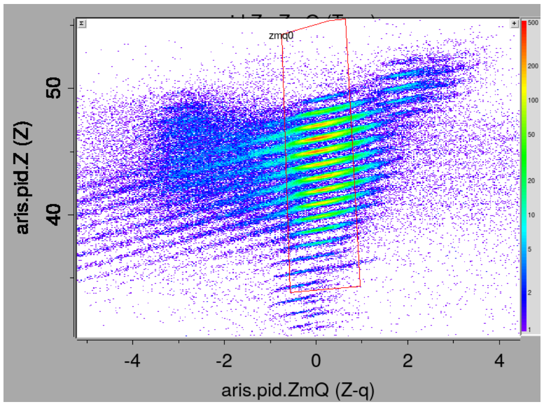

Figure 14: Example of a charge-state gate on fully-stripped ions.

Figure 11 shows an example of the `LISE_eloss` input sheet. The required inputs are highlighted in boxes **A** and **B**. Box **A** contains particle identification parameters and the experimental $B\rho$. Box **B** contains the average channel values from the energy-loss detectors. All remaining cells on this sheet are automatically calculated from these inputs.

---

[13] Detectors downstream of the stopping location do not register physical energy-loss and should not be included.

After entering the inputs, proceed to the `parameters` sheet (Fig. 13), where the minimization that determines the calibration parameters is performed. The objective of the fit is to transform raw detector channels into energy-loss values in a manner that is internally consistent and physically meaningful.

Detailed algorithmic aspects of the fitting procedure are not discussed here. Users are encouraged to examine the worksheet structure by tracing cell precedents and dependencies (`Formulas` → `Trace Precedents`) to better understand how the calibration is constructed.

In Figure 13, Box **A** contains the adjustable slope and offset parameters to be fitted. Box **B** displays the χ^2 values calculated on the `LISE_eloss` sheet. Box **C** must be verified before minimization begins; it specifies the physical thicknesses of the detectors and directly affects the calculated energy-loss. Box **D** is algebraically linked to Box **A** and must not be modified, as downstream calculations reference these cells. Box **E** contains the summed χ^2, which serves as the minimization target.

Minimization should be performed iteratively, reducing one χ^2 component at a time while monitoring the behavior of the `GLOBAL` cell. Using the Excel Solver add-in, minimize the selected χ^2 component by varying the parameters in Box **A**. Repeat this process until the total χ^2 is minimized and stable.

Only detectors that register physical energy-loss for the fragment of interest should be included in the minimization. For example, if fragments stop in silicon detector 3, then silicon detector 4 and beyond must be excluded from the fit.

Once the minimization is complete, copy the resulting calibration parameters into the `SpecTcl` calibration file located at `/calibrPID/CSV/db5_si_values.csv`. Reload the data and verify the calibration by inspecting the $Z - q$ vs Z spectrum. For light-Z beams, a well-defined cluster near zero charge-state difference should appear. An example of a well-calibrated spectrum and associated gate are shown in Figure 14. This gate is applied in subsequent data cleaning to isolate the desired charge-state prior to yield extraction.

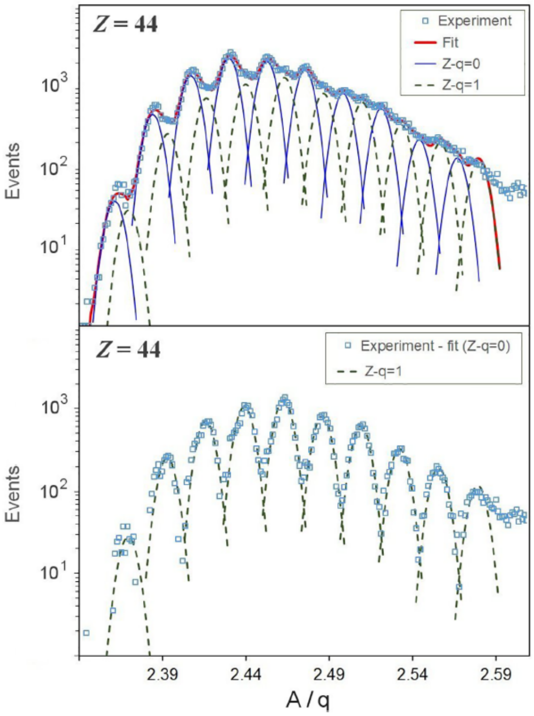

Figure 15: Example of potential charge-state contamination to the yield statistics. From Ref. [7].

The contamination of yields by different charge-states is shown in Figure 15. The analysis of charge-state distributions and locations was performed in Ref. [7]. Without proper removal of charge-state contamination, extracted isotopic yields will be skewed.

Once charge-state separation is complete and final cleaning gates are defined, the analysis proceeds to yield extraction, where elemental and isotopic distributions are quantified.

2.2.5 Z Calibration

The final essential PID variable is the atomic number, Z. This quantity is reconstructed from the particle's energy-loss in the DB5 detectors. The formal relationship used for the calculation is given in Appendix E.3. In practice, the Z calibration is performed concurrently with the total kinetic energy (TKE) and charge-state calibration described in the previous section, since these quantities are coupled through the velocity dependence of the stopping power.

Once the TKE calibration has been established, the elemental blobs in PID space can be translated into their correct physical positions. The detailed identification procedure is described in Appendix E.6. At this stage, adjustments to the Z calibration parameters serve primarily to align the reconstructed PID pattern with known isotopic centroids.

Within the `pid_values` spreadsheet, the calibration parameters are defined explicitly. Equations (30) and (31) show how these parameters enter the reconstruction of the atomic number. In typical operation, $Z_{\log\beta}$ is set to unity and Z_{slope2} is set to zero. The dominant tuning parameters are therefore Z_{slope} and Z_{offset}, which control the overall scaling and translation of the PID pattern in Z. Large adjustments to the offset (greater than approximately 0.5 units in Z) should not be made unless particle identification has been independently confirmed, as they may conceal underlying calibration inconsistencies.

The elemental resolution can also be improved by optimizing the energy-loss input used in the reconstruction. The `pid_values` spreadsheet includes a column specifying the `Z_method`, which determines which energy-loss signal enters Equation (30). In `SpecTcl`, method 0 uses only the PIN detector measurement, while method 1 uses the average of the PIN and silicon stack 0 signals. When both detectors are properly calibrated and functioning reliably, combining their measurements reduces statistical fluctuations and can noticeably improve the elemental peak resolution, as shown in Figure 16. Note that the Z shifts due to calibration differences.

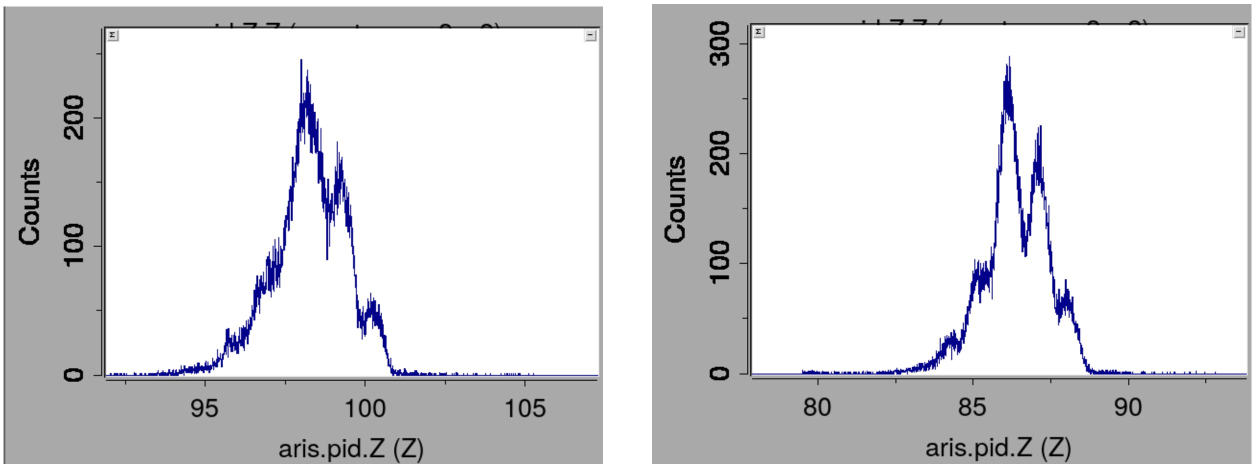

(a) Z method 0: $\sigma(Z) = 0.3552$

(b) Z method 1: $\sigma(Z) = 0.2697$

Figure 16: Increased resolution achieved when Z method 1 is used.

2.2.6 Final PID Resolution

As discussed previously, the intrinsic resolution of particle identification is commonly quantified by the widths (σ) of the Gaussian-like distributions observed in PID space. These widths reflect the combined experimental uncertainties in the measured observables used for identification, such as time-of-flight, energy-loss, and total kinetic energy. In addition to the absolute widths of individual PID peaks, the effective resolving power also depends on the separation between neighboring species. This separation is governed by the underlying nuclear properties (A, Z, and charge-state q) as well as the detector and beam-line resolutions that determine how distinctly different species map into PID space. A high-confidence PID is therefore characterized by both small peak widths and sufficient separation between adjacent isotope blobs.

This interplay between peak width and peak separation is illustrated in Figure 7, where gaps between PID clusters significantly improve the reliability of isotope assignment and yield extraction. When such gaps are present, systematic uncertainties associated with peak overlap and background subtraction are substantially reduced, leading to more robust cross section determinations.

A quantitative estimate of the overall PID resolution can be obtained using the `lise64` Excel spreadsheet PID resolution calculator [6]. This tool takes as input the experimentally measured resolutions of the individual observables (ToF, ΔE, and TKE), the assumed identification parameters (A, Z, and q), the magnetic rigidity setting, relevant optical properties of the beam line (including dispersion, magnification, and final image size), and the intrinsic detector resolutions. These contributions are then combined to produce a single, effective PID resolution that reflects the convolution of all experimental and optical effects. This calculated number provides a useful benchmark for assessing PID performance and for guiding the optimization of analysis cuts and spectrometer settings.

3 Data Extraction and Isotopic Yields

Once calibration and data cleaning are complete, isotopic yields may be extracted. This procedure assumes that elemental and isotopic peaks are well separated and that the remaining resolution is dominated by detector response rather than unresolved physical structure. In regions where peaks overlap significantly or statistics are extremely limited, extracted yields must be interpreted with additional caution.

Extraction is performed using a dedicated Excel workbook designed for yield determination. Elemental and isotopic peaks are modeled as Gaussian distributions, with all peaks in a given spectrum constrained to share a common width. This reflects the approximately uniform experimental resolution across the relevant charge or mass range after calibration.

3.1 Exporting Data from `SpecTcl`

Create the one-dimensional atomic number spectrum, Z, with all previously defined cleaning gates applied. Verify that the full data range is displayed and that the number of bins is sufficient to resolve individual elemental peaks without introducing artificial binning artifacts.

Once verified, export the spectrum using the following command:

```
swrite -format ascii <fileName><spectrumName>.
```

This command writes the specified spectrum as an ASCII file to the `SpecTcl` root directory.

3.2 Obtaining Yield Statistics

The purpose-built Z-extraction workbook (Fig. 17) models the elemental distribution as a sum of Gaussian peaks. The `lise64` workbook must be open concurrently, as it provides Gaussian function and reference utilities generated by `LISE`$^{++}$.

Enter the axis limits, bin count, and charge-state in the designated input fields (blue boxes in Fig. 17). These values must match the `SpecTcl` spectrum definition. Copy the histogram channel numbers and corresponding yields into columns A and B, respectively.

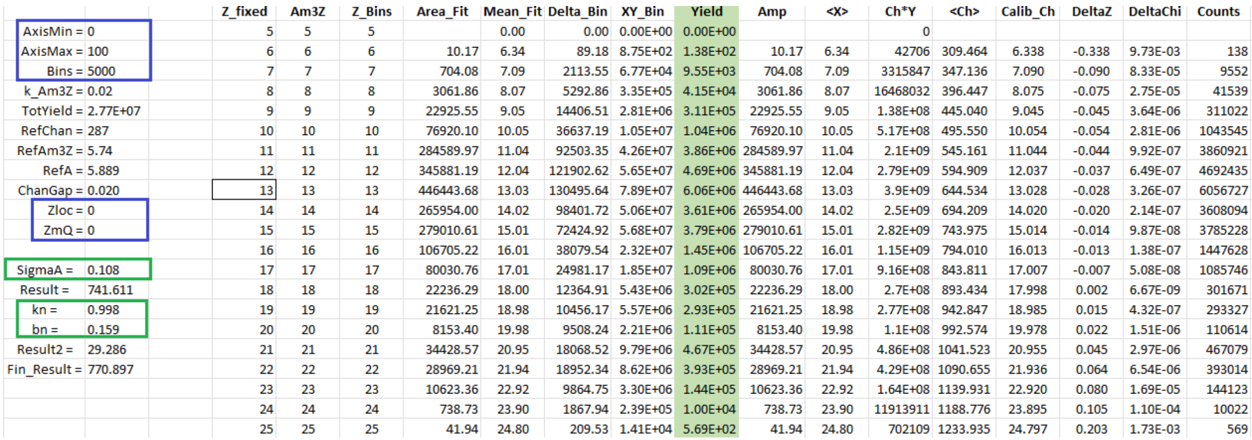

		Z_fixed	Am3Z	Z_Bins	Area_Fit	Mean_Fit	Delta_Bin	XY_Bin	Yield	Amp	<X>	Ch*Y	<Ch>	Calib_Ch	DeltaZ	DeltaChi	Counts
AxisMin =	0	5	5	5		0.00	0.00	0.00E+00	0.00E+00			0					
AxisMax =	100	6	6	6	10.17	6.34	89.18	8.75E+02	1.38E+02	10.17	6.34	42706	309.464	6.338	-0.338	9.73E-03	138
Bins =	5000	7	7	7	704.08	7.09	2113.55	6.77E+04	9.55E+03	704.08	7.09	3315847	347.136	7.090	-0.090	8.33E-05	9552
k_Am3Z =	0.02	8	8	8	3061.86	8.07	5292.86	3.35E+05	4.15E+04	3061.86	8.07	16468032	396.447	8.075	-0.075	2.75E-05	41539
TotYield =	2.77E+07	9	9	9	22925.55	9.05	14406.51	2.81E+06	3.11E+05	22925.55	9.05	1.38E+08	445.040	9.045	-0.045	3.64E-06	311022
RefChan =	287	10	10	10	76920.10	10.05	36637.19	1.05E+07	1.04E+06	76920.10	10.05	5.17E+08	495.550	10.054	-0.054	2.81E-06	1043545
RefAm3Z =	5.74	11	11	11	284589.97	11.04	92503.35	4.26E+07	3.86E+06	284589.97	11.04	2.1E+09	545.161	11.044	-0.044	9.92E-07	3860921
RefA =	5.889	12	12	12	345881.19	12.04	121902.62	5.65E+07	4.69E+06	345881.19	12.04	2.79E+09	594.909	12.037	-0.037	6.49E-07	4692435
ChanGap =	0.020	13	13	13	446443.68	13.03	130495.64	7.89E+07	6.06E+06	446443.68	13.03	3.9E+09	644.534	13.028	-0.028	3.26E-07	6056727
Zloc =	0	14	14	14	265954.00	14.02	98401.72	5.06E+07	3.61E+06	265954.00	14.02	2.5E+09	694.209	14.020	-0.020	2.14E-07	3608094
ZmQ =	0	15	15	15	279010.61	15.01	72424.92	5.68E+07	3.79E+06	279010.61	15.01	2.82E+09	743.975	15.014	-0.014	9.87E-08	3785228
		16	16	16	106705.22	16.01	38079.54	2.32E+07	1.45E+06	106705.22	16.01	1.15E+09	794.010	16.013	-0.013	1.38E-07	1447628
SigmaA =	0.108	17	17	17	80030.76	17.01	24981.17	1.85E+07	1.09E+06	80030.76	17.01	9.16E+08	843.811	17.007	-0.007	5.08E-08	1085746
Result =	741.611	18	18	18	22236.29	18.00	12364.91	5.43E+06	3.02E+05	22236.29	18.00	2.7E+08	893.434	17.998	0.002	6.67E-09	301671
kn =	0.998	19	19	19	21621.25	18.98	10456.17	5.57E+06	2.93E+05	21621.25	18.98	2.77E+08	942.847	18.985	0.015	4.32E-07	293327
bn =	0.159	20	20	20	8153.40	19.98	9508.24	2.21E+06	1.11E+05	8153.40	19.98	1.1E+08	992.574	19.978	0.022	1.51E-06	110614
Result2 =	29.286	21	21	21	34428.57	20.95	18068.52	9.79E+06	4.67E+05	34428.57	20.95	4.86E+08	1041.523	20.955	0.045	2.97E-06	467079
Fin_Result =	770.897	22	22	22	28969.21	21.94	18952.34	8.62E+06	3.93E+05	28969.21	21.94	4.29E+08	1090.655	21.936	0.064	6.54E-06	393014
		23	23	23	10623.36	22.92	9864.75	3.30E+06	1.44E+05	10623.36	22.92	1.64E+08	1139.931	22.920	0.080	1.69E-05	144123
		24	24	24	738.73	23.90	1867.94	2.39E+05	1.00E+04	738.73	23.90	11913911	1188.776	23.895	0.105	1.10E-04	10022
		25	25	25	41.94	24.80	209.53	1.41E+04	5.69E+02	41.94	24.80	702109	1233.935	24.797	0.203	1.73E-03	569

Figure 17: Z-fitting Excel spreadsheet. Using functions from the `lise64` workbook, Gaussian functions are fit to the data. Set-up information in the colored boxes are taken from `SpecTcl`.

All Gaussian peaks are constrained to share a common standard deviation (σ), reflecting the assumption of uniform charge resolution across the spectrum. The free fit parameters are:

- the common width σ,
- a linear slope controlling peak spacing,
- and an offset controlling the absolute centroid position.

For properly calibrated data, the slope should remain close to unity and the offset close to zero. Significant deviations typically indicate residual calibration inconsistencies. To stabilize the fit, it is recommended to constrain the centroid of the dominant elemental peak to its value determined in `SpecTcl`. This prevents unphysical drift of the reference peak during minimization.

Excel Solver is used to minimize the difference between the experimental spectrum and the Gaussian sum. Two error functions are available, with adjustable weights to improve convergence in low-statistics or partially overlapping regions. As with the total kinetic energy calibration workbook, using Excel's precedent and dependent tracing tools can be helpful for understanding how changes propagate through the calculation.

A successful fit reproduces the experimental distribution both visually and numerically (Fig. 18). The calculated Gaussian sum should track the measured spectrum across both peak regions and tails.

In some cases, the Gaussian fitting procedure may fail to converge or may produce unphysical results. The most common indicators of a problematic fit include:

- unusually large or small values of σ,
- significant deviations of the slope from unity,
- offsets far from zero, or
- visible discrepancies between the calculated and experimental distributions.

If the fitted slope or offset deviates substantially from expected values, this often indicates residual calibration issues in the upstream analysis. In such cases, the relevant calibration spectra should be revisited before proceeding.

Poor convergence or unstable fits can also result from low statistics or overlapping peaks, particularly near the edges of the acceptance. Adjusting the relative weights of the error functions in the Solver may improve stability. In some situations, temporarily fixing the slope and offset to their nominal values and fitting only for σ can help diagnose whether the instability arises from resolution effects or from misaligned peak centroids.

Finally, visual inspection remains an essential diagnostic tool. Even when the numerical minimization converges, the fitted distribution should always be compared directly to the experimental spectrum to ensure that the Gaussian model provides an adequate description of the data.

Once the optimal σ is determined, define elemental gates in `SpecTcl` corresponding to $\pm 3\sigma$ around each fitted centroid. These gates define the experimental elemental acceptance used for all subsequent isotopic yield extractions.

A practical approach is to place approximate gates visually in `SpecTk`, then refine the gate limits numerically in the `SpecTcl Gates` tab using the fitted $\pm 3\sigma$ values.

3.3 Deduced PID Integer Values

Isotopic distributions are generated by applying an `And` gate combining the cleaning gates with the appropriate Z gate. The gated events are projected onto a one-dimensional $A - 3Z$ axis for neutron-rich fragments, or $A - 2Z$ for proton-rich fragments.

In `SpecTcl`, the quantity labeled $A - 3Z$ is constructed from the measured A/q and Z assuming charge-state q:

$$A - 3Z = ((A/q) - 3)\, Z. \tag{1}$$

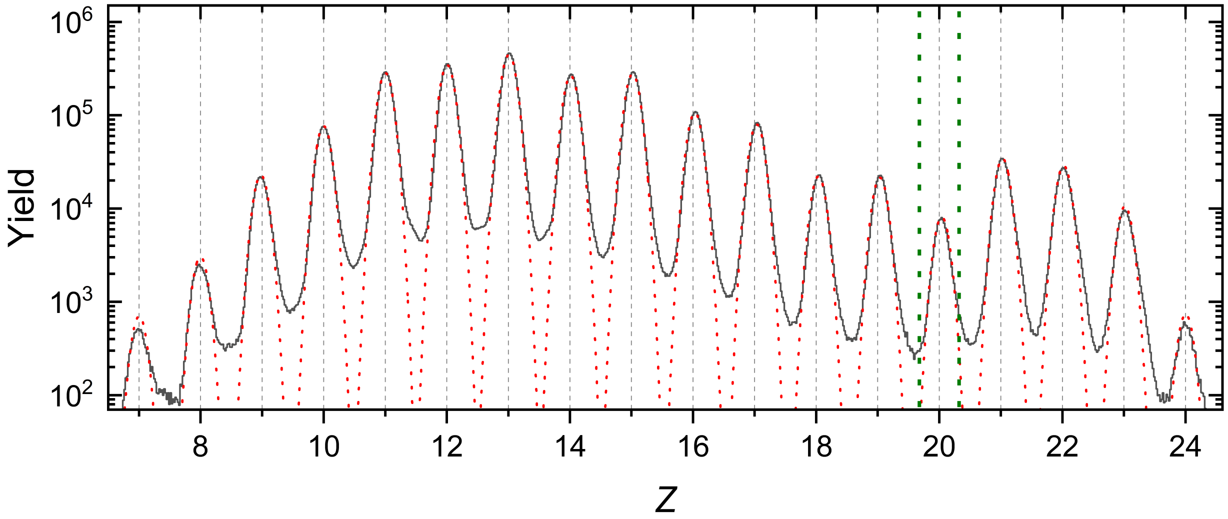

Figure 18: Z distribution (solid gray line) with calculated Gaussian (dotted red line) overlaid. Dashed green line represents a $\pm 3\sigma$ gate.

This expression is exact for fully stripped ions ($q = Z$). For partially stripped ions, the resulting value no longer corresponds strictly to $A-3Z$, but remains a useful PID coordinate, as different charge-states map to distinct loci in the projection.

This projection is motivated by both physical and practical considerations. For neutron-rich fragments, A and Z are strongly correlated along approximately constant $A - 3Z$ trajectories. The observed alignment reflects the charge-dispersion formalism of EPAX [8, 9], in which the most probable charge for a given mass follows an approximately linear relationship in the $A - Z$ plane due to projectile N/Z memory. Projecting onto this variable aligns isotopes of a given element along a single axis, reducing overlap and improving separation in low-statistics regions.

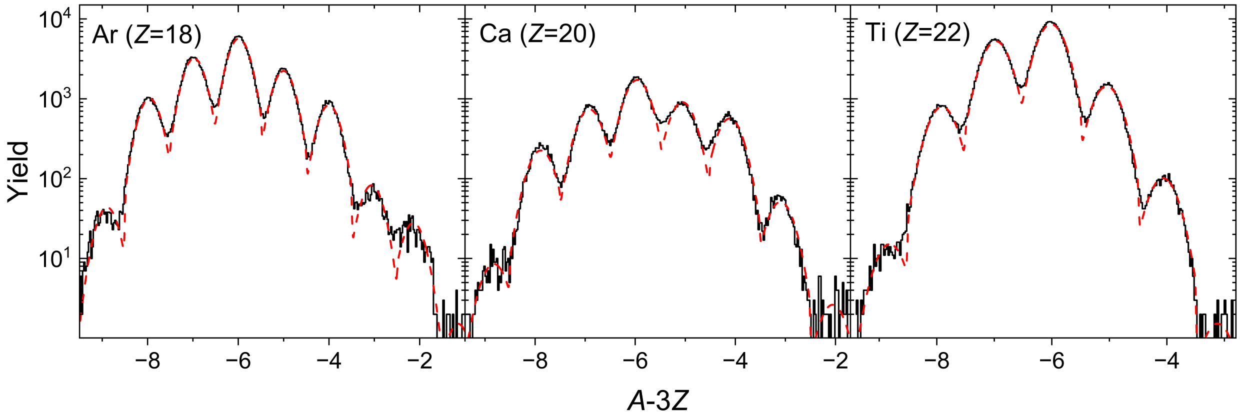

Figure 19: $A - 3Z$ distribution (solid gray line) with calculated Gaussian (dotted red line) overlaid for three elements.

Similarly, proton-rich fragments are more cleanly separated using $A - 2Z$, which better follows the dominant correlation direction in that region of the fragment distribution.

By projecting onto a coordinate approximately orthogonal to the dominant correlation direction, residual correlations between mass, charge, and time-of-flight are reduced. The resulting one-dimensional peaks are narrower and more symmetric, improving Gaussian fit stability and yield reliability.

	absolute		relative		
Y	$-dY$	$+dY$	$-dY$	$+dY$	$\sqrt{Y}$
1	0.63	1.75	−63%	175%	1.00
2	1.26	2.25	−63%	113%	1.41
3	1.90	2.30	−63%	77%	1.73
4	1.66	2.78	−42%	70%	2.00
5	2.25	2.81	−45%	56%	2.24
6	2.18	3.28	−36%	55%	2.45
7	2.75	3.30	−39%	47%	2.65
8	2.70	3.32	−34%	42%	2.83
9	2.67	3.79	−30%	42%	3.00
10	3.22	3.81	−32%	38%	3.16
11	3.19	3.82	−29%	35%	3.32
12	3.17	4.29	−26%	36%	3.46
13	3.72	4.30	−29%	33%	3.61
14	3.70	4.32	−26%	31%	3.74
15	3.68	4.32	−25%	29%	3.87
16	3.67	4.80	−23%	30%	4.00
17	4.21	4.81	−25%	28%	4.12
18	4.19	4.82	−23%	27%	4.24
19	4.18	4.82	−22%	25%	4.36
20	4.17	5.30	−21%	27%	4.47
21	4.58	4.58	−22%	22%	4.58

Table 1: Absolute and relative errors for small statistics as a function of Y. Adapted from [10]

In addition to improving peak separation, projections onto $A-3Z$ (neutron-rich) and $A-2Z$ (proton-rich) partially cancel correlated uncertainties in the reconstructed values of A and Z, further reducing the effective variance of the projected variable, as both quantities are derived from overlapping experimental observables [11].

As with the elemental spectra, the isotopic distributions are exported from `SpecTcl` and analyzed using the same Excel fitting framework as the elemental yields to extract Gaussian parameters. An example of an $A-3Z$ spectrum with fitted Gaussian peaks is shown in Figure 19. This representation illustrates the improved separation and symmetry of isotopic peaks obtained using the $A-3Z$ projection.

The yield for each isotope is defined as the area under its fitted Gaussian peak. Conversion to atomic mass A is performed using the selected charge-state. In most cases, fully stripped fragments satisfy $Z=q$, allowing direct conversion from the fitted $A-3Z$ value.

When multiple charge-states are present, only the gated charge-state must be used in the conversion.

Depending on the length of a given isotopic chain, the result block in the spreadsheet may need to be extended. Care should be taken to expand all relevant ranges uniformly to avoid truncation or misalignment of calculated values.

3.4 Counting Statistics

After yields are extracted, statistical uncertainties must be assigned. For $Y > 20$ counts, the Gaussian approximation $\sqrt{Y}$ provides a reasonable estimate of the statistical uncertainty. For $Y \leq 20$, asymmetric confidence intervals derived from Poisson statistics should be used instead, as summarized in Table 1.

The asymmetry in these intervals arises from the discrete and non-negative nature of Poisson counting statistics, particularly at low event counts. These statistical uncertainties represent only the counting contribution and must be combined with systematic uncertainties arising from background subtraction, charge-state contamination, transmission corrections, and calibration effects. Details of these sources of background are discussed further in paragraph 2.2.3.1.

These yield uncertainties form the statistical component of the cross section uncertainty, which is propagated together with transmission, target thickness, and beam integral uncertainties as described in section 6.

4 Experimental Inputs for Cross Section Determination

Production cross sections require two primary experimental inputs:

1. the effective target thickness, and
2. the total number of incident beam particles.

The determination of these quantities is described in the following subsections.

4.1 Target Thickness

The effective areal density of the target (and any wedges) is determined using energy-loss measurements with the primary beam. The beam energy is known from accelerator settings, and its passage through material produces a predictable energy-loss that depends on the material's areal density. A detailed discussion of the method is provided in subsection E.3.

Operationally, the primary beam is first transported to the first dispersive focal plane of the separator without material inserted. The beam is centered at the viewer position. When the target is inserted, the beam loses energy, reducing its magnetic rigidity and causing a shift along the dispersive axis (vertical y direction in the pre-separator).

To restore the beam to the original focal plane position, the magnetic rigidity $B\rho$ is adjusted. The required change in $B\rho$ is directly related to the energy-loss in the material and therefore to the effective areal density of the target. The same procedure is applied to determine the thicknesses of wedges or degraders used in the separator.

The resulting target and wedge thicknesses are recorded in the corresponding `LISE`$^{++}$ file and are typically documented in the Olog. These values must be used consistently in all subsequent transmission and cross section calculations.

4.2 Beam Integral

The beam integral quantifies the total number of primary beam particles incident on the target during data collection. This quantity is obtained by integrating the measured beam power over time and converting the total delivered energy into particle number using the known beam energy[14].

An Excel workbook has been developed to streamline this calculation. The workflow is:

1. Identify beam power measurements whose timestamps fall between the recorded start and stop times of each data run (Fig. 20).
2. Collate these measurements into columns of elapsed time and corresponding beam power.
3. Perform a trapezoidal integration of the power curve over time.

Negative power readings, which arise from measurement artifacts or baseline fluctuations, must be set to zero before integration.

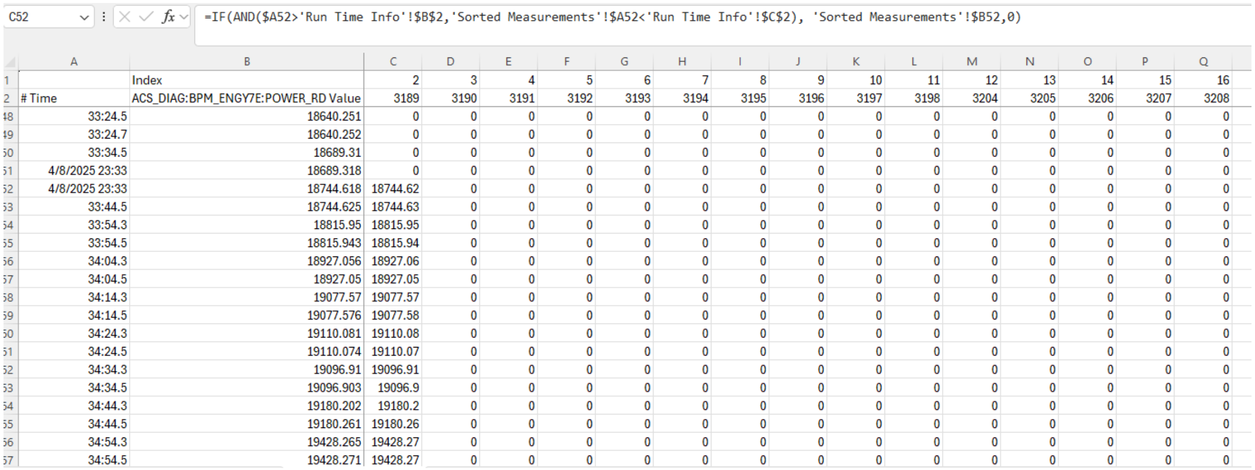

```
=IF(AND($A52>'Run Time Info'!$B$2,'Sorted Measurements'!$A52<'Run Time Info'!$C$2), 'Sorted Measurements'!$B52,0)
```

A	B	C	D	E	F	G	H	I	J	K	L	M	N	O	P	Q
	Index	2	3	4	5	6	7	8	9	10	11	12	13	14	15	16
# Time	ACS_DIAG:BPM_ENGY7E:POWER_RD Value	3189	3190	3191	3192	3193	3194	3195	3196	3197	3198	3204	3205	3206	3207	3208
33:24.5	18640.251	0	0	0	0	0	0	0	0	0	0	0	0	0	0	0
33:24.7	18640.252	0	0	0	0	0	0	0	0	0	0	0	0	0	0	0
33:34.5	18689.31	0	0	0	0	0	0	0	0	0	0	0	0	0	0	0
4/8/2025 23:33	18689.318	0	0	0	0	0	0	0	0	0	0	0	0	0	0	0
4/8/2025 23:33	18744.618	18744.62	0	0	0	0	0	0	0	0	0	0	0	0	0	0
33:44.5	18744.625	18744.63	0	0	0	0	0	0	0	0	0	0	0	0	0	0
33:54.3	18815.95	18815.95	0	0	0	0	0	0	0	0	0	0	0	0	0	0
33:54.5	18815.943	18815.94	0	0	0	0	0	0	0	0	0	0	0	0	0	0
34:04.3	18927.056	18927.06	0	0	0	0	0	0	0	0	0	0	0	0	0	0
34:04.5	18927.05	18927.05	0	0	0	0	0	0	0	0	0	0	0	0	0	0
34:14.3	19077.57	19077.57	0	0	0	0	0	0	0	0	0	0	0	0	0	0
34:14.5	19077.576	19077.58	0	0	0	0	0	0	0	0	0	0	0	0	0	0
34:24.3	19110.081	19110.08	0	0	0	0	0	0	0	0	0	0	0	0	0	0
34:24.5	19110.074	19110.07	0	0	0	0	0	0	0	0	0	0	0	0	0	0
34:34.3	19096.91	19096.91	0	0	0	0	0	0	0	0	0	0	0	0	0	0
34:34.5	19096.903	19096.9	0	0	0	0	0	0	0	0	0	0	0	0	0	0
34:44.3	19180.202	19180.2	0	0	0	0	0	0	0	0	0	0	0	0	0	0
34:44.5	19180.261	19180.26	0	0	0	0	0	0	0	0	0	0	0	0	0	0
34:54.3	19428.265	19428.27	0	0	0	0	0	0	0	0	0	0	0	0	0	0
34:54.5	19428.271	19428.27	0	0	0	0	0	0	0	0	0	0	0	0	0	0

Figure 20: Excel workbook that collates the beam power measurements falling between the start and stop timestamps of data collection runs.

After constructing the beam power time series, verify the consistency of the elapsed run duration. Convert the run start and stop timestamps to elapsed seconds and compare this duration with the cumulative time span represented by the beam power measurements.

---

[14] Instructions for extracting the raw data has been compiled in a help sheet. See /projects/lisedev /Literature/Cross Section Manual

These quantities should agree within expected sampling or rounding limits. Significant discrepancies may indicate missing measurements, DAQ interruptions, or misalignment between run timestamps and power-monitor data. Because the beam integral enters directly into the cross section denominator, any such inconsistency propagates linearly into the final result.

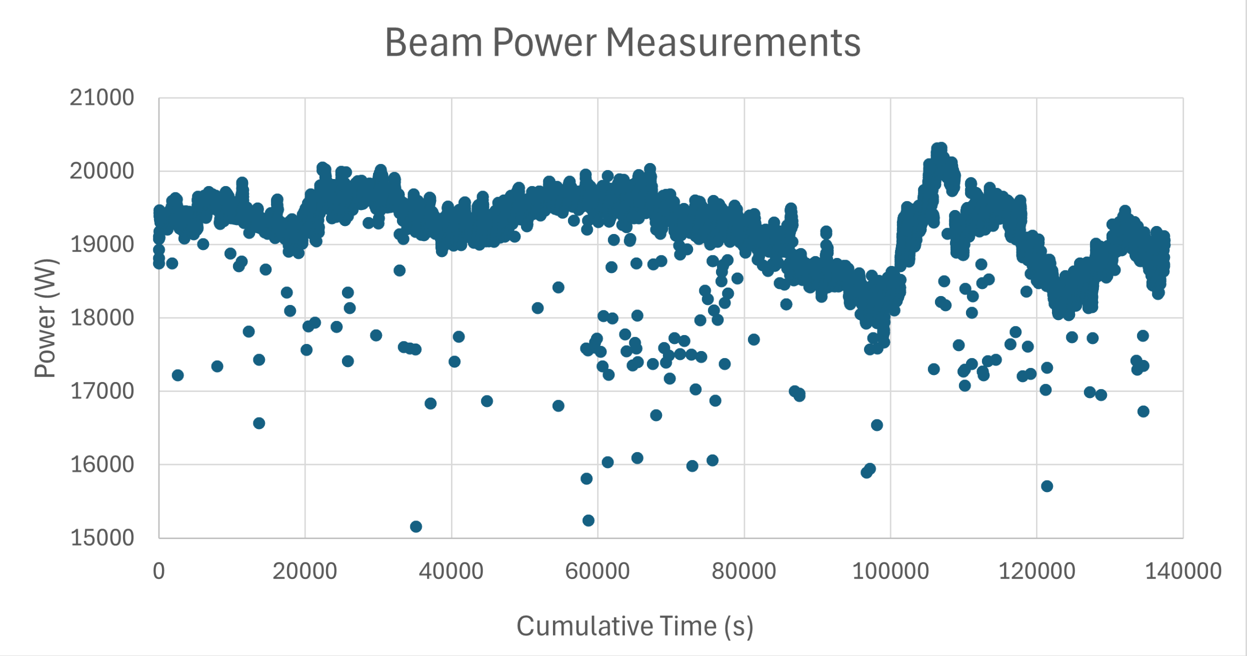

Figure 21: Resulting beam power graph from the beam integral workbook (Fig. 20). A trapezoidal integration of this curve yields the total energy delivered to the target.

The integrated beam power yields the total energy delivered to the target:

$$E_{\text{tot}} = \int P(t)\,dt.$$

Dividing this energy by the kinetic energy per projectile gives the total number of incident beam particles:

$$N_{\text{beam}} = \frac{E_{\text{tot}}}{E_{\text{beam}}}.$$

Care must be taken to ensure unit consistency when performing this conversion (e.g., joules vs MeV).

To estimate the uncertainty in the beam integral, a conservative approach is to assign an uncertainty to each power measurement equal to the magnitude of the largest observed negative reading (assumed to represent the scale of baseline fluctuations). Propagating this uncertainty through the trapezoidal integration provides an upper bound on the uncertainty in N_{beam}.

In most experiments, this contribution is small compared to statistical yield uncertainties and transmission corrections. Nevertheless, explicitly performing this estimate reinforces proper error propagation practices and ensures transparency in the cross section determination.

Together with the transmission correction described in section 5, these quantities provide the full normalization required for production cross section extraction.

5 `LISE`$^{++}$ Transmission Analysis

A central step in cross section analysis is determining the transmission from the target to the final focal plane. The number of fragments produced at the target is generally much larger than the number detected. Correcting for transport losses is therefore essential for an accurate cross section.

`LISE`$^{++}$ is a simulation tool for predicting fragment production, transport, and yields [12–15]. The objective of the transmission analysis is to reproduce the experimentally observed fragment rates using physically reasonable separator settings. For isotopes with previously measured cross sections, ensure the corresponding experimental data are loaded into `LISE`$^{++}$. For isotopes without measurements, theoretical predictions must be used.

5.1 Procedure

Begin by setting the primary beam rate in the segmented experiment file equal to the calculated beam integral. Then compute the fragment rates and transmissions at the final focal plane and compare them to the experimental yields. Initial disagreement is expected; iterative adjustment is required.

The parameters most commonly adjusted are:

- Target thickness and defect
- Wedge thickness, defect, and lateral offset

Only after all material-related adjustments have been explored should optics parameters (e.g., DB1 settings) be modified. Momentum-distribution parameters within `LISE`$^{++}$ may also be adjusted, but only with clear physical justification.

Physical plausibility check: After each modification, ask whether the change is physically reasonable. Adjustments should remain within experimental uncertainty. As a rule of thumb:

- Target or wedge thickness changes exceeding $\sim 5\%$ are likely unphysical.
- Slit or offset changes exceeding ~ 1 mm should be carefully justified.

After each iteration, record the transmission and predicted rates for all relevant fragments. Tracking these trends helps identify which parameters dominate the transmission sensitivity.

Warning: Pre-separator momentum slits. When set asymmetrically, the reference coordinate system becomes important. In the saveset, slit values follow physics coordinates;

in `LISE`$^{++}$, they are defined in beam coordinates. This results in a reversal of the values (e.g., $-75\ +60 \rightarrow -60\ +75$). Failure to account for this can introduce significant errors.

Document the baseline target defect used in the final transmission solution. This value will later serve as the thickness uncertainty in the cross section error propagation.

5.2 Distinguishing Primary and Secondary Fragments

Not all fragments reaching the final focal plane are primary products from the target. Contaminants may arise from:

- Secondary reactions in the target
- Reactions in wedge materials
- Higher-order optical effects

`LISE`$^{++}$ provides tools to evaluate these contributions:

- `Physical Models` → `Secondary Reactions in the Target`
- `Calculate reactions in this material` (material dialog)

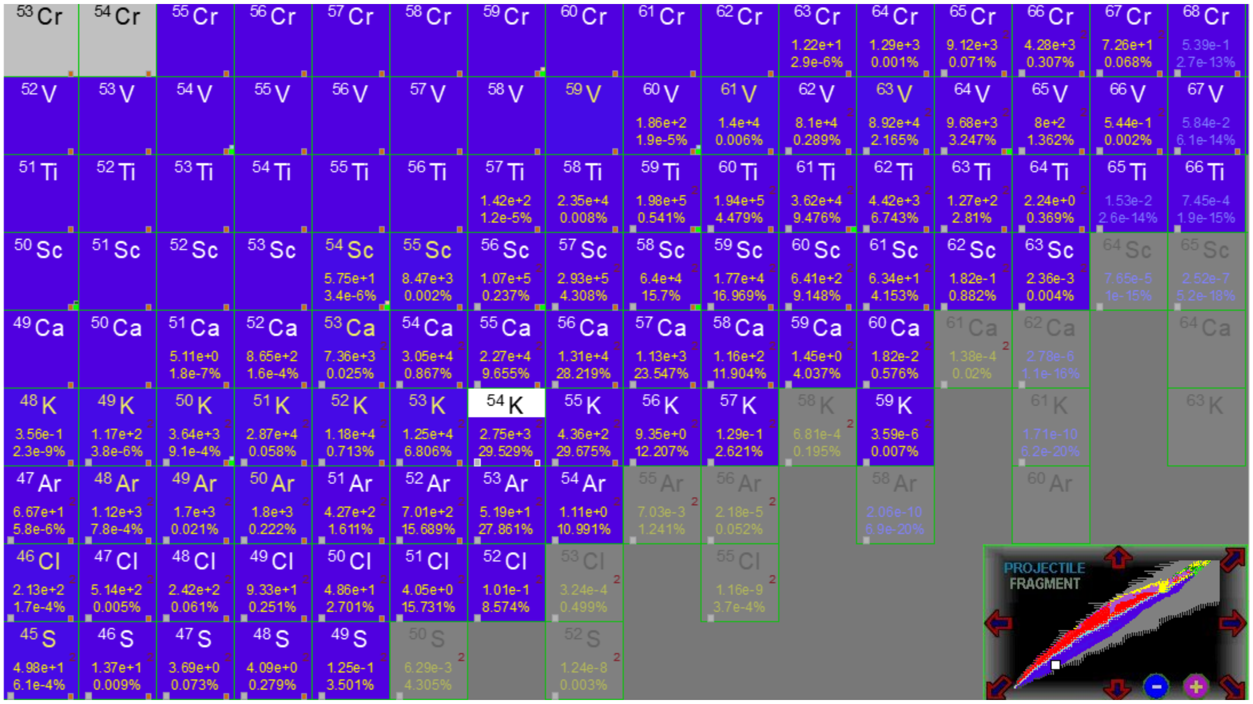

^{53}Cr	^{54}Cr	^{55}Cr	^{56}Cr	^{57}Cr	^{58}Cr	^{59}Cr	^{60}Cr	^{61}Cr	^{62}Cr	^{63}Cr 1.22e+1 2.9e-6%	^{64}Cr 1.29e+3 0.001%	^{65}Cr 9.12e+3 0.071%	^{66}Cr 4.28e+3 0.307%	^{67}Cr 7.26e+1 0.068%	^{68}Cr 5.39e-1 2.7e-13%
^{52}V	^{53}V	^{54}V	^{55}V	^{56}V	^{57}V	^{58}V	^{59}V	^{60}V 1.86e+2 1.9e-5%	^{61}V 1.4e+4 0.006%	^{62}V 8.1e+4 0.289%	^{63}V 8.92e+4 2.165%	^{64}V 9.68e+3 3.247%	^{65}V 8e+2 1.362%	^{66}V 5.44e-1 0.002%	^{67}V 5.84e-2 6.1e-14%
^{51}Ti	^{52}Ti	^{53}Ti	^{54}Ti	^{55}Ti	^{56}Ti	^{57}Ti 1.42e+2 1.2e-5%	^{58}Ti 2.35e+4 0.008%	^{59}Ti 1.98e+5 0.541%	^{60}Ti 1.94e+5 4.479%	^{61}Ti 3.62e+4 9.476%	^{62}Ti 4.42e+3 6.743%	^{63}Ti 1.27e+2 2.81%	^{64}Ti 2.24e+0 0.369%	^{65}Ti 1.53e-2 2.6e-14%	^{66}Ti 7.45e-4 1.9e-15%
^{50}Sc	^{51}Sc	^{52}Sc	^{53}Sc	^{54}Sc 5.75e+1 3.4e-6%	^{55}Sc 8.47e+3 0.002%	^{56}Sc 1.07e+5 0.237%	^{57}Sc 2.93e+5 4.308%	^{58}Sc 6.4e+4 15.7%	^{59}Sc 1.77e+4 16.969%	^{60}Sc 6.41e+2 9.148%	^{61}Sc 6.34e+1 4.153%	^{62}Sc 1.82e-1 0.882%	^{63}Sc 2.36e-3 0.004%	^{64}Sc 7.65e-5 1e-15%	^{65}Sc 2.52e-7 5.2e-18%
^{49}Ca	^{50}Ca	^{51}Ca 5.11e+0 1.8e-7%	^{52}Ca 8.65e+2 1.6e-4%	^{53}Ca 7.36e+3 0.025%	^{54}Ca 3.05e+4 0.867%	^{55}Ca 2.27e+4 9.655%	^{56}Ca 1.31e+4 28.219%	^{57}Ca 1.13e+3 23.547%	^{58}Ca 1.16e+2 11.904%	^{59}Ca 1.45e+0 4.037%	^{60}Ca 1.82e-2 0.576%	^{61}Ca 1.38e-4 0.02%	^{62}Ca 2.78e-6 1.1e-16%		^{64}Ca
^{48}K 3.56e-1 2.3e-9%	^{49}K 1.17e+2 3.8e-6%	^{50}K 3.64e+3 9.1e-4%	^{51}K 2.87e+4 0.058%	^{52}K 1.18e+4 0.713%	^{53}K 1.25e+4 6.806%	^{54}K 2.75e+3 29.529%	^{55}K 4.36e+2 29.675%	^{56}K 9.35e+0 12.207%	^{57}K 1.29e-1 2.621%	^{58}K 6.81e-4 0.195%	^{59}K 3.59e-6 0.007%		^{61}K 1.71e-10 6.2e-20%		^{63}K
^{47}Ar 6.67e+1 5.8e-6%	^{48}Ar 1.12e+3 7.8e-4%	^{49}Ar 1.7e+3 0.021%	^{50}Ar 1.8e+3 0.222%	^{51}Ar 4.27e+2 1.611%	^{52}Ar 7.01e+2 15.689%	^{53}Ar 5.19e+1 27.861%	^{54}Ar 1.11e+0 10.991%	^{55}Ar 7.03e-3 1.241%	^{56}Ar 2.18e-5 0.052%		^{58}Ar 2.06e-10 6.9e-20%		^{60}Ar		
^{46}Cl 2.13e+2 1.7e-4%	^{47}Cl 5.14e+2 0.005%	^{48}Cl 2.42e+2 0.061%	^{49}Cl 9.33e+1 0.251%	^{50}Cl 4.86e+1 2.701%	^{51}Cl 4.05e+0 15.731%	^{52}Cl 1.01e-1 8.574%	^{53}Cl 3.24e-4 0.499%		^{55}Cl 1.16e-9 3.7e-4%						
^{45}S 4.98e+1 6.1e-4%	^{46}S 1.37e+1 0.009%	^{47}S 3.69e+0 0.073%	^{48}S 4.09e+0 0.279%	^{49}S 1.25e-1 3.501%	^{50}S 6.29e-3 4.305%		^{52}S 1.24e-8 0.003%								

Figure 22: `LISE`$^{++}$ calculations of rate and transmission with secondary and wedge reactions enabled.

Compare simulations with these options enabled and disabled. Fragments dominated by secondary or material-reaction contributions are displayed in light gray in the isotope chart (Figure 22, e.g., ^{68}Cr). Such isotopes should generally be excluded from cross section extraction.

Higher-order optical effects are evaluated using Monte Carlo simulations:

1. In the main window, calculate transmissions for the isotopes of interest.
2. Open the `Monte Carlo` dialog.
3. Select `Group of isotopes already calculated`.
4. Set `After BLOCK` to DB5 slits.
5. Set X-coordinate to $A - 3q$ and Y-coordinate to Z.
6. Choose the optics order.

Run the Monte Carlo calculation to first order. After sufficient statistics are accumulated, stop the simulation and select `MC transmission statistics` to obtain the predicted transmission at DB5. Save the results and repeat using fifth-order optics.

Significant changes between first- and fifth-order transmission indicate sensitivity to higher-order aberrations. Isotopes exhibiting large transmission changes should be flagged as candidates for exclusion.

5.3 Estimating Transmission Uncertainty

Once primary fragments are identified and simulated yields reproduce experimental data (Figure 23), transmission uncertainties can be estimated. These uncertainties arise from deviations between simulated parameters and their experimentally determined values.

For each adjusted parameter (e.g., target thickness, wedge offset, slit position):

1. Vary the parameter slightly above and below the nominal value.
2. Recalculate the fragment transmission.
3. Record the deviation from the nominal transmission.

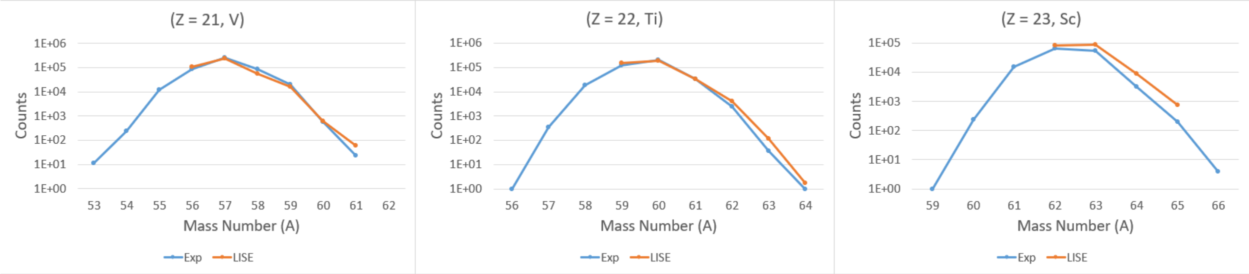

Figure 23: Comparison of experimental yields to final `LISE`$^{++}$-predicted yields for primary fragments.

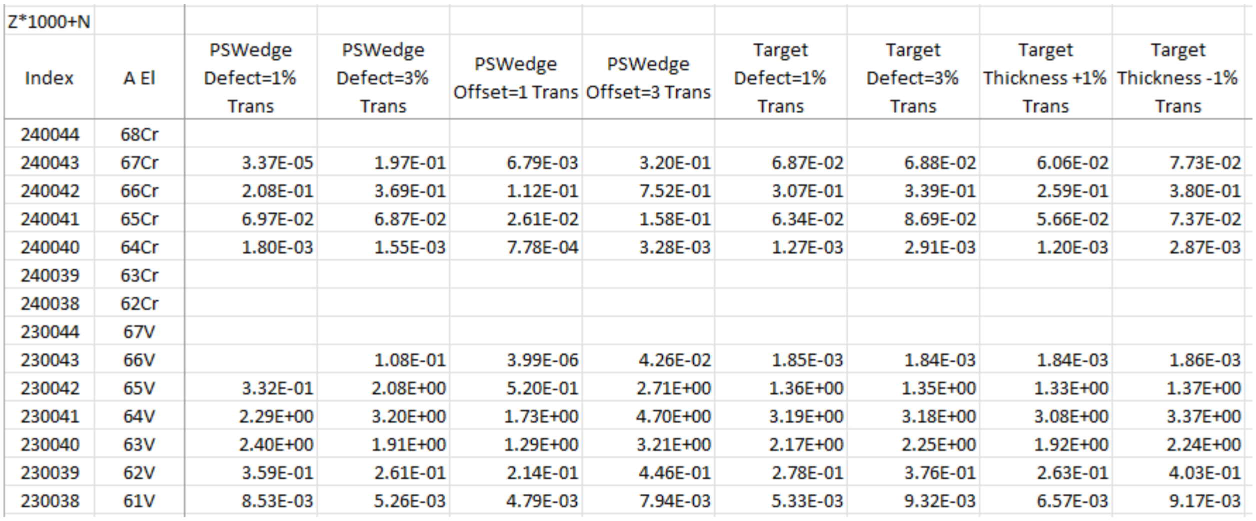

Z*1000+N Index	A El	PSWedge Defect=1% Trans	PSWedge Defect=3% Trans	PSWedge Offset=1 Trans	PSWedge Offset=3 Trans	Target Defect=1% Trans	Target Defect=3% Trans	Target Thickness +1% Trans	Target Thickness -1% Trans
240044	68Cr								
240043	67Cr	3.37E-05	1.97E-01	6.79E-03	3.20E-01	6.87E-02	6.88E-02	6.06E-02	7.73E-02
240042	66Cr	2.08E-01	3.69E-01	1.12E-01	7.52E-01	3.07E-01	3.39E-01	2.59E-01	3.80E-01
240041	65Cr	6.97E-02	6.87E-02	2.61E-02	1.58E-01	6.34E-02	8.69E-02	5.66E-02	7.37E-02
240040	64Cr	1.80E-03	1.55E-03	7.78E-04	3.28E-03	1.27E-03	2.91E-03	1.20E-03	2.87E-03
240039	63Cr								
240038	62Cr								
230044	67V								
230043	66V		1.08E-01	3.99E-06	4.26E-02	1.85E-03	1.84E-03	1.84E-03	1.86E-03
230042	65V	3.32E-01	2.08E+00	5.20E-01	2.71E+00	1.36E+00	1.35E+00	1.33E+00	1.37E+00
230041	64V	2.29E+00	3.20E+00	1.73E+00	4.70E+00	3.19E+00	3.18E+00	3.08E+00	3.37E+00
230040	63V	2.40E+00	1.91E+00	1.29E+00	3.21E+00	2.17E+00	2.25E+00	1.92E+00	2.24E+00
230039	62V	3.59E-01	2.61E-01	2.14E-01	4.46E-01	2.78E-01	3.76E-01	2.63E-01	4.03E-01
230038	61V	8.53E-03	5.26E-03	4.79E-03	7.94E-03	5.33E-03	9.32E-03	6.57E-03	9.17E-03

Figure 24: Calculation of transmission for various changes in the final `LISE`$^{++}$ transmission file. These changes correspond to the uncertainty of set parameters. The largest transmission change in a given fragment will constitute the uncertainty for that fragment.

These deviations define the uncertainty contribution of that parameter (Figure 24). For example, ^{67}Cr shows strong suppression when the pre-separator wedge defect is reduced below the nominal 2%, and enhancement when the wedge offset increases from 2 mm to 3 mm.

After all parameters have been varied, the total transmission uncertainty is calculated.

As a concrete example, the transmission uncertainty for ^{67}Cr and ^{54}K is shown in Figure 25, which shows the nine transmission values of Figure 24 in ascending order, from 1 (PSW defect = 1%) to 9 (target thickness -1%). Index 0 (orange point and line) represents the calculated median transmission of all nine points. This value becomes the new baseline for the cross section calculation. In this example, the medians for both ^{67}Cr and ^{54}K are nearly identical to the original baseline value. However, the median may move significantly for other isotopes. Calculating the median of all resultant transmissions indicates that we are taking the central value as the middle of all physically-reasonable outcomes.

The maximum and minimum transmission deviations are highlighted in red. These represent the final error bars of the transmission. This is the envelope of the total spread in transmission.

In the case of ^{67}Cr, the resulting transmission uncertainty spans multiple orders of magnitude, while the ^{54}K is well-constrained. This reflects the experimental reality that the fragment separator was tuned for ^{54}K, while ^{67}Cr was at the edge of acceptance.

When the propagated error dominates the cross section, the result may not be physically meaningful. Final acceptance or rejection of such isotopes should occur only after full cross section error propagation.

As this example illustrates, transmission effects frequently constitute the dominant source of uncertainty in rare isotope production cross section measurements. To obtain physically meaningful results, the parameter variations used in the transmission uncertainty evaluation must therefore remain within reasonable and defensible physical bounds:

- Material thickness: typically $\sim 1\%$ deviations

- Optics parameters: rarely more than 1–2%

Using excessively large variations artificially inflate the estimated uncertainties and consequently the cross section error.

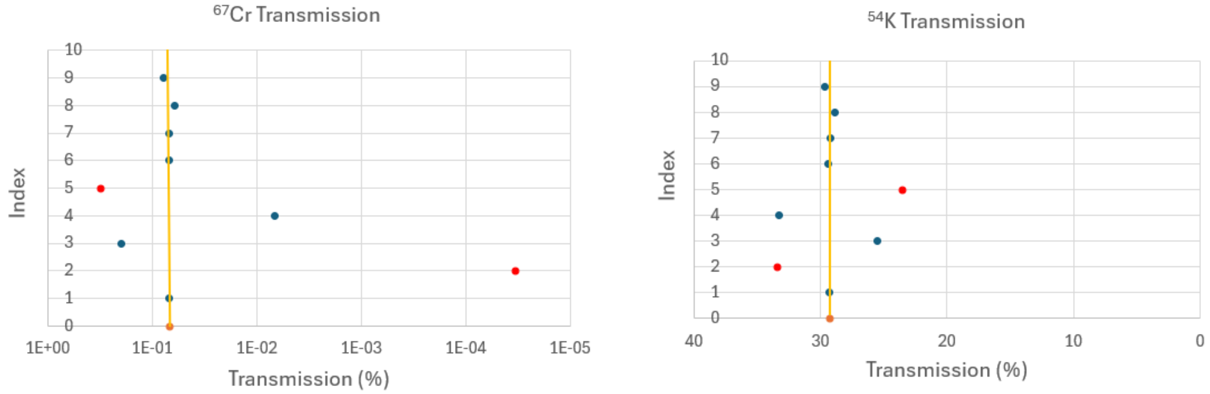

(a) Transmission deviations for ^{67}Cr, which was on the edge of acceptance.

(b) Transmission deviations for ^{54}K, which ARIS was tuned for.

Figure 25: Transmission uncertainty baseline and deviations for ^{67}Cr (panel **a**) and ^{54}K (panel **b**). The parameter indices (1–9) correspond to those in Fig. 24. The median transmission corresponds to index 0. The red points are the minimum and maximum transmission deviation. Note that the x-axis is inverted.

Final transmission-based exclusion: Fragments with predicted transmission below 0.1% are typically excluded. These isotopes lie at the edge of separator acceptance and are extremely sensitive to small parameter changes. This sensitivity often produces uncertainties spanning orders of magnitude (as in the ^{67}Cr example).

Low transmission does not imply low count rate; a sufficiently large production cross section can compensate for small acceptance. Conversely, high transmission does not guarantee high statistics, particularly for very neutron-rich isotopes.

Transmission analysis improves substantially with experience. Early analyses may require significant iteration. With familiarity, convergence toward physically reasonable solutions becomes faster and more systematic.

6 Cross Section Calculation

With all experimental inputs determined, the production cross section can now be calculated. This section connects the physical definition of a cross section to the experimentally measurable quantities derived in the preceding sections.

6.1 From First Principles to Measured Yields

The production cross section for a fragment F quantifies the probability that an interaction between an incident beam particle and a target nucleus produces that fragment. Formally, a reaction cross section relates the number of reactions to the incident flux and target density. For an infinitesimally thin target (no attenuation of beam or fragments), the total number of produced fragments is

$$Y_F = N_{\text{beam}}\, N_t\, \sigma_F, \tag{2}$$

where

- N_{beam} is the total number of incident beam particles,
- $N_t = n_t\, t$ is the areal density of the target (atoms/cm^2),
- σ_F is the production cross section.

If the target has finite thickness, the beam intensity decreases with depth due to nuclear reactions. The beam attenuation is governed by

$$\frac{dN_b}{dx} = -n_t\, \sigma_R^{(P)}\, N_b, \tag{3}$$

where

- N_b is the number of beam particles remaining at depth x,
- n_t is the target number density (nuclei/cm^3),
- $\sigma_R^{(P)}$ is the reaction cross section for the projectile for all non-elastic interactions with the target nuclei,
- x is the depth coordinate in the target.

Solving,

$$N_b(x) = N_{\text{beam}}\, e^{-n_t\, \sigma_R^{(P)}\, x}. \tag{4}$$

From Equation (4), the characteristic attenuation length is found to be

$$\lambda_{\text{int}}^{(P)} = \frac{1}{n_t\, \sigma_R^{(P)}}. \tag{5}$$

After the fragment F is produced, it must traverse the remaining thickness $t - x$. If the fragment interacts again, this secondary reaction decreases the production cross section[15]. Its survival probability is:

$$P_{\text{survival}}(x) = e^{-n_t\, \sigma_R^{(F)}\, (t-x)}, \tag{6}$$

where $\sigma_R^{(F)}$ is the reaction cross section for the fragment for all non-elastic interactions with the target nuclei.

---

[15] Conversely, fragment F may be created from the second reaction of fragment F', increasing the production cross section. Similarly, reactions in the wedge may create or destroy fragments. Accounting for secondary target reactions and reactions in the wedge is an important component of transmission analysis; see subsection 5.2

The number of fragments produced in a thickness element dx at depth x is

$$dY_F(x) = N_b(x)\, n_t\, \sigma_F\, P_{\text{survival}}(x)\, dx, \tag{7}$$

where σ_F is the production cross section for a specific fragment. Substituting Equations (4) and (6) into Equation (7) and integrating, we find

$$\begin{aligned} Y_F &= \int_0^t N_b\, e^{-n_t\, \sigma_R^P\, x}\, n_t\, \sigma_F\, e^{-n_t\, \sigma_R^F\, (t-x)}\, dx & (8)\\ &= N_b \frac{\sigma_F}{\sigma_R^P - \sigma_R^F} \left(e^{-n_t\, \sigma_R^F\, t} - e^{-n_t\, \sigma_R^P\, t} \right). & (9) \end{aligned}$$

The expression in Equation (9) accounts for both beam attenuation and fragment attenuation in the production target. The thin-target approximation may be recovered as $t \to 0$:

$$Y_F \approx N_b\, \sigma_F\, n_t\, t. \tag{10}$$

This approximation is valid when

$$t \ll \lambda_{\text{int}}^{(P)}.$$

In practice, this condition is satisfied when the target is a few percent of the interaction length. For all subsequent discussion, and throughout this manual, a sufficiently thin target will be assumed.

The reaction cross section for the fragment in Equation (10) is implicitly over all momenta and angles for which the reaction can take place:

$$\sigma_F = \iint \frac{d^2\sigma}{d\Omega\, dP}\, d\Omega\, dP. \tag{11}$$

The differential cross section in Equation (11) can be combined with the general formalism of Equation (10), along with a transmission function through the separation system. We explicitly include the charge-state acceptance, which is important for high-Z beams.

$$Y = N_{\text{beam}}\, N_{\text{t}} \int_{\Delta\theta} \int_{\Delta\phi} \int_{\Delta P} \int_{\Delta q} \frac{d^4\sigma}{d\theta\, d\phi\, dP\, dq}\, \xi(x',\, y',\, P,\, q)\, \sin(\theta)\, d\theta\, d\phi\, dP\, dq. \tag{12}$$

Equation (12) integrates over the solid angle of the fragment's distribution in angle and momentum. Additionally, we include an explicit function which takes into account all losses that occur as the fragments traverse the separator system.

To keep the notation clean, the angular acceptances of the separator are denoted by x' and y'. Because the acceptances of the separator system are presumed to be independent[16], the transmission function can be decomposed into the following components:

$$\xi(x',\, y',\, P,\, q) = \xi_{x'}\, \xi_{y'}\, \xi_P\, \xi_q. \tag{13}$$

---

[16] This assumption only holds in the case of abrasion-ablation, as shown in Figure 26. In abrasion-fission, there is strong correlation between the fragments' momentum and angle.

In typical rare-isotope production experiments, the separator integrates over much of the angular distribution. Detector efficiencies, geometrical and momentum acceptance, and analysis cuts are folded into a single transmission factor ξ[17]. The extracted cross sections are therefore partial cross sections over the experimentally accepted phase space (see subsection 7.1 and Appendix F).

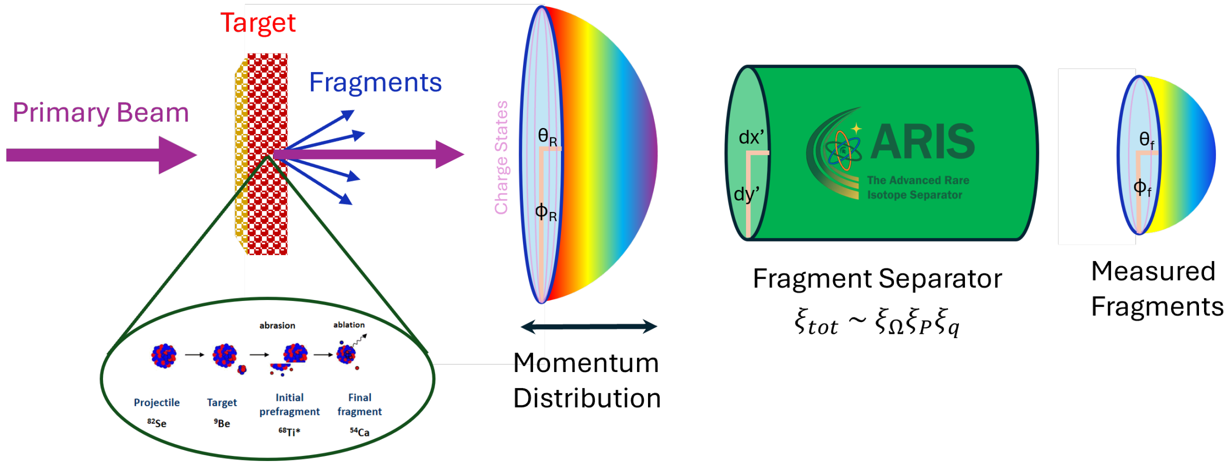

Figure 26: Schematic illustration of fragment production and transmission through ARIS. The fragments are produced with a certain angular spread (θ_R and ϕ_R) and momentum spread (purple for high momenta (close to primary beam) and red for low momenta (energy loss straggling)). Charge states are represented as light purple concentric shells in the fragment distribution. ARIS has an angular, momentum, and charge-state acceptance. This determines the measured fragments' final angular distribution (θ_f and ϕ_f), momentum distribution, and charge state.

Equation (12) is evaluated in `LISE`$^{++}$ using the distribution method. The result is

$$Y = N_{\text{beam}}\, N_{\text{t}}\, \xi\, \sigma(P), \tag{14}$$

where the measured cross section is done so at a small momentum range[18]. Due to the complex nature of separation in the system, the `LISE`$^{++}$ Monte Carlo calculations are recommended as a check on the distribution method's results.

Equation (14) may be rearranged into the form

$$\sigma(P) = \frac{Y}{B_{\text{int}}\, N_t\, \xi}, \tag{15}$$

where N_{beam} has been replaced by the beam integral B_{int} and $n_t\, t$ has been replaced by the areal density N_t (atoms/cm^2). Equation (15) is the working formula used throughout this manual.

Before evaluating Equation (15), verify unit consistency:

- Y and B_{int} in counts,

---

[17] See section 5

[18] This is the partial vs. total cross section discussion in subsection 7.1

- N_t in atoms/cm^2,
- ξ dimensionless.

Cross sections are generally reported in millibarns (mb). If Equation (15) is evaluated using CGS units (cm^2), multiply the result by 10^{27} to convert to millibarns (1 mb = 10^{-3} b = 10^{-27} cm^2).

6.2 Uncertainty Propagation

Each term in Equation (15) carries an uncertainty. These fall into three categories:

- **Statistical uncertainty** – yield counting statistics (Y),
- **Isotope-dependent systematic uncertainty** – transmission (ξ),
- **Global systematic uncertainty** – target areal density (N_t) and beam integral (B_{int}).

Assuming the uncertainties are independent and sufficiently small, standard error propagation gives:

$$\frac{\Delta\sigma}{\sigma} = \sqrt{\left(\frac{\Delta Y}{Y}\right)^2 + \left(\frac{\Delta\xi}{\xi}\right)^2 + \left(\frac{\Delta N_t}{N_t}\right)^2 + \left(\frac{\Delta B_{\text{int}}}{B_{\text{int}}}\right)^2}. \tag{16}$$

Because transmission uncertainties are frequently asymmetric, the positive and negative uncertainties are evaluated separately using Equation (16).

All uncertainty contributions should be documented separately. This ensures transparency and facilitates comparison with previous measurements.

6.3 Uncertainty Summary

For clarity, the estimation procedure for each uncertainty component is summarized below.

- **Isotope Yield** Y
  - For $Y > 20$, the uncertainty can be approximated as $\Delta Y = \sqrt{Y}$.
  - For $Y \leq 20$, Poisson statistics must be applied using the specialized corrections summarized in Table 1.
- **Transmission** ξ
  - Recalculate transmission after varying each adjusted simulation parameter within physically defensible bounds.
  - For each isotope, the maximum and minimum transmission deviations are the error bounds, as illustrated in Figure 25.
- **Target Areal Density** N_t

  - Use the defect parameter adopted in the baseline `LISE`$^{++}$ solution.
  - Physically, this uncertainty reflects manufacturing tolerances, non-uniformity across the target area, and measurement error.

- **Beam Integral** B_{int}
  - When correctly integrated, this uncertainty is typically small.
  - A conservative estimate treats the largest negative power fluctuation as the per-point uncertainty and propagates it through the trapezoidal integration.

7 Interpretive Analysis

At this stage, production cross sections and their uncertainties have been extracted. The experimental phase is complete. What follows is interpretation and model comparison.

The remainder of this manual focuses on placing the newly measured cross sections in a broader physical context. In particular, this section guides a first-time researcher through the two most common post-analysis studies performed with production cross sections:

- Abrasion–ablation (AA) modeling [16]
- ΔBE systematics [5]

Before performing model comparisons, the first diagnostic step is visualization. Plot cross sections grouped by atomic number Z as a function of mass number A. Along a given isotopic chain, cross sections should vary smoothly. Discontinuities or sharp kinks often indicate upstream issues such as misidentification, over-cleaning, or incorrect transmission corrections.

There are, however, important and physically meaningful exceptions to this expectation. Odd–even staggering effects are commonly observed, particularly in neutron- or proton-rich regions. Unbound nuclei produce genuine gaps in isotopic chains, and shell or deformation effects can introduce local structure in otherwise smooth trends. An example of such behavior is shown in Figure 27 for the heaviest isotopes in the titanium isotopic chain.

In some cases, individual cross sections may be excluded from further analysis. This is most often necessary for fragments with very large relative uncertainties, which typically arise from small transmissions or extremely low statistics. Exclusion should be conservative and well-documented; questionable points are often more valuable as diagnostics than as final results.

Once the internal consistency of the data set has been verified, comparisons to previous measurements should be performed. Plot the new results alongside published cross sections for the same isotopes and perform an initial visual comparison. Agreement within quoted uncertainties is expected but not guaranteed. If significant discrepancies are observed, the affected isotopes should be flagged and the analysis carefully reviewed. Subtle errors – particularly in PID, transmission, or yield extraction – often only become apparent at this stage.

If no errors are identified, discrepancies may reflect genuine experimental differences. The most common sources include variations in primary beam energy, target material or thickness, and experimental acceptance. Such differences must be considered carefully before drawing physical conclusions from comparisons across experiments.

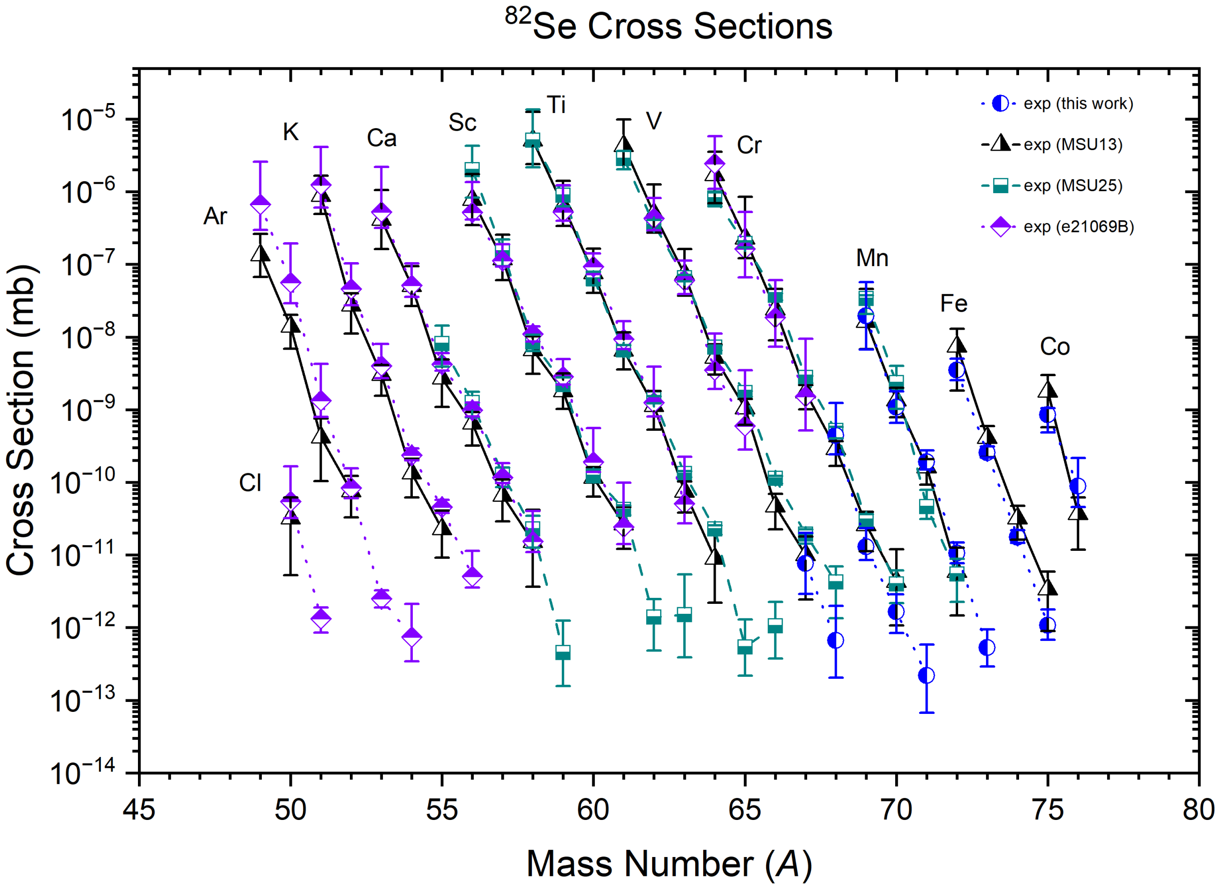

Figure 27: Cross sections from multiple experiments plotted together. From the reaction ^{82}Se on carbon. Data from Refs. [5, 16] and manuscript in preparation.

7.1 Partial vs. Total Cross Sections

In projectile fragmentation experiments, the term cross section is used in several closely related but distinct ways. Clarifying this terminology is essential for correctly interpreting experimental results and for making meaningful comparisons to previous measurements and theoretical models.

Throughout this manual, the cross section calculated using Equation (15) represents a **partial cross section**. This quantity corresponds to the yield of a given fragment measured within a specific experimental acceptance and at a fixed magnetic rigidity. It reflects the fragment production rate sampled over a limited region of momentum space defined by the separator optics and analysis gates.

In contrast, the **total production cross section** for a fragment is, in principle, defined as the integral of the differential cross section over all emission angles and momenta. In practice, however, projectile fragmentation experiments rarely measure this quantity directly[19].

For the purposes of this manual, and consistent with standard experimental practice, the total cross section is defined as the cross section integrated over the fragment's longitudinal momentum distribution. This is achieved by repeating the cross section measurement at multiple magnetic rigidities ($B\rho$), each of which samples a different portion of the fragment's momentum distribution [19]. The resulting partial cross sections are then combined – typically by fitting the momentum distribution and integrating – to obtain an estimate of the total production cross section.

Under typical intermediate- and high-energy fragmentation conditions, fragments are strongly forward-focused and their angular distributions are narrow. When the angular acceptance of the separator is sufficiently large and the transmission parameter of the partial cross section includes the momentum acceptance, integrating over the longitudinal momentum effectively captures the dominant contribution to the total yield. In this regime, the momentum-integrated cross section provides a reliable approximation to the formal total production cross section defined in Equation (12).

It is important to emphasize that a single cross section measurement, as derived in this manual, should always be interpreted as a partial cross section. Only by performing the analysis at three or more magnetic rigidity settings – and accounting for transmission and acceptance effects – can a total cross section be extracted. The procedures for momentum scans[20], fitting, and integration are experiment-specific and are therefore deferred to Appendix F.

This distinction is particularly important when comparing cross sections between experiments. Apparent discrepancies may arise if measurements from different locations along the momentum distribution are compared, or if differences in acceptance and transmission are not consistently treated.

7.2 Weighted Cross Sections

After comparison with previously measured data, the next step is to calculate the weighted cross sections. The resulting values incorporate all available measurements and their associated uncertainties into a single representative cross section for each isotope.

The advantage of weighting multiple measurements is that, when the reported cross sections are statistically consistent (i.e., their mean values agree within uncertainty), the combined uncertainty on the weighted mean can be reduced relative to the individual measurements. This reflects the improved precision obtained by combining independent determinations of the same physical quantity.

The weighting and averaging are performed using the `lise64 S_ArrayAsymErrorLog_Transpose` function.

This function accepts, for each measurement (one per row):

- the central cross section value,

---

[19] Experiments have been performed to explicitly measure the total cross section. See, for example, Refs. [17, 18]

[20] Also called $B\rho$ scans.

- the negative uncertainty,
- the positive uncertainty,
- and a weight.

Note the specified order. The function returns the combined cross section and its associated asymmetric uncertainties (indexed 0-2):

```
=S_ArrayAsymErrorLog_Transpose(<outputIndex>, <meanCol>, <nErrCol>,
                               <pErrCol>, <weightCol>)
```

Mathematically, the procedure is carried out in logarithmic space. Each cross section and its asymmetric uncertainties are transformed to log space, where the averaging is computed. Under this formulation, the logarithms of the cross sections are treated as normally distributed measurements of a single true log-value. The weighted average in log space therefore corresponds to the maximum likelihood estimator (MLE) of the underlying true logarithmic cross section.

The final reported cross section is obtained by exponentiating this estimator. Consequently, the returned central value corresponds to the exponentiated MLE (equivalently, the median of the implied log-normal distribution), rather than the arithmetic mean in linear space.

Working in log space is appropriate because cross sections are strictly positive quantities and frequently span multiple orders of magnitude. This approach naturally treats uncertainties as fractional (multiplicative) and preserves asymmetry when transforming back to linear space.

The inputs are treated as independent measurements of a single underlying true value. The returned uncertainty therefore represents the uncertainty on the inferred value of that true cross section, not the spread of the individual measurements.

The weights should reflect the relative precision of the measurements. Measurements with larger uncertainties should contribute less to the combined result than those with smaller uncertainties.

This calculation should be performed for every isotope with more than one independent cross section measurement. The resulting weighted cross sections are then used as inputs to the subsequent abrasion–ablation and ΔBE analyses. An example of the final weighted cross sections is shown in Figure 34, where the individual inputs are shown in Figure 27.

7.2.1 Convolution of Asymmetric Distributions

An aside is warranted regarding the convolution of asymmetric probability distributions. While the discussion above concerning weighted cross sections represents an analytical treatment, analogous statistical approaches are useful in other contexts, such as those described in Ref. [20].

When combining two independent quantities with asymmetric uncertainties, the resulting distribution depends on how the parent distributions are defined. For symmetric Gaussians, the mean, median, and mode coincide and convolution is uniquely defined. For asymmetric distributions, however, these three statistical descriptors differ, and anchoring the distribution on one or another leads to distinct convolution results.

To explore these differences systematically, an Excel spreadsheet, `Error_analysis_v7_x64`, has been developed to perform numerical convolutions under several statistical assumptions.

The spreadsheet accepts as input, for each distribution:

- the mode (used to define the peak location),
- the left standard deviation σ_L,
- the right standard deviation σ_R, and
- a statistical weight.

Each distribution is constructed as a piecewise Gaussian of the form

$$f(x) = \begin{cases} \exp\left[-\frac{(x-\theta)^2}{2\sigma_L^2}\right], x < \theta \\ \exp\left[-\frac{(x-\theta)^2}{2\sigma_R^2}\right], x \geq \theta, \end{cases} \tag{17}$$

where θ is taken to be the mode unless otherwise specified. Because $\sigma_L \neq \sigma_R$, the distribution is skewed and its mean, median, and mode are not identical.

Based on the input distributions, five convolution procedures are implemented:

1. **Symmetric convolution** – each asymmetric distribution is replaced by a symmetric Gaussian with an effective variance, and standard Gaussian convolution is applied.
2. **Mode-based asymmetric convolution** – distributions are centered on their modes prior to convolution.
3. **Mean-based asymmetric convolution** – distributions are shifted so that the expectation value defines the central location. Because expectation values are additive under convolution,
$$E[X + Y] = E[X] + E[Y],$$
this method preserves linear propagation of central values.
4. **Median-based asymmetric convolution** – distributions are centered on their medians, so that 50% of the probability lies on either side of the quoted central value.
5. **Analytical solution** – calculated using the `lise64 S_ArrayAsymErrorLog _Transpose` function, which implements the logarithmic asymmetric error propagation formalism.

The resulting central values and asymmetric uncertainties differ between these approaches, as can be seen in Figure 28. These differences are statistically meaningful because each method corresponds to a different definition of the "central value" being propagated:

- The **mean-based convolution** propagates expectation values and is consistent with linear statistical addition.

- The **median-based convolution** propagates quantiles and is robust to tail asymmetry.
- The **mode-based convolution** propagates most-probable values and emphasizes peak location. This is most similar to the **analytic method**.
- The **symmetric approximation** suppresses skew information.

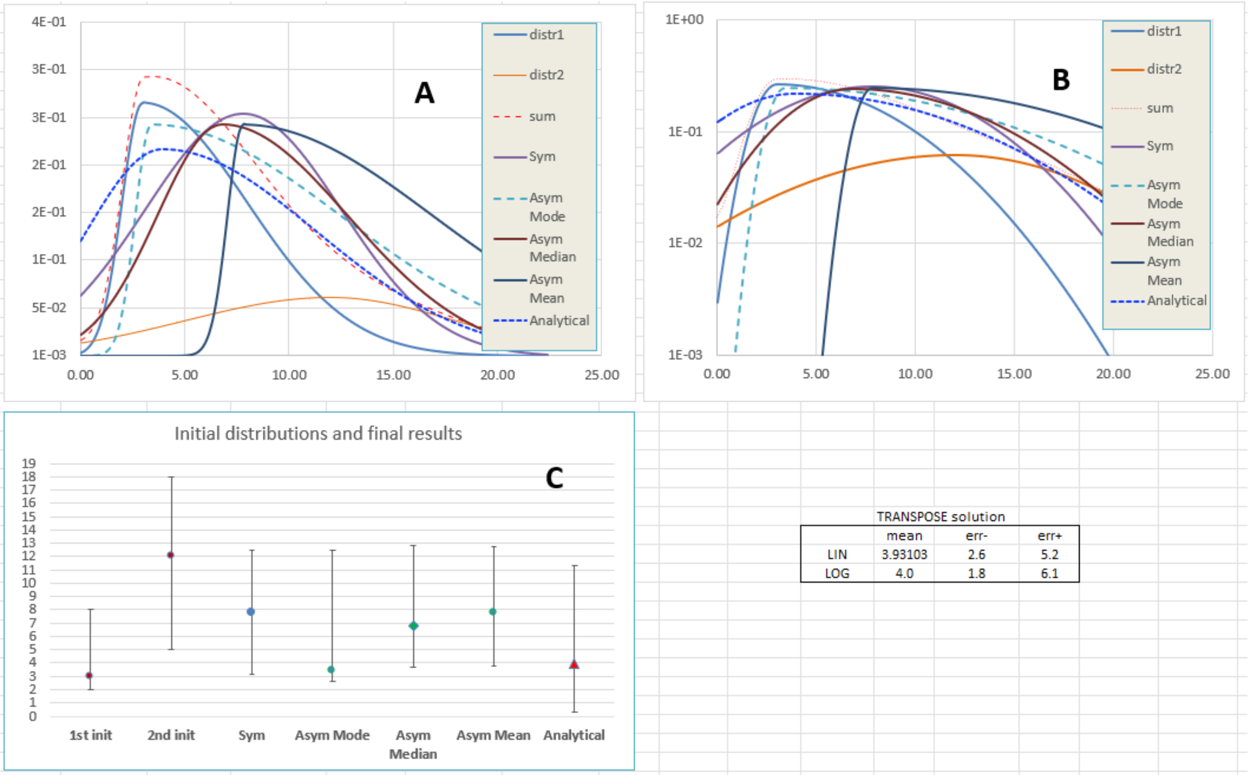

TRANSPOSE solution

	mean	err-	err+
LIN	3.93103	2.6	5.2
LOG	4.0	1.8	6.1

Figure 28: The results of the symmetric and asymmetric convolution methods, as well as the analytical solution. Graphs **A** and **B** show the Gaussians on linear and log scales, respectively. Graph **C** shows the 1D uncertainty equivalents.

For symmetric input distributions, all methods converge to the same result. As asymmetry increases (i.e., as the ratio σ_L/σ_R deviates from unity), the methods diverge in both the resulting central value and the quoted upper and lower uncertainties. The magnitude of this divergence provides a qualitative measure of the statistical sensitivity to skewness assumptions.

From a statistical perspective, the choice of convolution method should be guided by the interpretation of the input distributions and the intended meaning of the output central value and uncertainties:

- **Mean-based convolution** is appropriate when the input quantities represent expectation values or when additive propagation of uncertainties is desired. This method provides a statistically consistent central value that reflects the long-term average of repeated measurements.

- **Median-based convolution** is suitable when robustness to skew or outliers is important, or when the goal is to identify the central value that splits the probability distribution in half. It is particularly useful when reporting a “typical” outcome rather than an expectation.

- **Mode-based convolution** is best applied when the input distributions reflect the most probable observed value or when emphasizing peak likelihood is desired. This approach highlights the region of maximum probability density but may underrepresent contributions from tails.

- **Symmetric convolution** may be used when skew is negligible or when a simplified, approximate treatment of uncertainties is sufficient. It reduces the input distributions to an effective Gaussian, suppressing asymmetry information.

In all cases, the differences between methods are meaningful: they quantify how the statistical characterization of asymmetry affects the resulting central value and error intervals, and they allow the analyst to select the propagation method that aligns with the intended interpretation of the data.

7.3 Abrasion-Ablation

Abrasion–ablation is a widely used reaction model for describing intermediate- and high-energy projectile fragmentation [21]. In this framework, the reaction is separated into two conceptually distinct stages: **abrasion**, in which nucleons are rapidly removed from the projectile nucleus due to its geometric overlap with the target, and **ablation**, in which the highly excited projectile-like remnant de-excites through particle emission.

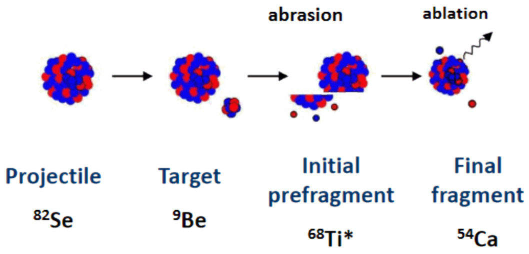

Figure 29: Schematic illustration of the abrasion–ablation process.

During the abrasion stage, the projectile and target pass through one another on a timescale of order 10^{-22} s. Nucleons located in the geometric overlap region are removed from the projectile, while the remaining nucleons form a projectile-like pre-fragment. To first order, the number of abraded protons and neutrons is determined by the impact parameter of the collision and the nuclear density distributions of the projectile and target[21]. This stage is essentially a fast, non-equilibrated process, and the resulting pre-fragment retains approximately the forward velocity of the original projectile.

The sudden removal of nucleons leaves the pre-fragment in a highly excited state, with excitation energy that scales with the number of abraded nucleons. In the subsequent ablation stage, this excess energy is dissipated through the statistical emission of light particles –primarily neutrons, but also protons and light clusters at higher excitation energies. This

---

[21] Note that the impact parameter must be large. Small impact parameters usually lead to complete destruction of the projectile nucleus.

de-excitation occurs on a longer timescale ($\sim 10^{-19}$–10^{-16} s) and drives the pre-fragment toward the final observed residual nucleus.

Following particle evaporation, the residual fragment may still populate long-lived excited or isomeric states. On even longer timescales, these states can decay via γ-ray emission, which can be observed experimentally using ancillary detector systems. While this electromagnetic decay does not alter the mass or charge of the fragment, it can provide valuable spectroscopic information and, in some cases, serve as an additional handle for particle identification.

A schematic overview of the full abrasion–ablation sequence is shown in Figure 29. In practice, this model provides an intuitive and effective framework for interpreting isotopic production cross sections and for connecting measured yields to underlying reaction mechanisms. Subsequent sections build on this picture to compare experimental cross sections with abrasion–ablation–based calculations and systematics.

7.3.1 Dissipation and Friction

Between the abrasion and ablation stages of the abrasion-ablation model, an additional interaction regime may contribute to the excitation and kinematic properties of the pre-fragment. Within the simplified framework described above, this intermediate stage is largely neglected. Nevertheless, it can play an important role by modifying both the excitation energy generated during abrasion and the subsequent particle emission during ablation.

During the collision of the projectile and target nuclei, the geometrical overlap region persists for a finite interaction time and may experience nuclear friction [22]. This friction is proportional to both the degree of geometrical overlap and the duration of the overlap. Microscopically, it arises from nucleon-nucleon interactions within the overlap region. These interactions dissipate kinetic energy, converting a portion of the relative motion of the projectile into internal excitation energy of the pre-fragment. As a result, the excitation energy entering the ablation stage is increased, enhancing the probability for light-particle emission and thereby modifying final fragment yields.

When the interaction is treated as non-instantaneous, this intermediate stage also provides a natural mechanism for nucleon pick-up processes from the target. This is seen experimentally, as in Figure 34. Such processes are difficult to reconcile within a purely sudden abrasion picture but arise naturally when finite interaction times and dissipative effects are included.

Experimental signatures of frictional dissipation extend beyond total production cross sections. In particular, the low-momentum tail of fragment longitudinal momentum distributions has been attributed, in part, to energy-loss arising from nuclear friction[22]. Increasing friction leads to a broadening of this tail, which in turn enhances production cross sections at momenta lower than those predicted by purely geometric abrasion models.

In `LISE`$^{++}$, the geometrical model of Wilson, Townsend, and Badavi [23] incorporates additional excitation energy arising from frictional dissipation. In this formulation, the total excitation energy of the pre-fragment is expressed as

$$E^{*} = (\gamma\, f\, \Delta S)_{\text{geom}} + E_{\text{friction}}, \tag{18}$$

---

[22] `https://lise.frib.msu.edu/paper/2006_09_acs_pf.pdf`

where γ is the surface energy (MeV/fm^2), f is a correction factor accounting for surface distortion effects, and ΔS is the excess surface area of the pre-fragment immediately following abrasion relative to a sphere of equal volume. The correction factor f depends on the number of abraded nucleons.

The additional excitation energy due to friction is parameterized as

$$E_{\text{friction}} = k_1\, C_p + k_2\, C_p\, C_t, \tag{19}$$

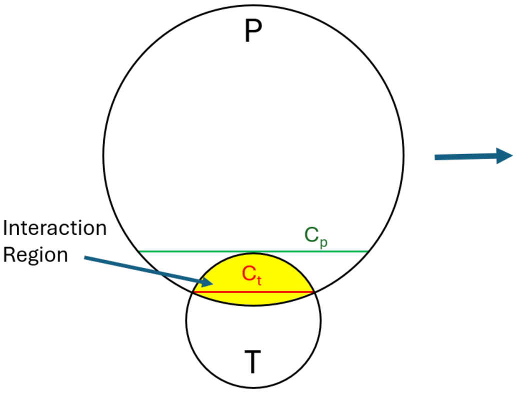

Figure 30: Geometry of a simple abrasion-ablation model at maximum overlap. The chords used for a simple friction calculation are shown.

where C_p is the length of the longest chord at the projectile surface interface (green line, in Figure 30), C_t is the chord of intersection between the projectile and target (red line, in Figure 30), and k_1 and k_2 are phenomenological coefficients. This formulation provides an intuitive geometrical link between the collision geometry and the resulting dissipative excitation.

For typical FRIB beam energies ($\sim$ 150-400 MeV/u) and light production targets (e.g. carbon), the contribution from frictional excitation is expected to be small. The high beam velocity and limited geometrical overlap result in short interaction times and minimal dissipation. Nonetheless, the explicit inclusion of friction highlights a physical mechanism that is absent from many modern excitation-energy prescriptions. Modern rare isotope production increasingly relies on extrapolations across beam energy, target material, and reaction systematics, where small effects at high energy can evolve into non-negligible contributions under different conditions.

Incorporating friction provides a more complete and internally consistent description of the collision dynamics, ensuring that excitation-energy models remain valid beyond the narrow regime in which they were tuned. Moreover, even weak dissipative effects can influence subtle observables such as the low-momentum tails of fragment distributions and the population of marginally bound species, which are particularly relevant for precision cross section predictions.

Including friction therefore improves the predictive robustness of excitation-energy prescriptions in `LISE`$^{++}$ and strengthens confidence in their applicability across current and future experimental programs.

7.3.2 Abrasion-Fission

As will be discussed in paragraph 7.3.4.3, there are several possible de-excitation channels available to an excited pre-fragment following the abrasion step. For sufficiently heavy primary projectiles, and for pre-fragments with large excitation energies, fission can become the dominant de-excitation mechanism. In this reaction pathway, the projectile first undergoes abrasion, producing a highly excited heavy pre-fragment, which subsequently fissions into two primary fragments. Each fission product may retain a significant amount of excitation energy and can undergo further particle evaporation before reaching its final bound state. This reaction mechanism is illustrated schematically in Figure 31.

Figure 31: Schematic illustration of the abrasion-fission process.

In `LISE`$^{++}$, fission following abrasion is treated as a stochastic decay channel whose probability depends on the mass, charge, and excitation energy of the pre-fragment[23,24]. Detailed descriptions of the fission modeling implemented in `LISE`$^{++}$, including the treatment of fragment yields and kinematics, can be found in Refs. [7, 12, 13]. While abrasion-ablation dominates the production of fragments close in mass to the projectile, abrasion-fission plays a crucial role in accessing neutron-rich nuclei where direct fragmentation cross sections may be vanishingly small.

From an experimental perspective, abrasion-fission introduces several important complications for particle identification and transmission. In the rest frame of the fissioning nucleus, the two primary fission fragments are emitted nearly isotropically, populating a spherical shell in velocity space. When boosted into the laboratory frame, this distribution becomes strongly elongated along the beam axis, forming an ellipsoidal shell in momentum space. As a consequence, a significant fraction of the fission fragments are emitted at large angles relative to the beam direction, in contrast to projectile fragmentation residues, which are strongly forward-focused. The momentum space shell reconstruction of krypton isotopes created in the fission of uranium are shown in Figure 32.

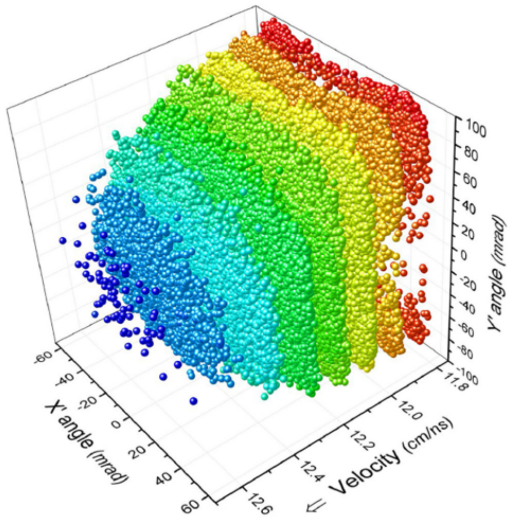

Figure 32: Reconstruction of momentum space as a function of transverse angle of krypton fragments from the fission of uranium. From Ref. [7].

The first implication of this kinematic structure is that only a subset of fission products fall within the angular acceptance of a fragment separator. Experiments relying on abrasion-fission therefore require large transverse acceptance to efficiently transmit the desired fragments, and the measured yields are particularly sensitive to the optical settings and acceptance modeling of the separator.

A second complication arises from the broad longitudinal momentum distribution of the fission fragments. Fragments emitted forward and backward in the fissioning nucleus rest frame can possess identical proton and neutron numbers, but markedly different laboratory-frame velocities. Because magnetic rigidity and time-of-flight measurements are both velocity-dependent, fragments with the same Z and A can populate different regions of PID space.

---

[23] `https://groups.frib.msu.edu/nscl_library/nscl_preprint/MSUCL1299.pdf`

[24] `https://lise.frib.msu.edu/7_5/lise++_7_5.pdf`

In extreme cases, backward-emitted fragments may be misidentified or fall outside the nominal PID gates defined for forward-emitted residues. Careful trajectory reconstruction, charge-state separation, and acceptance corrections are therefore essential when interpreting abrasion-fission data.

In spite of these experimental challenges, abrasion-fission remains a powerful production mechanism for rare isotopes. When properly modeled and corrected for acceptance effects, fission-based production enables access to regions of the nuclear chart that are otherwise unreachable with standard abrasion-ablation reactions, and it plays a central role in many current and planned rare isotope experiments at FRIB.

7.3.3 Abrasion–Ablation Calculations in `LISE`$^{++}$

The abrasion-ablation (AA) calculations implemented in `LISE`$^{++}$ apply the reaction model described above to predict fragment production cross sections for a given projectile-target system[25]. In practice, the calculation folds together several physical ingredients that govern (i) how a pre-fragment is formed during abrasion and (ii) how that pre-fragment subsequently de-excites through particle evaporation. Many of these ingredients introduce parameters that can be adjusted during fitting to better reproduce experimental data.

The most important model components and user-controlled inputs are summarized below, along with their physical motivation and typical role in the fitting process.

Nuclear Mass Model

The nuclear mass model provides tabulated values of nuclear masses and derived quantities such as binding energies, neutron and proton separation energies, and Q-values for particle emission. These quantities enter directly into the ablation stage, where they determine which evaporation channels are energetically allowed and how probable they are.

In `LISE`$^{++}$, experimentally measured masses are taken from the 2020 Atomic Mass Evaluation (AME2020) wherever available [24]. For nuclei beyond the reach of experimental mass measurements, theoretical mass models are used to supply the missing values. Among these, the Hartree-Fock-Bogoliubov HFB22 mass model [25] is the most commonly employed due to its global coverage and reasonable performance across much of the nuclear chart.

Because separation energies strongly influence evaporation probabilities, the choice of mass model can have a noticeable effect on predicted cross sections, particularly for very neutron-rich or proton-rich fragments. This sensitivity underlies the connection between cross sections and nuclear binding systematics discussed in the ΔBE analysis.

Particle Evaporation Channels

The particle evaporation settings define which light particles are permitted to be emitted during the ablation stage. By default, `LISE`$^{++}$ allows evaporation of neutrons, protons, and α particles, which are the dominant de-excitation modes for most projectile-like pre-fragments at intermediate energies.

---

[25] See https://lise.frib.msu.edu/AA for more details.

If the excitation energy of the pre-fragment is sufficiently high, additional channels may become relevant. For heavy systems, fission can compete with particle evaporation, while at very high excitation energies multifragmentation or breakup processes may occur. Enabling or disabling specific evaporation channels effectively constrains how the pre-fragment sheds energy and mass, and therefore influences the final isotopic distributions.

Excitation Energy of the Pre-Fragment

The excitation energy imparted to the pre-fragment during abrasion is one of the most influential inputs to AA calculations. Physically, this excitation energy arises from the sudden removal of nucleons, which disrupts the mean field and leaves the remaining nucleus far from equilibrium. To first order, the total excitation energy scales with the number of abraded nucleons.

Within `LISE`$^{++}$, several parameterizations are available to describe this excitation energy. The simplest is the Gaimard–Schmidt model, which assigns an average excitation energy per abraded nucleon [26]. More sophisticated treatments introduce statistical distributions of excitation energy, allowing event-by-event fluctuations around a mean value.

The most commonly used option in practical analyses is the exponential mean-T model [27], which characterizes the excitation energy distribution in terms of an effective temperature. Increasing the excitation energy generally increases the probability of emitting multiple neutrons, thereby shifting the predicted fragment yields toward lower mass numbers along a given isotopic chain.

Effective Coulomb Barrier

The effective Coulomb barrier parameter modifies the probability for charged-particle evaporation, particularly proton and α emission. Physically, it reflects the electrostatic repulsion experienced by charged particles attempting to escape the nuclear potential well.

In `LISE`$^{++}$, this parameter effectively sets a charge radius for the pre-fragment and therefore controls the height of the Coulomb barrier. Adjusting this parameter primarily impacts proton-rich fragments and can be important when reproducing yields on the proton-deficient side of the projectile.

Odd-Even Effect

Experimental cross sections often exhibit odd-even staggering, especially near the drip lines, where nuclei with paired protons and neutrons are systematically more bound than their odd-Z or odd-N neighbors. This behavior originates from nucleon pairing correlations.

The odd-even parameter in `LISE`$^{++}$ introduces a phenomenological correction to reproduce this staggering in calculated cross sections. While not derived from first principles, it provides a practical means of capturing pairing effects that are otherwise smeared out in purely statistical evaporation models.

Breakup Limiting Temperatures

At sufficiently high excitation energies, a pre-fragment may no longer be well described as a compound nucleus undergoing sequential evaporation. Instead, it may undergo complete breakup into its constituent nucleons or light clusters. To prevent unphysical evaporation chains, `LISE`$^{++}$ introduces limiting temperatures that cap the excitation energy available for standard ablation processes.

These breakup limiting temperatures act as free parameters during AA fits and effectively regulate the transition between evaporation-dominated de-excitation and more violent disassembly modes. While somewhat phenomenological, they play an important role in stabilizing calculations at high excitation energies and improving agreement with experimental yields.

7.3.4 Performing Abrasion-Ablation Fits

The next step is to perform a fit that optimizes the model parameters to reproduce the measured cross sections. Because the fitting procedure can modify many interconnected quantities, it is strongly recommended to perform these calculations in a fresh `LISE`$^{++}$ file to avoid unintended carryover from previous analyses.

Begin by selecting the nuclear mass model (HFB22 is recommended unless a specific alternative is justified), importing the experimental cross sections, and choosing the excitation energy model (typically mean-T). When importing data, it is advantageous to combine newly measured cross sections with reliable literature values so that each isotopic chain spans as wide a range in neutron number as possible. Broad coverage helps constrain the excitation and evaporation parameters and reduces sensitivity to local statistical fluctuations.

To access the fitting interface, navigate to:

`Utilities` → `Reaction Utilities` → `User Cross Section Analysis` →
`Minimization of` E^* `Parameters`.

Upon opening this dialog, the `Fit` button may initially be disabled. This indicates that prerequisite internal quantities have not yet been initialized. These are generated automatically by selecting the `Make items 1-3` button located near the center of the dialog (Figure 33, **A**). Once these steps are completed, the fitting controls become available.

Underneath the `Make items 1-3` button is a `Pre-fragment Excitation Energy` button. This opens a dialog that allows you to define the excitation energy model.

A central aspect of the minimization procedure is the treatment of experimental uncertainties and the relative weighting of different isotopes (Figure 33, **B**). `LISE`$^{++}$ provides four objective-function components: global χ^2, local χ^2, and the corresponding logarithmic differences. The logarithmic terms are particularly important for fragmentation data, where cross sections often span many orders of magnitude. Without them, a fit driven purely by χ^2 would be dominated by the most abundant fragments and could fail to reproduce the rare, exotic isotopes that are often of greatest physical interest.

The *local line* selection, controlled by the button near Figure 33, **C**, determines which isotopic chain (or subset of chains) is emphasized during a given stage of the fit. `LISE`$^{++}$ also allows the local line to be cycled automatically: after a fixed number of iterations, the fit

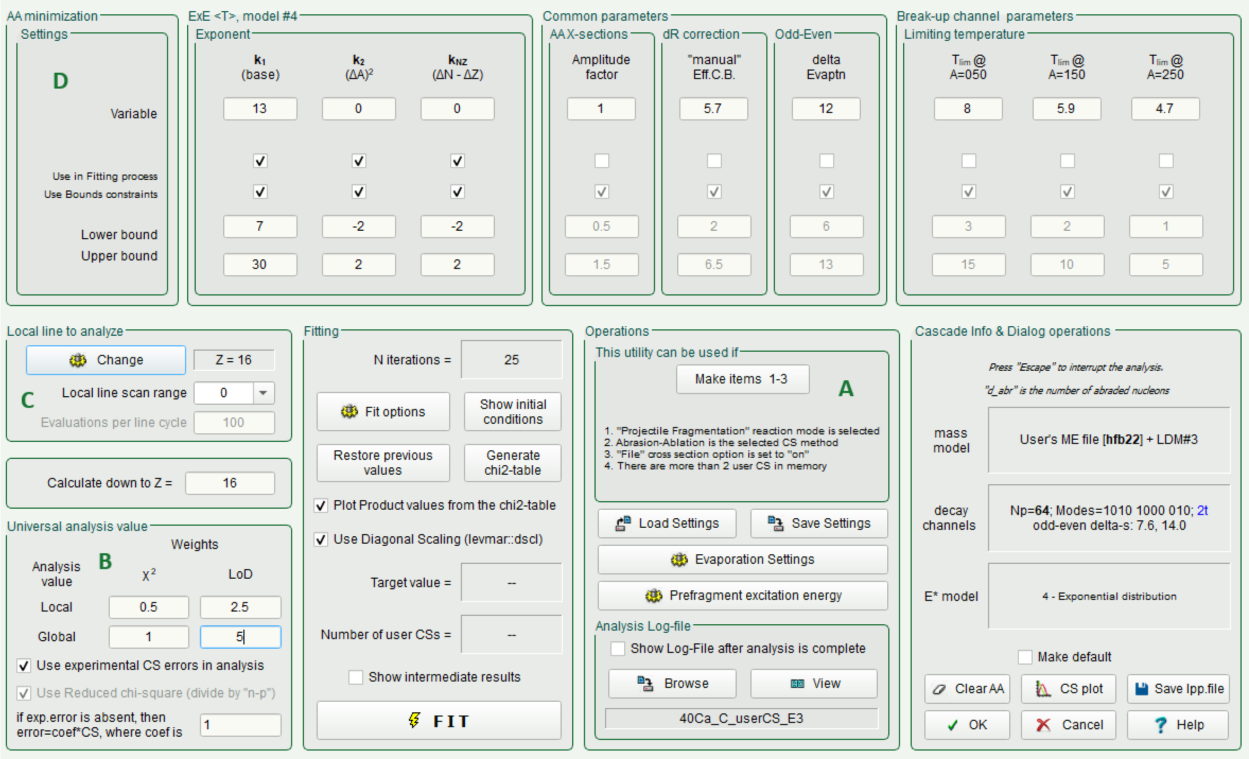

	ExE <T>, model #4 Exponent k_1 (base)	k_2 $(\Delta A)^2$	k_{NZ} $(\Delta N - \Delta Z)$	AA X-sections Amplitude factor	dR correction "manual" Eff.C.B.	Odd-Even delta Evaptn	Limiting temperature T_{lim} @ A=050	T_{lim} @ A=150	T_{lim} @ A=250
Variable	13	0	0	1	5.7	12	8	5.9	4.7
Use in Fitting process	☑	☑	☑	☐	☐	☐	☐	☐	☐
Use Bounds constraints	☑	☑	☑	☑	☑	☑	☑	☑	☑
Lower bound	7	-2	-2	0.5	2	6	3	2	1
Upper bound	30	2	2	1.5	6.5	13	15	10	5

Local line to analyze: Z = 16
Local line scan range: 0
Evaluations per line cycle: 100
Calculate down to Z = 16

Universal analysis value

Analysis value	Weights χ^2	LoD
Local	0.5	2.5
Global	1	5

☑ Use experimental CS errors in analysis
☑ Use Reduced chi-square (divide by "n-p")
if exp.error is absent, then error=coef*CS, where coef is 1

Fitting
N iterations = 25
☑ Plot Product values from the chi2-table
☑ Use Diagonal Scaling (levmar::dscl)
Target value = --
Number of user CSs = --
☐ Show intermediate results

Operations
This utility can be used if
1. "Projectile Fragmentation" reaction mode is selected
2. Abrasion-Ablation is the selected CS method
3. "File" cross section option is set to "on"
4. There are more than 2 user CS in memory

Analysis Log-file
☐ Show Log-File after analysis is complete
40Ca_C_userCS_E3

Cascade Info & Dialog operations
Press "Escape" to interrupt the analysis.
"d_abr" is the number of abraded nucleons
mass model: User's ME file [hfb22] + LDM#3
decay channels: Np=64; Modes=1010 1000 010; 2t odd-even delta-s: 7.6, 14.0
E* model: 4 - Exponential distribution
☐ Make default

Figure 33: The abrasion-ablation fitting dialog in `LISE`$^{++}$. Key regions discussed in the text are labeled.

shifts its focus to neighboring isotopic chains (e.g., 16 → 17 → 15 → 16). This cycling helps prevent the minimization from becoming trapped in a local minimum dominated by a single chain and encourages a more globally consistent solution. Utilizing this feature is highly recommended. For small- and medium-sized data sets, a scanning range of ±1 is sufficient; for larger sets, ±2 or larger is recommended.

The parameters eligible for fitting are listed at the top of the dialog (Figure 33, **D**). In the example shown, the mean-T excitation energy model is selected, with its associated parameters exposed for adjustment. Although many parameters can be floated simultaneously, doing so is rarely optimal.

A practical and robust fitting strategy is to proceed incrementally:

- Begin by fitting only the base excitation parameter (k_1), which sets the overall scale of the excitation energy.
- Introduce higher-order terms (k_2 and k_3) sequentially to refine the curvature and width of isotopic distributions.
- Add the odd–even parameter to reproduce pairing-related staggering once the gross trends are established.
- Include the effective Coulomb barrier parameter to fine-tune proton-rich yields.

The breakup limiting temperatures may also be floated, but in most cases the default values provided by `LISE`$^{++}$ are robust. Large deviations from these defaults often signal that the fit has settled into an unphysical local minimum rather than uncovering genuine physics.

The final parameter to adjust should be the overall amplitude factor. This multiplicative scale shifts all calculated cross sections uniformly and is best optimized only after the relative shapes of the isotopic distributions are well reproduced. Adjusting the amplitude too early can mask deficiencies in the underlying model parameters and lead to misleading agreement.

7.3.4.1 Physical Bounds for Fitting Parameters

Early in the abrasion-ablation fitting process, the numerical values of the fit parameters can appear abstract, and it is not always obvious what constitutes a *physically reasonable* solution. This subsection provides physical intuition and empirical guidance for interpreting the fitted parameters. The ranges quoted below are not strict limits, but rather typical values observed across many successful fits. Parameters that converge well outside these ranges should be treated as warning signs and examined critically.

- **k_1 (Base excitation energy per abraded nucleon)**

  In the mean-T excitation energy model, k_1 sets the average excitation energy deposited per abraded nucleon. Physically, it reflects the typical energy cost of removing a nucleon from the projectile during the abrasion stage and embedding it into an excited pre-fragment.

  This parameter depends on the mass and energy of the primary beam, as heavier projectiles generally generate more excitation per removed nucleon due to increased participant–spectator interactions. Across a wide range of intermediate-energy fragmentation experiments, acceptable values typically lie in the range

  $$15 \lesssim k_1 \lesssim 20 \text{ MeV}$$

  Values significantly below this range often underpredict particle evaporation, while values well above it tend to overbroaden isotopic distributions.

- **k_2 (Quadratic excitation term)**

  The k_2 parameter introduces a quadratic dependence of excitation energy on the number of abraded nucleons (ΔA^2). Physically, this term accounts for the fact that large overlaps between projectile and target produce disproportionately higher excitation energies than would be expected from a purely linear scaling.

  Empirically, k_2 is typically small, reflecting a modest correction rather than a dominant contribution. Reasonable values usually fall in the range

  $$0 \lesssim k_2 \lesssim 1$$

  Values outside this range often indicate that the fit is compensating for deficiencies elsewhere in the model.

- **k_3 (Isospin-dependent excitation term)**

  The k_3 parameter encodes an isospin dependence in the excitation energy, proportional to $(\Delta N - \Delta Z)$. This term reflects the differing nuclear interactions experienced by neutrons and protons during abrasion, including symmetry-energy effects.

  Fits across the nuclear chart show that k_3 is generally negative, indicating slightly reduced excitation for neutron-rich abrasion. Typical values lie in the range

  $$-1 \lesssim k_3 \lesssim 0$$

  Positive values are rarely physical and usually signal an unstable or poorly constrained fit.

- **Effective Coulomb Barrier**

  The effective Coulomb barrier parameter controls the suppression of charged-particle evaporation (primarily protons and α particles) during the ablation stage. Physically, it represents an effective charge radius and barrier height experienced by evaporating particles.

  This parameter decreases with increasing projectile mass, as larger systems have more diffuse charge distributions and lower effective barriers. Empirical fits suggest typical values in the range

  $$\text{Barrier} \approx 5 - 7$$

  with heavier beams favoring the lower end of this range.

- **Odd-Even Parameter**

  The odd-even parameter models the staggering observed in isotopic yields near the driplines, arising from nuclear pairing correlations. Its effect becomes most pronounced for nuclei where separation energies change rapidly with neutron or proton number.

  This parameter generally scales with projectile mass, reflecting stronger pairing effects in heavier systems. Reasonable values typically fall in the range

  $$\text{Odd-Even} \approx 6 - 12$$

  Unusually large values may indicate that the fit is attempting to reproduce fine structure that is not well supported by the data.

- **Limiting Temperatures**

  The limiting temperatures define the transition from sequential evaporation (ablation) to breakup or multifragmentation. Physically, they cap the temperature of the prefragment to prevent unphysical excitation energies.

  The default limiting temperatures provided by `LISE`$^{++}$ have been shown to be robust across much of the nuclear chart. Large deviations from these defaults are strongly discouraged, as they often indicate convergence to a nonphysical local minimum rather than genuine sensitivity to the data.

- **Amplitude Factor**

  The amplitude factor uniformly rescales all calculated cross sections. Ideally, this parameter should remain close to unity, indicating that the absolute normalization of the model is consistent with the experimental inputs.

  In practice, values in the range

  $$\text{Amplitude} \approx 0.8 - 1.2$$

  are considered acceptable. Larger deviations may arise, but should be treated skeptically.

Taken together, these parameter ranges provide a practical framework for assessing the physical plausibility of abrasion-ablation fits. A fit that reproduces the data well but yields parameters far outside these ranges should be treated with skepticism and revisited before being used for interpretation or extrapolation.

7.3.4.2 Diagnosing and Correcting Unphysical Fits

It is not uncommon for abrasion-ablation minimization to converge to a statistically acceptable solution (e.g., low global χ^2) while producing one or more parameters that lie outside physically reasonable bounds. Such outcomes typically indicate that the minimizer has compensated for deficiencies in the dataset or model assumptions rather than capturing the underlying reaction physics. The following diagnostic checks provide guidance for identifying and correcting these situations.

An important visual aid is the χ^2 table that `LISE`$^{++}$ generates at the conclusion of a fit. To see the χ^2 and logarithmic differences plot, click the `Generate chi2-table` in the `Fitting` box at the center of the dialog.

- **Unphysical excitation-energy parameters**: Extreme values of k_1, k_2, or k_3 (e.g., $k_1 \ll 15$, $k_2 > 1$, or $k_3 > 0$) often indicate insufficient isotopic coverage or strong parameter correlations. This most commonly arises when only mid-chain isotopes are included or when exotic tails are underweighted.
  - Fix higher-order parameters (k_2, k_3) at reasonable values and refit k_1 alone.
  - Expand or contract the dataset by including/excluding previous measurements or neighboring elements, even if uncertainties are larger.
  - Verify that the chosen excitation-energy model is appropriate for the projectile mass and beam energy.
- **Instability under local-line cycling**: Strong dependence of fitted parameters on the chosen local line or cycling pattern indicates an underconstrained fit or the presence of multiple local minima.
  - Reduce the number of free parameters.
  - Improve isotopic coverage before refitting.

  - Favor solutions that are stable across multiple cycling configurations.

- **Misleadingly good global χ^2:** A low χ^2 can mask systematic trends. Always inspect residuals along individual isotopic chains.
  - Look for systematic over- or under-prediction of neutron-rich or proton-rich tails.
  - Check for smooth reproduction of trends across neighboring elements.

In general, physically meaningful solutions are characterized by parameter values within established bounds, smooth reproduction of isotopic trends, and stability under reasonable variations of fitting strategy. When ambiguities persist, conservative exclusion of poorly constrained isotopes is preferable to propagating unphysical parameters into interpretation or extrapolation.

7.3.4.3 When to Enable Additional Evaporation Channels

The user-controlled evaporation settings in `LISE`$^{++}$ determine whether additional composite light-particle channels – specifically $2n$, $2p$, deuteron (d), and triton (t) emission – are permitted during the ablation stage. The decision to enable these channels should be guided by physical considerations, not solely by fit quality.

Under typical intermediate-energy projectile fragmentation conditions, de-excitation of the pre-fragment is dominated by sequential neutron evaporation, with proton and α emission contributing as excitation energy increases. Composite-particle channels such as $2n$, $2p$, d, and t represent higher-order decay modes that become relevant only when the excitation energy is sufficiently large to overcome their higher effective emission thresholds.

The need to study or enable these additional channels generally arises under the following conditions:

- The fitted excitation-energy parameters (e.g., k_1) imply excitation energies well above typical neutron-evaporation scales.
- Systematic discrepancies appear between measured and calculated cross sections for specific regions, particularly proton-rich isotopes or light fragments where cluster emission may compete with sequential evaporation.
- The fit reproduces neutron-rich isotopes well but consistently overpredicts yields closer to stability, suggesting that additional decay pathways may be draining population from those channels.
- The reaction involves light or medium-mass projectiles, where composite-particle emission is known to be more competitive at high excitation energies.

When these conditions are met, enabling composite evaporation channels should be treated as a controlled physics study rather than a default fitting step. Channels should be enabled incrementally, and their impact on both global fit quality and isotopic-chain behavior should be examined carefully. In particular, one should assess whether enabling a new channel leads to physically reasonable changes – such as selective suppression of specific isotopes – rather than a uniform rescaling of all cross sections.

It is important to recognize that opening additional evaporation channels can significantly alter the sensitivity of the fit to excitation-energy parameters. Apparent improvements in χ^2 may reflect compensating effects between channel competition and excitation energy, rather than a more accurate physical description. For this reason, enabling composite channels often necessitates revisiting previously fitted parameters to ensure they remain within physically meaningful bounds.

As a best practice, abrasion-ablation fits should first be stabilized using the minimal evaporation channel set (typically n, p, and α only). Composite channels ($2n$, $2p$, d, t) should then be enabled selectively and only when motivated by clear physical or systematic evidence. This approach preserves interpretability of the fit and avoids masking deficiencies in excitation-energy modeling or mass input with excessive decay freedom.

7.3.4.4 Determining a Global Minimum

The abrasion-ablation minimization procedure described above identifies a best-fit solution for a *single* choice of nuclear mass model and excitation-energy prescription. However, because the AA model is inherently multi-parameter and highly non-linear, a single minimization run does not guarantee convergence to the true global minimum.

Different nuclear mass models and excitation-energy parameterizations can lead to distinct local minima with comparable χ^2 values but different physical implications. To ensure that the extracted parameters and predictions are robust, it is therefore recommended to repeat the full minimization procedure using multiple mass models and, where appropriate, alternative excitation-energy models.

In practice, past analyses have found that the combination of the HFB22 mass model with the mean-T excitation-energy prescription provides the most consistent and physically reasonable description across large regions of the nuclear chart. Nevertheless, this outcome should not be assumed *a priori*. Different projectile masses, beam energies, or regions far from stability may favor alternative models.

The final abrasion-ablation prediction should be selected based on a combination of statistical quality (e.g., χ^2), physical plausibility of fitted parameters (see paragraph 7.3.4.1), and stability of the solution across repeated minimizations. Agreement among multiple fits provides strong evidence that a true global minimum has been reached rather than an artifact of initial conditions or model assumptions.

After a suitable parameter set has been selected, the predicted cross sections should be plotted directly against the measured values, as shown in Figure 34. This comparison provides a visual assessment of the quality of the fit across the full dynamic range of the data. It is also useful to overlay predictions from the empirical parameterization EPAX3, a global fragmentation systematics model derived from a large body of experimental data [9]. EPAX is not expected to reproduce detailed isotopic structure or extreme neutron- or proton-rich yields, but it serves as a valuable baseline reference. Systematic deviations from EPAX – particularly those that are smooth and localized along isotopic chains – often reflect genuine nuclear structure effects or limitations of empirical systematics, whereas erratic or isolated discrepancies may indicate issues in the experimental analysis or the fitting procedure.

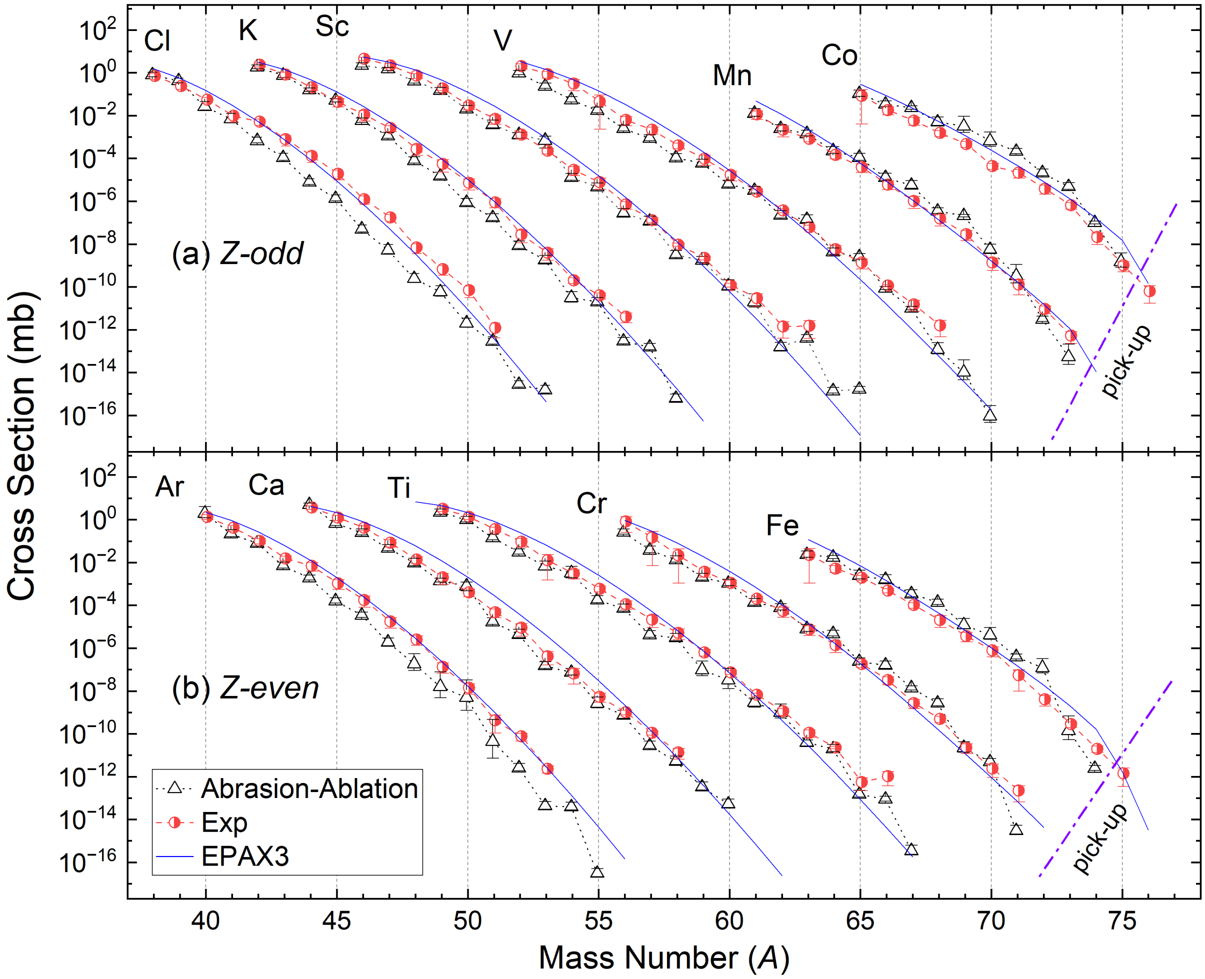

Figure 34: Abrasion-ablation and EPAX3 predicted cross sections vs experimentally measured cross sections. Pick-up reactions are labeled.

7.4 ΔBE Systematics

Cross sections for projectile fragmentation products exhibit a strong and remarkably smooth correlation with nuclear binding energy. This observation motivates the use of empirical ΔBE systematics, which relate measured production cross sections to differences in binding energy along isotopic chains. A commonly used parameterization is

$$\log(\sigma) = k_1 \ln(dBE + 1) + k_2 \ln\left(\frac{e^{k_0 S_{\min}} - 1}{k_0}\right) + b + dZ, \tag{20}$$

where

- $S_{\min}$ is the minimum nucleon separation energy for the isotopic chain, typically taken as the separation energy of the last bound isotope,
- $dBE = BE_{\max}(Z) - BE(Z, N)$ is the binding-energy difference between the most bound isotope of a given element and the isotope of interest,

- $dZ = t\,(Z_{\mathrm{beam}} - Z_{\mathrm{frag}})$ accounts for systematic shifts between isotopic chains of different atomic number,
- b is an overall normalization constant, and
- k_0, k_1, k_2, and t are empirical fit parameters.

The quantity dBE serves as a compact measure of how far a fragment lies from the most strongly bound configuration of a given element. As dBE increases toward the neutron or proton dripline, production cross sections decrease rapidly and approximately exponentially. Expressing the cross section in logarithmic form reveals a near-linear dependence on dBE, enabling systematic trends to be extracted even across many orders of magnitude in yield.

The term involving S_{min} accounts for the finite termination of isotopic chains at the dripline and encodes sensitivity to separation energies, which govern both nuclear stability and evaporation pathways during the ablation stage of the reaction. The dZ term allows for a smooth interpolation between neighboring elements by compensating for changes in projectile–fragment mass asymmetry.

Although Equation (20) is purely empirical, its success reflects the underlying role of nuclear binding in fragment production: nuclei with lower binding energy are both harder to populate during abrasion and more likely to decay during ablation. Studying deviations from the smooth ΔBE trends can therefore reveal nuclear structure effects such as shell closures, odd–even staggering, or changes in separation energy behavior near the dripline.

A full derivation and physical motivation of these systematics are beyond the scope of this manual. Interested readers are referred to the foundational work by Tarasov *et al.* [5], which established and validated this formalism across a wide range of projectile fragmentation data.

7.4.1 Performing ΔBE Fits

ΔBE systematics fits are performed in `LISE`$^{++}$ via the dialog

`1D-plot` → `Systematic Distributions` → `dBE(N, max)` → `dBE-systematics vs CS` → `dBE-systematics Settings`.

A graphical summary is presented in Ref. [28]. The overall fitting philosophy closely mirrors that used for abrasion-ablation analyses. Fits should be built incrementally: begin with the minimum number of free parameters and introduce additional parameters only as required to achieve stable convergence and a physically reasonable trend.

Experience has shown that the parameter k_0 is consistent with zero for essentially all ΔBE fits performed to date. Physically, this implies that the exponential cutoff term associated with the minimum separation energy does not introduce additional curvature beyond what is already captured by the logarithmic dependence on ΔBE. As a result, k_0 should be fixed to zero unless compelling evidence suggests otherwise.

Similarly, the parameter t, which introduces a shift between isotopic chains of different atomic number, is typically set to zero. This reflects the fact that ΔBE systematics are most robust when applied along individual isotopic chains rather than across large Z ranges.

Allowing t to float can artificially absorb deficiencies in the mass model rather than reveal them.

Within the minimization dialog, an upper cross section cutoff may be specified. This option exists to avoid generating multiple reduced data files and reflects an important physical limitation of the ΔBE approach: the systematics are most applicable in the very neutron-rich (or proton-rich) regime, where binding-energy differences dominate the production probability.

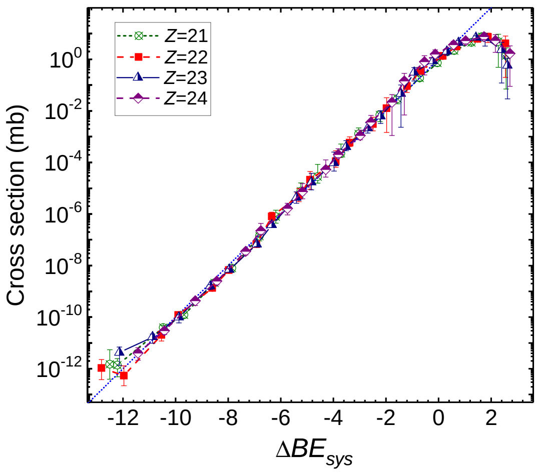

Figure 35: Measured cross sections for isotopes produced in the fragmentation of ^{82}Se plotted as a function of ΔBE using the HFB-22 mass table. The blue dotted line represents the fitted functional form $\sigma = 10^{\Delta BE_{\text{sys}}}$. From Ref. [5].

Including high-cross-section isotopes near stability can degrade the fit quality, as these nuclei are influenced by reaction mechanisms and structural effects not captured by the ΔBE parameterization. Reducing the cutoff often improves convergence and fit quality; however, care should be taken not to remove too many data points, as this can artificially constrain the slope and inflate parameter uncertainties.

The choice of nuclear mass model plays a critical role in ΔBE analyses. Because dBE enters explicitly into Equation (20), any deficiencies or biases in the mass table directly affect the extracted trends. If a given mass model fails to reproduce a smooth or physically reasonable ΔBE dependence, alternative mass tables should be tested. Figure 35 shows an example of a high-quality ΔBE fit obtained using the HFB-22 mass model.

7.4.2 Mass Table Adjustments

The ΔBE formalism relies fundamentally on nuclear binding energies, which are well known near stability but increasingly uncertain far from it. In regions where experimental mass measurements are unavailable, theoretical mass models must be used, and different models can predict substantially different binding energies for the same exotic nucleus. This sensitivity underlies why changing the mass model can significantly alter both abrasion-ablation and ΔBE fit results.

In this sense, the mass table itself acts as an implicit, high-dimensional parameter set within the ΔBE framework. The fit parameters described in the previous section primarily control the global trend of the cross section dependence, while the placement of individual data points along that trend is governed almost entirely by the calculated values of dBE, which are derived directly from the mass table.

Adjusting mass excess values for neutron-rich nuclei can therefore improve agreement between measured cross sections and ΔBE systematics. Importantly, such adjustments are not merely technical: they carry physical meaning, as changes in binding energy directly correspond to changes in nucleon separation energies and, by extension, nuclear stability.

At present, a formalized fitting procedure for mass excesses using ΔBE systematics is still under development. No dedicated Excel workbook or automated `LISE`$^{++}$ tool currently exists to perform this task in a systematic and reproducible way, and this remains an area of active research. Current approaches entail hand-tuning mass excesses on a case-by-case basis. Any mass adjustments should be treated as hypotheses requiring validation through independent observables or improved mass measurements.

A natural extension of the analysis chain is to take a mass table modified through ΔBE considerations and reapply it to abrasion-ablation calculations. In principle, a mass model constrained by cross section systematics should lead to improved agreement in AA predictions as well. This feedback loop between ΔBE and AA analyses has not yet been fully explored and represents a promising direction for future work.

7.5 Complementarity of Abrasion–Ablation and ΔBE Analyses

Abrasion-ablation (AA) and ΔBE systematics provide two complementary lenses through which newly measured production cross sections may be interpreted. While both approaches seek to describe the same experimental observables, they emphasize different physical aspects of the reaction and carry distinct sensitivities and limitations. Used together, they form a powerful, self-consistent framework for diagnosing both reaction dynamics and nuclear structure effects.

The abrasion-ablation model is fundamentally reaction-driven. It explicitly models the geometry of the projectile-target interaction, the excitation energy imparted to the pre-fragment, and the subsequent statistical decay through particle evaporation or breakup. As a result, AA calculations are sensitive to assumptions about excitation energy generation, evaporation channels, Coulomb barriers, and odd-even effects. When tuned successfully, AA provides a global description of cross sections across wide regions of the nuclear chart and offers insight into reaction mechanisms and transport dynamics.

In contrast, ΔBE systematics are intentionally minimalist. They abstract away the details of the reaction mechanism and instead focus on a strong empirical correlation between production cross sections and nuclear binding energies. In this framework, deviations from smooth ΔBE trends are interpreted primarily as manifestations of nuclear structure – such as shell closures, changes in separation energies, or deficiencies in mass models – rather than as shortcomings of reaction modeling. As such, ΔBE analyses are particularly sensitive to the underlying mass surface and are most informative in regions far from stability.

Because of these differing sensitivities, discrepancies between AA predictions and experimental data may have multiple origins. A poor AA fit may arise from an inadequate excitation energy model, an inappropriate evaporation prescription, or an incorrect mass input. The ΔBE analysis helps disentangle these possibilities: if the same data follow a clean ΔBE trend, the issue likely lies in the reaction modeling rather than the mass surface. Conversely, if both AA and ΔBE fail to reproduce the data using the same mass table, this strongly suggests deficiencies in the assumed binding energies or separation energies of the fragments.

This complementary behavior enables a productive feedback loop. ΔBE analyses can guide adjustments to mass tables by highlighting nuclei whose binding energies are inconsistent with observed cross sections. These adjusted masses can then be fed back into AA calculations, potentially improving their predictive power. Similarly, AA calculations can provide a global consistency check on whether mass adjustments inferred from ΔBE remain compatible with known reaction systematics.

In practice, the most robust interpretation of newly measured cross sections is achieved when both analyses converge on a consistent description. Agreement between AA predictions, ΔBE trends, and experimental data provides strong confidence that the essential reaction dynamics and nuclear structure inputs are being captured correctly. Persistent disagreements, on the other hand, are often the most scientifically valuable outcome, as they point directly toward regions where existing models or mass predictions require refinement.

8 Concluding Remarks

This manual has been written with the goal of guiding a first-time researcher through the complete process of rare isotope production cross section measurements, from raw experimental data to finalized, publishable results.

While the guide is designed to be as self-contained as possible, it is not truly standalone. Background knowledge is assumed in several areas related to rare isotope production, detector systems, and nuclear reaction modeling. Where appropriate, references to external sources have been provided to direct the reader to more detailed discussions.

In an effort to address the full scope of the analysis workflow, additional documentation has been appended to this manual. These appendices include practical discussions, expanded technical details, and a frequently asked questions section intended to address common points of confusion that arise during cross section analyses.

The focus of this manual has been on the how of cross section extraction, rather than the why. Nevertheless, production cross sections are valuable in two closely related contexts. First, they are essential for experimental planning in exotic regions of the nuclear chart. Production cross sections represent the ultimate limiting factor of an experiment: even with ideal transmission and high primary beam intensities, certain nuclei may only be produced on timescales of days or weeks. Quantifying production rates therefore informs the low-energy nuclear science community which experiments are currently feasible, and which may become feasible as next-generation accelerator facilities come online and reach full performance.

In this context, and particularly at FRIB, the extrapolation of cross sections using theoretical models such as abrasion–ablation and ΔBE systematics allows predictions of the facility's ultimate reach. One of FRIB's central scientific goals is the exploration of the neutron dripline, which is currently established experimentally only up to neon [29]. Rare isotope discovery and dripline determination are among the most compelling scientific objectives of the Rare Isotope Research Group, and both are enabled by reliable cross section measurements. These measurements are often obtained parasitically, alongside a wide range of other cutting-edge experiments conducted at FRIB, underscoring their broad impact across the experimental program [30, 31].

Reliable cross section measurements therefore serve not only as bookkeeping quantities, but as benchmarks for reaction models and as guideposts for future facility development. Discrepancies between measured and predicted values highlight where existing excitation energy treatments, transmission modeling, or structural inputs require refinement. In this way, cross section work feeds directly back into improvements in theoretical descriptions and simulation tools such as `LISE`$^{++}$.

The intent of this manual is to reduce procedural uncertainty while maintaining analytical rigor. As experiments continue to push further from stability, transparent and reproducible cross section measurements will remain foundational to meaningful progress.

Appendix A Installing and Booting `SpecTcl` and `SpecTk`

This appendix provides a self-contained guide for installing and launching the `SpecTcl` and `SpecTk` software packages required for cross section analysis. It assumes a Windows desktop with access to the laboratory servers hosting experimental data.

1. Required Software

Two software packages must be installed on the local machine:

1. **MobaXterm**[26]: Provides remote terminal access to Unix-based laboratory servers.
2. **Xming**[27]: Enables the display of graphical Unix applications (X11) on the local desktop.

After installation, launch Xming through the search bar. It must be running prior to starting `SpecTcl`, as `SpecTcl` relies on X11 forwarding for all graphical output. The presence of the Xming icon in the system tray confirms it is active.

2. Configuring Remote Access

Remote connections are established using PuTTY. It is recommended to create two saved sessions:

1. Personal account on the `fishtank` server:
   `<yourFRIBUserName>@fishtank`
2. Laboratory account `arisdaq` on `fishtank`:
   `arisdaq@fishtank`

For both sessions, configure:

- Connection type: SSH
- Port: 22
- X11 forwarding: enabled (under SSH → X11)

Assign descriptive names to each session and click `Save`.

---

[26] The program can be downloaded from: `https://mobaxterm.mobatek.net/`

[27] This program is available from the “Software Center” on your desktop.

3. Logging In

Open MobaXterm. The sessions defined in PuTTY appear under `User sessions`. Double-click the desired session to connect. After the laboratory banner, log in with the appropriate password: personal account passwords match your email password; the `arisdaq` password is distributed separately.

Once logged in to the arisdaq account, the default directory is `/user/arisdaq`. Navigate to the `SpecTcl` directory:

`/user/arisdaq/PID/User`.

4. Preparing a Working Directory

Create a dedicated working directory for the analysis. At the start of each analysis:

1. Copy the most recent `SpecTcl` build from `/PID/Develop` into your working directory.
2. From the `source` subdirectory, execute:

```
make clean

make
```

Maintaining a single `SpecTcl` build per analysis prevents version drift, greatly reduces potential errors, and ensures reproducibility. After creating a new work directory, it is important to update the path to the calibration files in the `loadCalibration.tcl` file. If changing values in `pid_values.csv` appears to do nothing, this is likely the problem.

5. Starting the Buster Shell

Before launching `SpecTcl`, the Buster shell must be active. A script to start it is located inside each `SpecTcl` directory. Execute the script using:

`busterdaq_LISE`.

6. Launching `SpecTcl`

From the root directory of the compiled `SpecTcl` build:

1. Open two additional terminals with the command `xterm &`.
2. Launch `SpecTcl` from one of these terminals.

Upon successful startup, the following windows appear:

- `info`: displays detector efficiency
- `treegui`: used for defining spectra and managing gates
- Two `SpecTcl` windows: one command-line interface, one file control GUI
- `Xamine`: not used in this workflow

If `SpecTcl` fails to load, consult the terminal output. Common causes include Xming not running, the Buster shell not active, or issues with the `steelhead` server.

7. Loading Definition Files

In the `treegui` window, load a definition file using the control in the upper-right corner (Fig. 36, **A**). Definition files are typically located in:

`/<yourVersionName>/def/`.

Successful loading is indicated by text appearing in the central display area of the window.

8. Launching SpecTk

In an `xterm` terminal, navigate to:

`/user/arisdaq/SpecTk`

and execute the program. Once `SpecTk` opens:

1. Select `Connect to` from the `SpecTk` drop-down menu.
2. Enter `localhost` as the server name.
3. Enter the four-digit port number displayed in the `SpecTcl GUI` under “SpecTcl server is up and listening on port xxxx”.

Upon successful connection:

- The `clients connected` counter in `SpecTcl` increments.
- The top of the `SpecTk` window reads: `Status: Connected to localhost on port xxxx` (Fig. 38, **A**).

`SpecTk` files may now be opened via `File` → `Open`, or new files may be created and saved.

9. Notes and Best Practices

- Always ensure Xming is running before launching `SpecTcl`.
- Use a dedicated working directory for each analysis to ensure reproducibility.
- Keep a single `SpecTcl` build per analysis.
- If errors occur, check Xming, the Buster shell, and server connectivity.

Appendix B Analysis Program Basics

This appendix summarizes the essential functionality of `SpecTcl` and `SpecTk` required for cross section analysis. Advanced features are documented in the official references and are not covered here[28].

B.1 `SpecTcl`

Most user interactions with `SpecTcl` occur through the `treegui` or the main `SpecTcl GUI`.

Defining Spectra

The `treegui` is used to define spectra and manage existing definitions. To define a spectrum:

1. Select the spectrum type in the upper-left corner (Fig. 36, **B**). The most common types are one-dimensional and two-dimensional spectra.
2. Choose the parameter(s) from the central list (Fig. 36, **C**). For two-dimensional spectra, parameters are ordered as (x, y).
3. Set axis limits and the number of bins. Excessively fine binning, especially for two-dimensional spectra, may exceed the shared-memory limit and should be avoided.
4. Click `Create/Replace` to define the spectrum.

Existing spectra can be edited by double-clicking their names in the list, modifying fields, and clicking `Create/Replace`. Controls adjacent to the list allow spectra to be deleted, duplicated, or cleared.

Managing Gates

Gates are created and managed through the `treegui Gate` tab (Fig. 37):

- Display existing gates from a loaded definition file by clicking `Update gate list` (Fig. 37, **A**).
- Gates may be defined manually by entering coordinates or interactively via `SpecTk`. Manual definition is recommended only for simple cases.

---

[28] See `https://lise.frib.msu.edu/work/SpecTclSpecTk_Tutorial_Haak.pdf` for a detailed description of the software architecture and analysis pipeline.

- Gates can be edited directly in the `treegui`, though this becomes cumbersome for complex gates.

Compound gates (AND, OR, NOT) can be created as follows:

1. Assign a name beneath the `Create/Replace` button.
2. Select the gate type from the drop-down menu (Fig. 37, **B**).
3. Enter the names of gates to combine or select them from the `Gate Select` menu.

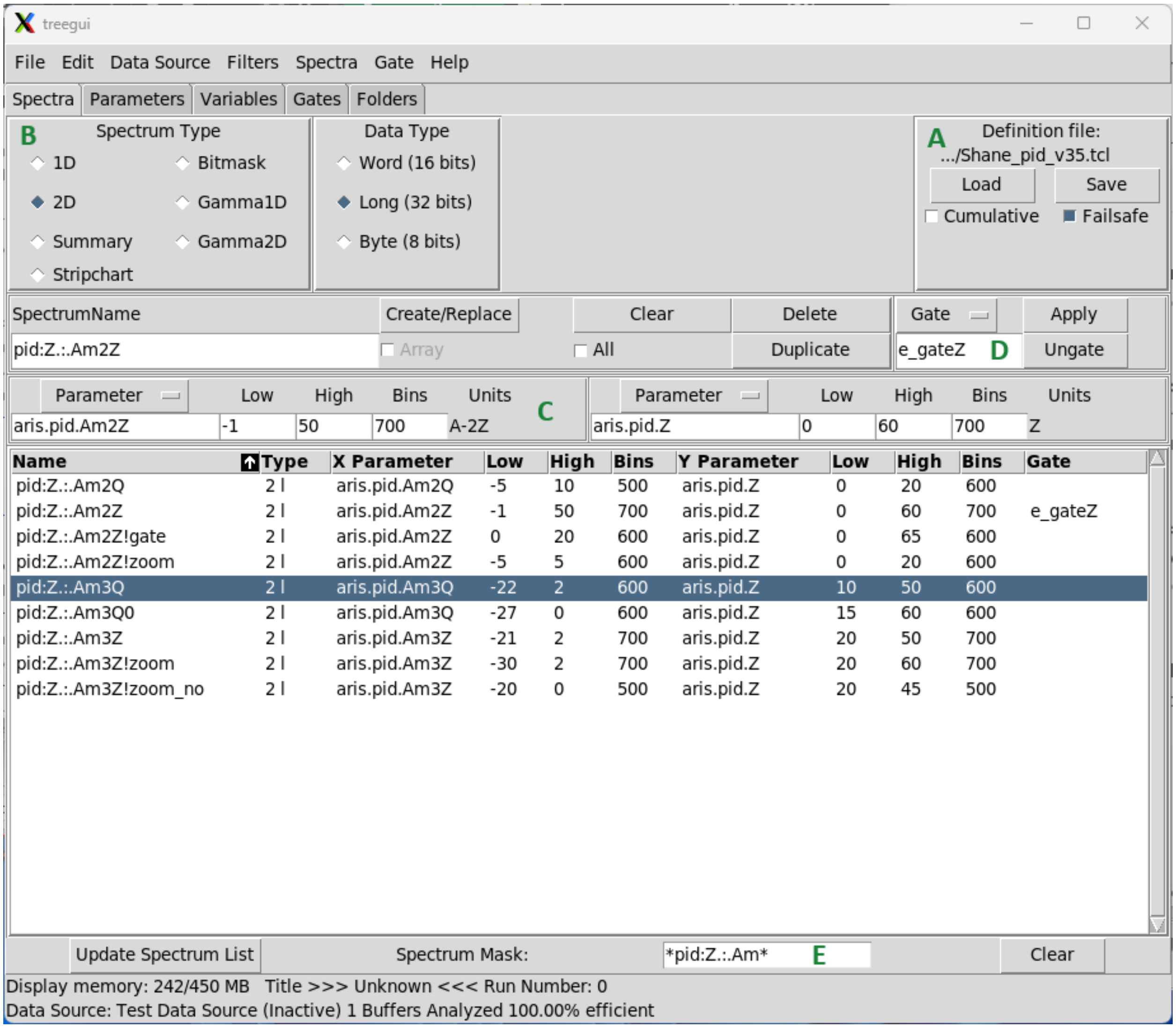

Spectrum Type: ○ 1D ○ Bitmask ● 2D ○ Gamma1D ○ Summary ○ Gamma2D ○ Stripchart

Data Type: ○ Word (16 bits) ● Long (32 bits) ○ Byte (8 bits)

Definition file: .../Shane_pid_v35.tcl

☐ Cumulative ☒ Failsafe

SpectrumName: pid:Z.:.Am2Z

☐ Array ☐ All

Gate: e_gateZ

Parameter	Low	High	Bins	Units
aris.pid.Am2Z	-1	50	700	A-2Z
aris.pid.Z	0	60	700	Z

Name	Type	X Parameter	Low	High	Bins	Y Parameter	Low	High	Bins	Gate
pid:Z.:.Am2Q	2 l	aris.pid.Am2Q	-5	10	500	aris.pid.Z	0	20	600	
pid:Z.:.Am2Z	2 l	aris.pid.Am2Z	-1	50	700	aris.pid.Z	0	60	700	e_gateZ
pid:Z.:.Am2Z!gate	2 l	aris.pid.Am2Z	0	20	600	aris.pid.Z	0	65	600	
pid:Z.:.Am2Z!zoom	2 l	aris.pid.Am2Z	-5	5	600	aris.pid.Z	0	20	600	
pid:Z.:.Am3Q	2 l	aris.pid.Am3Q	-22	2	600	aris.pid.Z	10	50	600	
pid:Z.:.Am3Q0	2 l	aris.pid.Am3Q	-27	0	600	aris.pid.Z	15	60	600	
pid:Z.:.Am3Z	2 l	aris.pid.Am3Z	-21	2	700	aris.pid.Z	20	50	700	
pid:Z.:.Am3Z!zoom	2 l	aris.pid.Am3Z	-30	2	700	aris.pid.Z	20	60	700	
pid:Z.:.Am3Z!zoom_no	2 l	aris.pid.Am3Z	-20	0	500	aris.pid.Z	20	45	500	

Spectrum Mask: *pid:Z.:.Am*

Display memory: 242/450 MB Title >>> Unknown <<< Run Number: 0
Data Source: Test Data Source (Inactive) 1 Buffers Analyzed 100.00% efficient

Figure 36: The `SpecTcl` `treegui` Spectrum tab interface.

To apply a gate to a spectra:

- Select one or more spectra.

- Select the desired gate and click `Apply`.
- Click `Ungate` to remove all gates from the selected spectra.

A search field at the bottom of the window (Fig. 36, **E**) allows locating specific spectra or gates using queries enclosed in asterisks, e.g., `*SpectrumName*`.

File Operations

Data files are read using the `SpecTcl GUI`. Key functions include:

- `Clear Spectra`: removes all accumulated data from memory.
- `Pause Analysis`: temporarily halt file processing.
- `Read ArisVariable`: reload calibration files.
- `Attach Online`: connects to live data acquisition.
- `Attach to previously used file`: restart the most recent run after clearing spectra and reloading calibrations.
- `Attach to next/prior runs`: increment or decrement the run number after reloading calibration files.
- `Attach list of files`: reads a cluster file containing a user-defined list of runs processed sequentially.
- `Detach`: stops file processing.

B.1.1 `SpecTcl` Filtering Output

One of the core functionalities of `SpecTcl` is the ability to filter event data through gates, as described in the previous section. Within the `SpecTcl` framework, gated event data can be written out to a new file, allowing subsequent stages of the analysis to operate on a reduced and cleaner data set. For very large data sets, this reduction can result in substantial time savings during downstream processing.

By default, `SpecTcl` writes filtered data in a native binary format intended for re-ingestion by `SpecTcl` itself[29]. In the ARIS `SpecTcl` build, an extended capability has been implemented that allows filtered output to be written directly to a comma-separated values (CSV) file[30].

In this CSV format, each column corresponds to a selected spectrum (or parameter), and each row represents a single correlated event. If a particular spectrum is not defined for

---

[29] This functionality has not yet been successfully integrated into any working version of the ARIS `SpecTcl` analysis chain.

[30] See `https://lise.frib.msu.edu/work/SpecTcl/SpecTcl_Filter_Output%20v3.pdf` for more information.

a given event, the corresponding cell is left empty. This preserves event-by-event correlations while allowing the data to be read by external analysis tools.

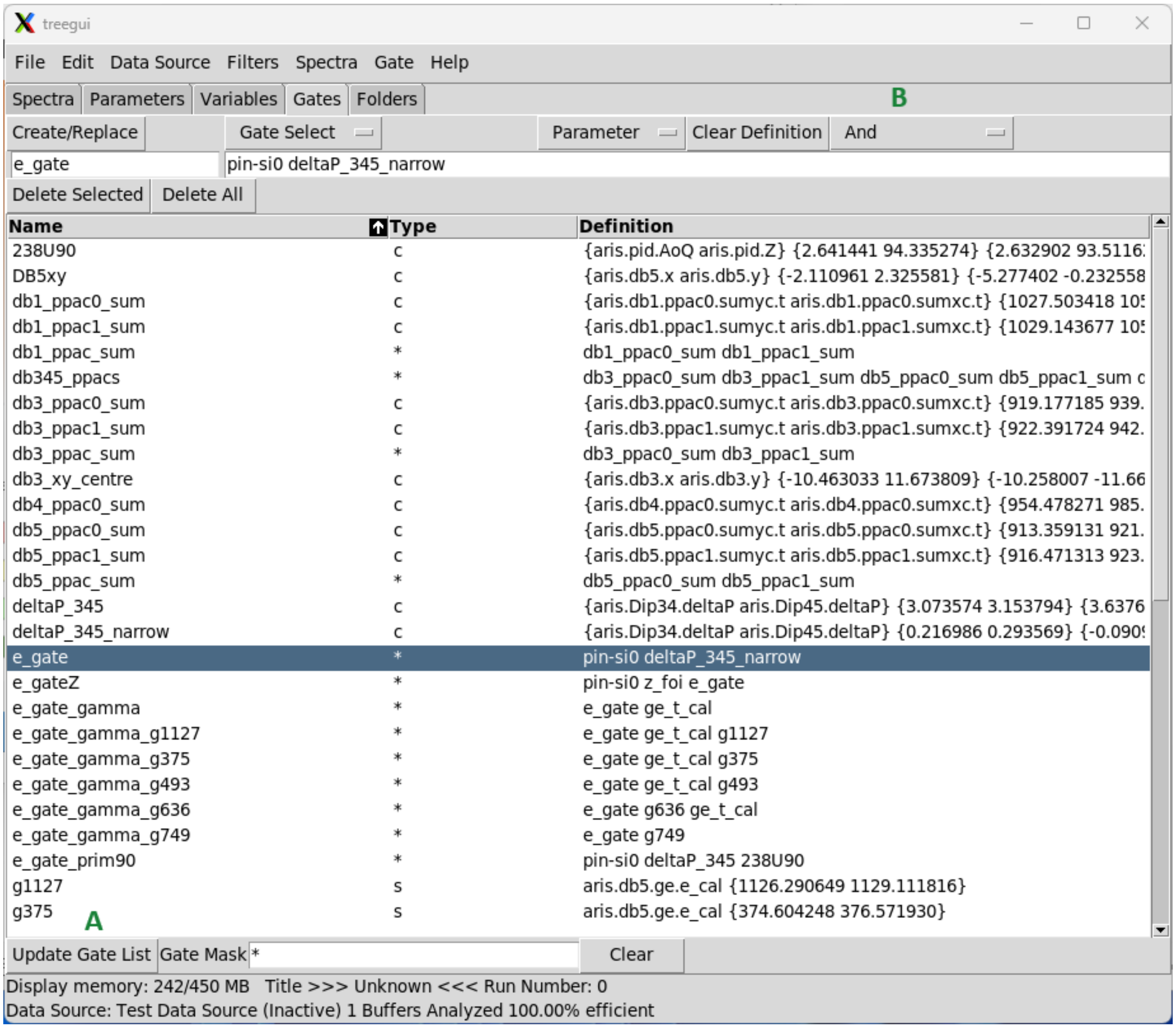

e_gate

pin-si0 deltaP_345_narrow

Name	Type	Definition
238U90	c	{aris.pid.AoQ aris.pid.Z} {2.641441 94.335274} {2.632902 93.5116
DB5xy	c	{aris.db5.x aris.db5.y} {-2.110961 2.325581} {-5.277402 -0.232558
db1_ppac0_sum	c	{aris.db1.ppac0.sumyc.t aris.db1.ppac0.sumxc.t} {1027.503418 10
db1_ppac1_sum	c	{aris.db1.ppac1.sumyc.t aris.db1.ppac1.sumxc.t} {1029.143677 10
db1_ppac_sum	*	db1_ppac0_sum db1_ppac1_sum
db345_ppacs	*	db3_ppac0_sum db3_ppac1_sum db5_ppac0_sum db5_ppac1_sum
db3_ppac0_sum	c	{aris.db3.ppac0.sumyc.t aris.db3.ppac0.sumxc.t} {919.177185 939.
db3_ppac1_sum	c	{aris.db3.ppac1.sumyc.t aris.db3.ppac1.sumxc.t} {922.391724 942.
db3_ppac_sum	*	db3_ppac0_sum db3_ppac1_sum
db3_xy_centre	c	{aris.db3.x aris.db3.y} {-10.463033 11.673809} {-10.258007 -11.66
db4_ppac0_sum	c	{aris.db4.ppac0.sumyc.t aris.db4.ppac0.sumxc.t} {954.478271 985.
db5_ppac0_sum	c	{aris.db5.ppac0.sumyc.t aris.db5.ppac0.sumxc.t} {913.359131 921.
db5_ppac1_sum	c	{aris.db5.ppac1.sumyc.t aris.db5.ppac1.sumxc.t} {916.471313 923.
db5_ppac_sum	*	db5_ppac0_sum db5_ppac1_sum
deltaP_345	c	{aris.Dip34.deltaP aris.Dip45.deltaP} {3.073574 3.153794} {3.6376
deltaP_345_narrow	c	{aris.Dip34.deltaP aris.Dip45.deltaP} {0.216986 0.293569} {-0.090
e_gate	*	pin-si0 deltaP_345_narrow
e_gateZ	*	pin-si0 z_foi e_gate
e_gate_gamma	*	e_gate ge_t_cal
e_gate_gamma_g1127	*	e_gate ge_t_cal g1127
e_gate_gamma_g375	*	e_gate ge_t_cal g375
e_gate_gamma_g493	*	e_gate ge_t_cal g493
e_gate_gamma_g636	*	e_gate g636 ge_t_cal
e_gate_gamma_g749	*	e_gate g749
e_gate_prim90	*	pin-si0 deltaP_345 238U90
g1127	s	aris.db5.ge.e_cal {1126.290649 1129.111816}
g375	s	aris.db5.ge.e_cal {374.604248 376.571930}

Gate Mask *

Display memory: 242/450 MB Title >>> Unknown <<< Run Number: 0
Data Source: Test Data Source (Inactive) 1 Buffers Analyzed 100.00% efficient

Figure 37: The `SpecTcl` `treegui` Gates tab interface.

The primary purpose of filtering is to extract clean subsets of data that satisfy specific PID or quality gates. However, it is also possible to output essentially all calibrated event data if desired. The analysis tool `Ray Reader`[31] was originally developed for use with `LISE`$^{++}$ Monte Carlo data, but its functionality has since been extended to support `SpecTcl` CSV output. Once all calibrations have been finalized, `Ray Reader` can therefore serve as a lightweight substitute for `SpecTcl` for many downstream analysis tasks.

From the `SpecTcl` command line, the following sequence of commands defines and controls a filter:

- `filter -new <filterName> <gateName> {spectra}`

---

[31] `https://lise.frib.msu.edu/doc/ray-reader-documentation/`

Defines a new filter, specifying the gate to apply and the list of spectra to be written to the output file.

- `filter -file <fileName.csv> <filterName>`

  Specifies the output file for the filter. By default, files are written to the `SpecTcl` root directory, though an explicit path may be provided.

- `filter -format <filterName> csv`

  Changes the output format from the default XDR format to CSV.

- `filter -enable` (`-disable`) `<filterName>`

  Enables or disables the filter. Note that `SpecTcl` will overwrite existing files with the same name.

This filtering capability is required for the trajectory reconstruction procedure discussed in subsection C.3, as well as for the empirical transfer matrix regression described in subsubsection C.3.2.

B.2 SpecTk

`SpecTk` is a visualization extension for `SpecTcl`, providing functionality not available in Xamine.

Page and Spectrum Management

Configuration controls are accessed via `Open Drawer` in the lower-right corner. Pages are managed under the `Page` tab, and spectra are assigned to page cells under the `Spectrum` tab (Fig. 38).

Defining ROIs and Gates

The `ROI` tab is used to define regions of interest (local to `SpecTk`) and gates, which are shared with `SpecTcl`. Toggle between ROI and gate creation using the buttons at the top of the window (Fig. 38, **B**).

To create a gate:

1. Select the gate type: `Slice` for one-dimensional plots, `Contour` for two-dimensional plots.
2. Define the region interactively; for contour gates, double-click to complete the shape.
3. Assign a name and click `Validate` to create the gate, or `Cancel` to discard.

Existing gates can be modified by:

- Selecting the contour-edit tool on the left side of the `SpecTk` window (Fig. 38, **C**) and dragging gate vertices.
- Creating a new gate with the same name. In both cases, the updated definition is synchronized between `SpecTk` and `SpecTcl`.

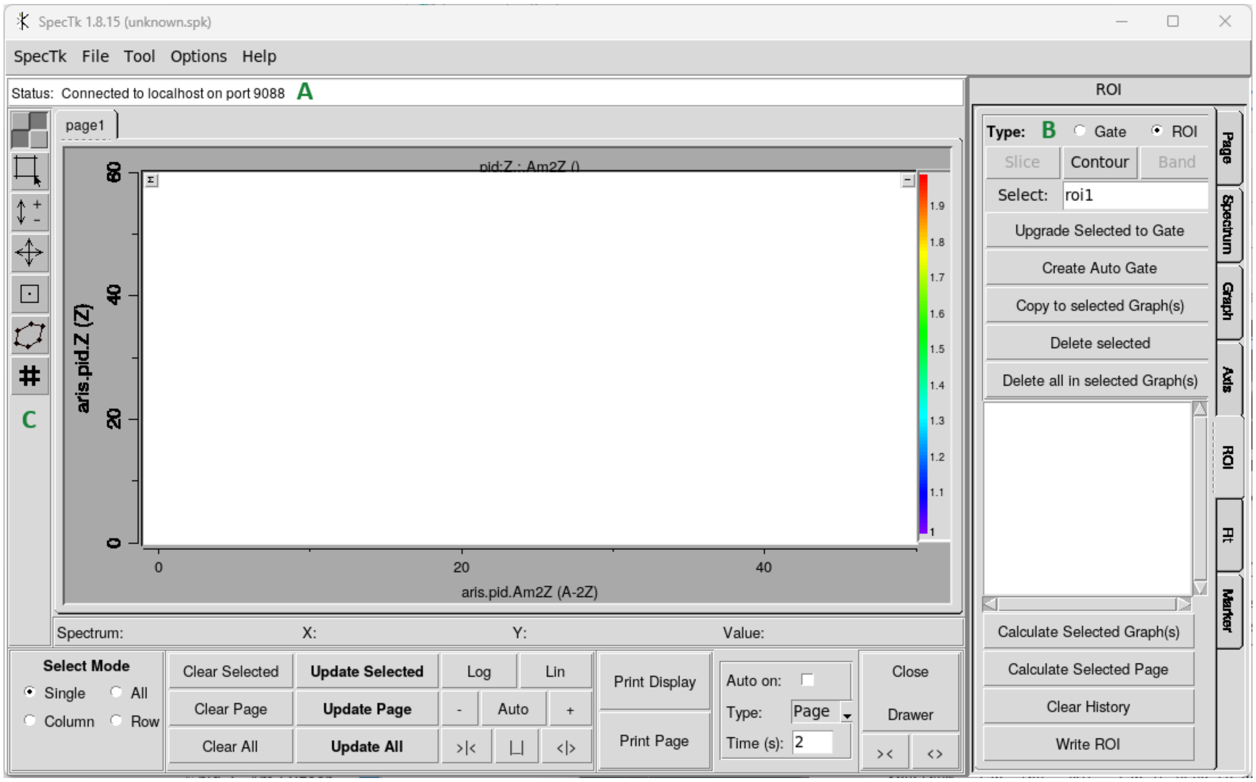

Status: Connected to localhost on port 9088

Type: ○ Gate ● ROI

Select: roi1

● Single ○ All
○ Column ○ Row

Auto on: ☐
Type: Page
Time (s): 2

Figure 38: The `SpecTk` GUI.

B.3 Excel

Excel workbooks are used extensively throughout the analysis process. This subsection summarizes intermediate Excel functionality and good spreadsheet practices that may not be familiar to a first-time analyst.

B.3.1 Excel Functions

- `VLOOKUP` (and `XLOOKUP`)

  The `VLOOKUP` function retrieves a value from a table based on a reference value. It is particularly useful when working with large datasets of measured cross sections or isotope properties, where values must be matched automatically across sheets.

  The syntax is:

  ```
  =VLOOKUP(<refVal>, <table>, <colNum>, <exactMatch>)
  ```

  where:

  - `refVal` is the value to search for (e.g., an isotope index such as $1000Z + N$),
  - `table` is the cell range to search,
  - `colNum` is the column number within the table to return (counting from 1),

  - `exactMatch` is `FALSE` (or 0) for exact match and `TRUE` (or 1) for approximate match. Exact match is strongly recommended for analysis work.

  Important: `VLOOKUP` searches only the leftmost column of the specified table and returns values from columns to the right. For newer versions of Excel (e.g., Excel 365), `XLOOKUP` is generally preferred, as it allows greater flexibility and avoids many common indexing errors.

- `INDIRECT`

  The `INDIRECT` function converts text into a cell reference. Its syntax is:

  ```
  =INDIRECT(ref_text)
  ```

  where `ref_text` is a string specifying the desired cell or range.

  This function is useful when referencing dynamically changing cells, such as looping over runs or automatically selecting values from another sheet based on an index. It allows formulas to be constructed programmatically rather than hard-coded.

  For example, in Figure 39, the logical function determines whether a beam power measurement falls within the start and stop times of a given run. The formula in cell E8 is:

  ```
  =IF(AND($A8=INDIRECT("’Exp Times’!B"&F$1),
  INDIRECT("’Exp Times’!C"&F$1)<=rawBeamCurrent!$B8,
  rawBeamCurrent!$B8<=INDIRECT("’Exp Times’!D"&F$1)),
  rawBeamCurrent!$C8,0)
  ```

  This formula checks whether the date and timestamp in the current row fall within the run boundaries specified on the `’Exp Times’` sheet. If so, it returns the beam power measurement; otherwise, it returns 0.

  The use of `INDIRECT` allows the row reference to be controlled by the value in cell `F$1`, enabling consistent repetition across multiple runs.

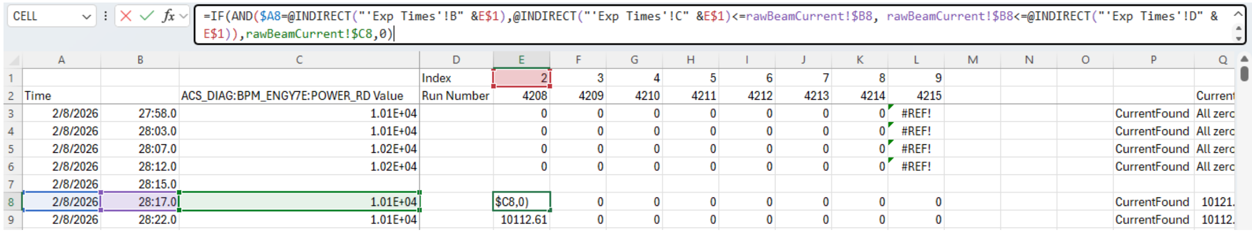

```
=IF(AND($A8=@INDIRECT("'Exp Times'!B" &E$1),@INDIRECT("'Exp Times'!C" &E$1)<=rawBeamCurrent!$B8, rawBeamCurrent!$B8<=@INDIRECT("'Exp Times'!D" &
E$1)),rawBeamCurrent!$C8,0)
```

	A	B	C	D	E	F	G	H	I	J	K	L	M	N	O	P	Q
1				Index	2	3	4	5	6	7	8	9					
2	Time		ACS_DIAG:BPM_ENGY7E:POWER_RD Value	Run Number	4208	4209	4210	4211	4212	4213	4214	4215					Curren
3	2/8/2026	27:58.0	1.01E+04		0	0	0	0	0	0	0	#REF!				CurrentFound	All zer
4	2/8/2026	28:03.0	1.01E+04		0	0	0	0	0	0	0	#REF!				CurrentFound	All zer
5	2/8/2026	28:07.0	1.02E+04		0	0	0	0	0	0	0	#REF!				CurrentFound	All zer
6	2/8/2026	28:12.0	1.02E+04		0	0	0	0	0	0	0	#REF!				CurrentFound	All zer
7	2/8/2026	28:15.0															
8	2/8/2026	28:17.0	1.01E+04		$C8,0)	0	0	0	0	0	0	0				CurrentFound	10121.
9	2/8/2026	28:22.0	1.01E+04		10112.61	0	0	0	0	0	0	0				CurrentFound	10112.

Figure 39: Example of the Excel `INDIRECT` function.

- `Pivot Tables`

  `Pivot Tables` and `Pivot Charts` are powerful tools for data organization and visualization. They allow rapid grouping, filtering, aggregation, and summarization of large datasets without modifying the original data.

  For example, one can:

  - Sum counts by isotope,
  - Group runs by date,
  - Average beam currents by run,
  - Filter specific reaction types.

  Fluency with Pivot Tables significantly improves efficiency and reduces manual calculation errors. Detailed documentation is available in the Excel support materials[32]. It is not hyperbole to say that "mastery of Excel" is tied almost entirely to this tool.

B.3.2 Excel Housekeeping

When working with large and complex worksheets, consistent formatting and organization greatly improve readability and reduce errors.

- **Freeze Panes:**

  Freezing rows and columns ensures that headers and indexing information remain visible while scrolling. This reduces referencing errors and improves readability in large datasets.

  Access via: Ribbon (top of the window) → View → Freeze Panes.

- **Named Reference Cells:**

  Cells that are repeatedly used in formulas (e.g., target thickness, normalization factors, fit parameters) should be assigned names. Named ranges act like variables and improve equation readability.

  For example, instead of referencing `B17`, a formula may reference `TargetThickness`. This makes equations self-documenting and easier to debug.

  Names are defined via: Ribbon → Formulas → Define Name.

- **Numerical Formatting:**

  Limit displayed decimal places to a reasonable number (typically 2–4, depending on context). Excess digits reduce readability and imply false precision. Scientific notation is often appropriate for cross sections.

  Ensure formatting reflects significant figures consistent with uncertainties.

  Centering or justifying the values also creates uniformity in the spreadsheet. The position of the numbers is dictated by the content of the nearby text. An example of a number-heavy spreadsheet is shown in Figure 17.

- **Highlighting:**

  Use color sparingly and intentionally. Highlight:

  - Final results,

---

[32] https://support.microsoft.com/en-us/office/create-a-pivottable-to-analyze-worksheet-data-a9a84538-bfe9-40a9-a8e9-f99134456576

  - Input parameters,
  - Cells requiring user modification,
  - Warning or diagnostic outputs.

  Avoid decorative or excessive coloring, which reduces clarity.

- **Documentation:**

  Each sheet should clearly state:

  - Its purpose,
  - Required inputs,
  - Key outputs,
  - Assumptions or model dependencies.

  Spreadsheets used for analysis are scientific documents and should be treated accordingly.

- **Version Control:**

  Maintain archived copies of major workbook revisions. Document changes between versions. Never overwrite original raw data.

Appendix C Ion Optics and Trajectory Reconstruction Primer

The purpose of this appendix is to introduce concepts related to ion optics and trajectory reconstruction in the context of fragment separators and secondary beam purification. Throughout this appendix, and implicitly throughout the manual, we adopt the `TRANSPORT` notation of ion optical matrix elements [32].

As with other content in this manual, this discussion of ion optics is not intended to be complete. Rather, it aims to provide the reader with a practical working knowledge of optics as it pertains to cross section measurements, particle identification, and transmission corrections. Many textbooks and monographs have been written on charged-particle optics; interested readers are directed to these for a more formal and complete treatment [33, 34].

C.1 The Transfer Matrix and Other Optical Definitions

An optical system is a series of electromagnetic elements that are used to transport a beam of charged particles from one place to another. In particular, a fragment separator is an optical system designed to purify the secondary beam for delivery to an experiment. The Advanced Rare Isotope Separator (ARIS) consists of various magnetic elements: dipoles, quadrupoles, sextupoles, and octupoles. Additionally, materials such as wedges, position and energy detectors, and slits exist in the beamline to aid in the purification process.

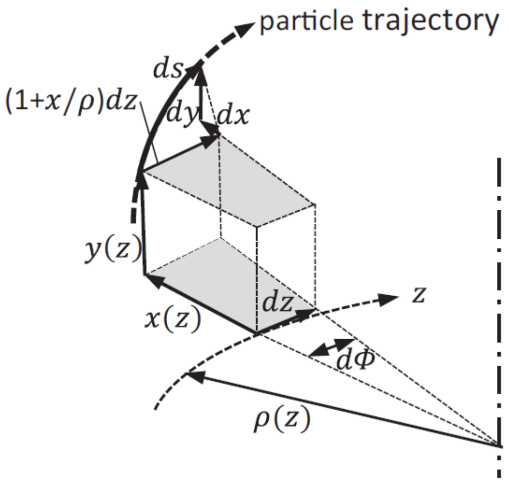

Figure 40: The curvilinear coordinate system used in the definition of the ion optical vector $\vec{V}$. The optical axis is $\vec{s}$.

A beam particle moving through an optical system can be represented as a six-dimensional phase-space vector, which contains its transverse position (x, y), its angle relative to the reference trajectory in both transverse directions (θ, ϕ), a relative path-length difference between an arbitrary particle and the reference particle (l), and the relative momentum deviation of the particle (δ):

$$\vec{V} = \begin{pmatrix} x \\ \theta \\ y \\ \phi \\ l \\ \delta \end{pmatrix} \tag{21}$$

Here, $\delta = \Delta p/p_0$ is defined with respect to the reference particle momentum p_0. The path-length coordinate l represents the difference in distance traveled by an arbitrary particle compared to the reference trajectory and plays an important role in time-of-flight measurements and longitudinal beam dynamics.

The reference particle is defined as the ideal particle traversing the system: it follows the designed optical axis exactly and has the reference momentum and charge-state. All other particles are described relative to this trajectory. The trajectory definitions are shown in Figure 40.

Just as every particle has a vector associated with it, every element along the beamline has an associated transfer matrix. The transfer matrix calculates how the beamline element affects the particles as they traverse the system. The general matrix is defined as:

$$M = \begin{pmatrix} (x|x) & (x|\theta) & 0 & 0 & 0 & (x|\delta) \\ (\theta|x) & (\theta|\theta) & 0 & 0 & 0 & (\theta|\delta) \\ 0 & 0 & (y|y) & (y|\phi) & 0 & 0 \\ 0 & 0 & (\phi|y) & (\phi|\phi) & 0 & 0 \\ (l|x) & (l|\theta) & 0 & 0 & (l|l) & (l|\delta) \\ 0 & 0 & 0 & 0 & 0 & (\delta|\delta) \end{pmatrix} \tag{22}$$

where elements shown as identically zero arise from mid-plane symmetry, the assumed decoupling of horizontal and vertical motion, and the choice of coordinate system. ARIS is designed to be well described by this first-order, uncoupled approximation. Additionally, this matrix implicitly assumes that the x-plane is the dispersive plane. This is assumed in all further discussion.

Definitions of each matrix element are displayed in Figure 41, along with the definition of beam transport in the language of matrices. Elements along the diagonal represent the magnification in each coordinate. Highlighted cross terms represent the focusing of the beam, and the sixth column represents the dispersion of each coordinate.

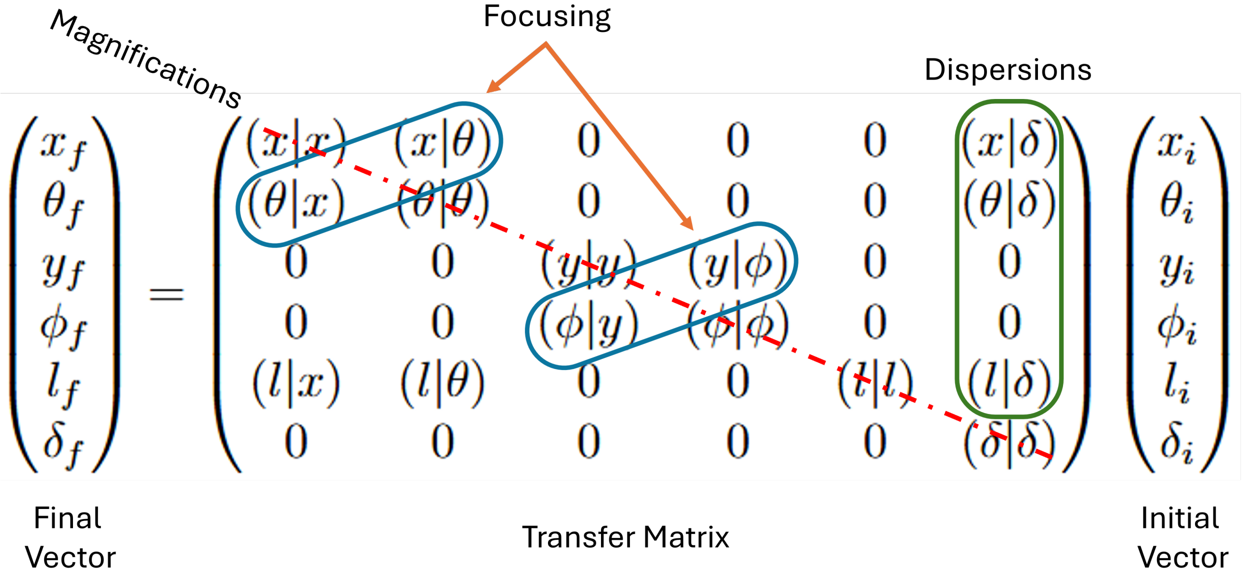

$$\begin{pmatrix} x_f \\ \theta_f \\ y_f \\ \phi_f \\ l_f \\ \delta_f \end{pmatrix} = \begin{pmatrix} (x|x) & (x|\theta) & 0 & 0 & 0 & (x|\delta) \\ (\theta|x) & (\theta|\theta) & 0 & 0 & 0 & (\theta|\delta) \\ 0 & 0 & (y|y) & (y|\phi) & 0 & 0 \\ 0 & 0 & (\phi|y) & (\phi|\phi) & 0 & 0 \\ (l|x) & (l|\theta) & 0 & 0 & (l|l) & (l|\delta) \\ 0 & 0 & 0 & 0 & 0 & (\delta|\delta) \end{pmatrix} \begin{pmatrix} x_i \\ \theta_i \\ y_i \\ \phi_i \\ l_i \\ \delta_i \end{pmatrix}$$

Figure 41: Definition of principle elements in the first-order transfer matrix, along with matrix multiplication definition.

The explicit derivation of the transfer matrix for every element in the beamline is far beyond the scope of this manual. Detailed derivations are presented in Ref. [32]. An important distinction should be made here: the matrices above represent the *first-order* transport of a beam. These optics adequately describe drift regions, dipoles, and quadrupoles under small-angle and small-momentum-spread assumptions.

The global transfer matrix is defined as the matrix multiplication of all component parts of the transport system. It is important to note that the matrix multiplication is performed from the end of the system to the beginning:

$$M_{tot} = M_f \cdot M_{f-1} \ldots M_2 \cdot M_1, \tag{23}$$

where M_i represents the transfer matrix of the optical element.

Higher-order effects – arising from intrinsic field nonlinearities, finite magnet apertures, or large momentum acceptance – are described by higher-rank tensors (second-order transport corresponds to rank-3 tensors, third-order to rank-4, and so on). These higher-order terms give rise to optical aberrations.

An aside on the types of magnets used for beam transport:

- **Dipoles**: magnets used to bend the beam trajectory. Dipoles are the primary source of dispersion in a beamline.
- **Quadrupoles**: first-order focusing elements used to control beam envelopes and imaging conditions. Quadrupoles introduce chromatic aberrations due to momentum-dependent focusing.

- **Sextupoles**: second-order correction magnets primarily used to correct chromatic aberrations introduced by quadrupoles and dipoles[33]. Sextupoles introduce third-order geometric aberrations.

- **Octupoles**: third-order correction magnets used to compensate aberrations introduced by sextupoles. These introduce fourth-order aberrations.

These magnets are commonly used in beam transport to create the desired optical conditions. They are analogous to lenses in light optics. The focusing strength of a quadrupole magnet is related to the length of the magnet along the beam axis, the size of the aperture the beam passes through, and the amount of current flowing through its wires. For a set geometry, the only variable parameter is the current. Tuning the beam refers to the action of adjusting the focusing strengths (electric current) of the magnet to create the desired transport conditions. Mathematically, this is equivalent to changing the quadrupole matrix to achieve certain global transfer matrix elements.

Aberrations manifest themselves in various ways. No matter the manifestation, they are undesired and significant work has been done to correct them. In the simplest form, these aberrations impact the shape of the beam profile. This can enlarge the beamspot, creating issues for transport downstream. Aberrations can also conspire to *increase* the transmission of unwanted particles. This can be a large source of unwanted background for experiments and must be treated explicitly during the `LISE`$^{++}$ transmission analysis, as seen in section 5.

In the context of cross section measurements, aberrations are particularly important because they can distort the relationship between measured detector coordinates and the true particle rigidity or trajectory. If left uncorrected, these effects can bias transmission estimates and particle identification, especially for large-acceptance settings.

Magnets beyond the octupole can be implemented in a beamline if control over the high-order aberrations is desired (e.g., decapole (10 poletips) or dodecapole (12 poletips)), but these magnets are not implemented in ARIS.

An alternative approach to correcting high-order aberrations through the introduction of hardware (magnets) is to correct the optics through trajectory reconstruction. Trajectory reconstruction seeks to correct, on an event-by-event basis, for the effects of finite acceptance and optical aberrations using measured detector information and known optical properties of the separator. This approach can effectively extend the usable acceptance of the system without introducing additional hardware. This is discussed in the subsection C.3.

Before discussing the details of trajectory reconstruction, further groundwork must first be laid on ion optical terminology.

- **Phase Space**: the transverse coordinate–angle space (e.g., x-θ) describing the beam envelope. Beam transmission depends on how this distribution fits within the acceptance of downstream elements.

- **Emittance**: a measure of the phase-space area occupied by the beam in a given plane. Emittance is conserved under linear, conservative (symplectic) transport.

---

[33] Dipoles with shaped pole faces can deliberately introduce second-order terms.

- **Acceptance**: the region of phase space that an optical system can transport without loss.
- **Transmission**: the fraction of particles produced at the target that fall within the acceptance of the system and reach a downstream location.
- **Dispersion**: the dependence of transverse position or angle on momentum deviation. In a dispersive plane, particles of different rigidity separate spatially.
- **Momentum Resolving Power**: the ability of an optical system to distinguish particles of different momenta, often characterized by the ratio of dispersion to beam size at a focal plane.
- **Magnification**: the scaling of beam size between two locations, given by first-order matrix elements such as $(x|x)$ or $(y|y)$. Large magnification increases spatial separation but also amplifies detector resolution effects.
- **Chromatic Aberrations**: aberrations arising from momentum dependence of focusing elements.
- **Geometric Aberrations**: aberrations arising from finite beam size or angular spread, independent of momentum.
- **Focus**: the beam is focused in a given plane when the final position is independent of the initial angle in that plane $[(x|\theta), (y|\phi) = 0]$.
- **Achromatic**: the beam position and angle are independent of momentum deviation $[(x|\delta) = (\theta|\delta) = 0]$.
- **Aberration**: a higher-order optical term that distorts the image at a focal plane (e.g., chromatic aberrations such as $(x|\theta\delta) \neq 0$).
- **Beam Envelope**: the maximum transverse extent of the beam as it propagates through the system.
- **Parallel Beam**: a beam for which particle angles are small and narrowly distributed about zero (small angular divergence), often realized at a waist.
- **Beam Waist**: a location where the beam envelope reaches a minimum and the angular divergence is maximized.
- **Coordinate Correlation**: a statistical dependence between phase-space coordinates (e.g., x correlated with δ in a dispersive plane). Trajectory reconstruction exploits these correlations to infer unmeasured quantities.

These terms may be used in conjunction with each other to describe the optical properties of the system. For example, a focus does not need to be achromatic. Optics specific to ARIS are discussed in the next subsection.

C.2 The Optics of ARIS

ARIS is a third-generation fragment separator designed to efficiently collect, purify, and deliver rare isotope beams produced via projectile fragmentation. The system is composed of two major optical sections: a vertical pre-separator followed by a horizontal C-Bend. A schematic overview of the full system is shown in Figure 1. The following subsections describe the optical principles and operating modes that are most relevant for cross section measurements and trajectory reconstruction.

C.2.1 Momentum Compression

The pre-separator constitutes the first stage of separation in ARIS and plays a critical role in shaping the longitudinal phase space of the secondary beam. Of particular importance is its ability to perform *momentum compression*, a technique that reduces the longitudinal momentum (or velocity) spread of the fragments and thereby increases the effective momentum acceptance of the separator.

The principles and formal description of momentum compression are detailed in Ref. [35]. In brief, momentum compression exploits the correlation between momentum and energy-loss in matter. Fragments with higher momentum lose more energy when passing through a wedge-shaped degrader placed at a dispersive focal plane, while lower-momentum fragments lose less. With appropriate optical matching, this differential energy-loss reduces the momentum spread of the beam downstream of the degrader.

The principal benefit of momentum compression is an increase in the number of fragments that fall within the downstream momentum acceptance of the separator. The trade-off is an increase in transverse phase space, both as a result of the momentum compression and because the wedge material introduces additional angular and spatial spread through multiple scattering and energy-loss straggling. A schematic illustration of the momentum compression process is shown in Figure 42.

After the pre-separator, the beam is transported into the C-Bend. The transition between these two sections is optically significant because it involves an effective rotation of the beam coordinates: the dispersive plane changes from the vertical direction (y) in the pre-separator to the horizontal direction (x) in the C-Bend. This rotation is dictated both by the physical layout of the facility – transporting the beam from below ground to ground level – and by optical considerations.

Following momentum compression, the transverse phase space in the dispersive plane of the pre-separator expands in proportion to the compression factor (three in the standard ARIS configuration). If left unaltered, this enlarged phase space would reduce downstream acceptance. By rotating the coordinate system, the dispersive plane is transferred to the orthogonal transverse direction, which was not affected by the momentum compression process. This preserves acceptance in the C-Bend while retaining the benefits of the reduced momentum spread.

C.2.2 Optical Modes of Operation

All particle identification measurements in ARIS are performed in the C-Bend section of the separator. The C-Bend contains five principal focal planes, labeled DB1 through DB5. DB1

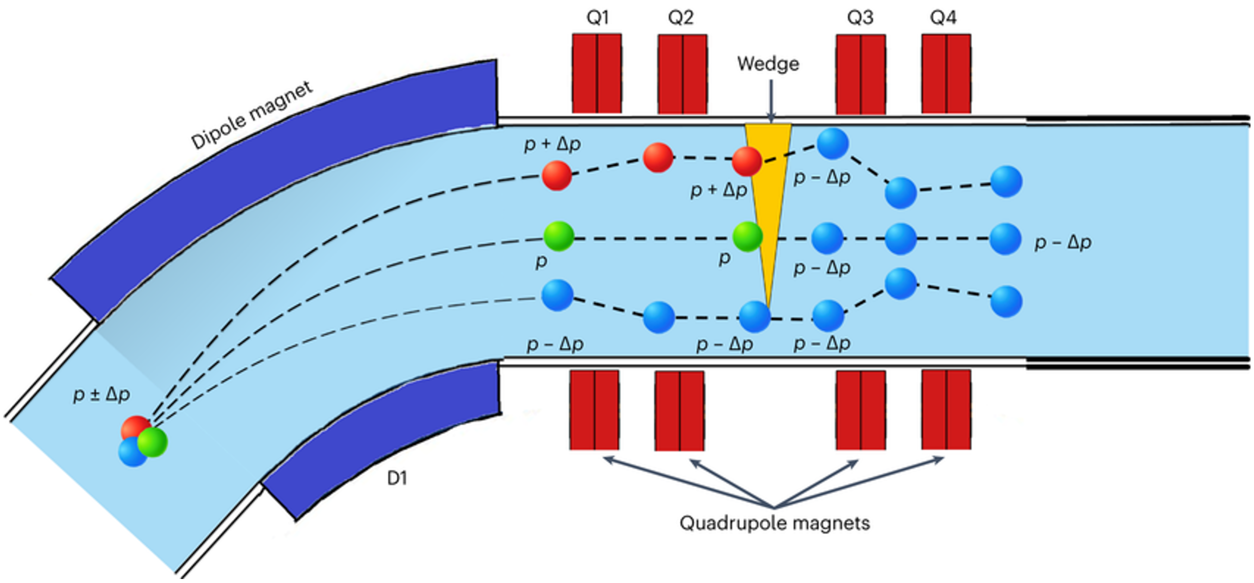

Figure 42: Schematic overview of momentum compression. Identical particles with different initial momenta (color scheme) are spatially separated at a dispersive focal plane and pass through a wedge-shaped degrader, resulting in a reduced momentum spread downstream. Paths of the particles are traced through the system. Taken from Ref. [36].

marks the entrance to the C-Bend and corresponds to the coordinate rotation point between the pre-separator and the horizontal transport section.

In the most commonly used optical configuration, known as the high-acceptance **CB2 mode**, DB2 and DB4 are dispersive focal planes, while DB3 and DB5 are achromatic. DB4 plays a central role in particle identification, as position measurements at this plane are used to correct the magnetic rigidity ($B\rho$) of individual fragments. DB5 marks the end of the fragment separator.

An alternative configuration, the high-resolution **CB1 mode**, may also be employed. In this mode, the optics are tuned such that only a single dispersive focal plane exists at DB3, prioritizing momentum resolution over acceptance.

While operating in CB2 mode, DB5 may be configured in one of two optical conditions. In the *focus* setting, DB5 serves as a focal plane for experiments terminating at the separator, such as dedicated new-isotope searches. In the *transmission* setting, DB5 is tuned to efficiently transport the beam to downstream experimental areas.

The pre-separator itself supports two primary modes of operation: k1 and k3. The k3 mode, which provides a momentum compression factor of three, is by far the most commonly used configuration. The k1 mode, in which no momentum compression is applied, is employed in cases where compression offers no benefit or is detrimental to transmission or resolution. The pre-separator and C-Bend modes may be combined arbitrarily, though the k3CB2 configuration is overwhelmingly dominant in experiments performed at FRIB.

The ideal first-order optics for the k3CB2 mode are shown in Figure 43. Magnifications are shown in the left plot, focuses are shown in the middle plot, and the spatial dispersion is shown in the right plot. The plotted global matrix elements illustrate the evolution of focusing and dispersion along the separator and clearly show the coordinate rotation between the pre-separator and C-Bend.

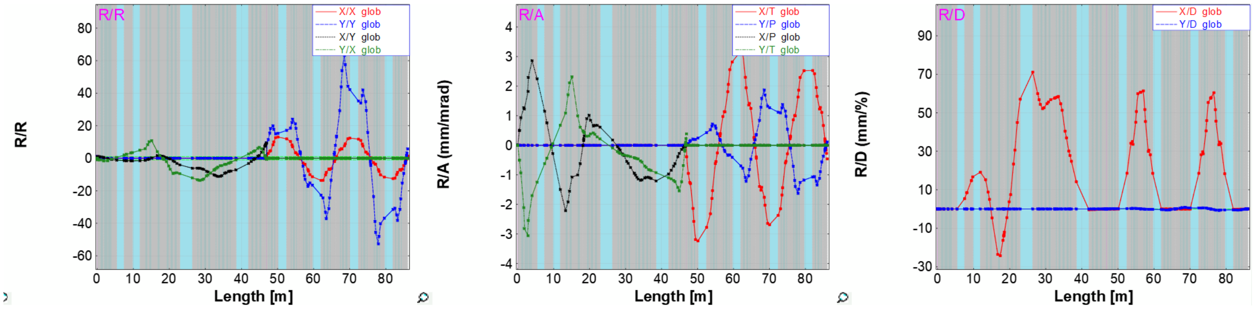

Figure 43: Ideal first-order optics of the k3CB2 mode of ARIS. The plotted quantities represent global transfer matrix elements as a function of position along the beamline. The rotation of the dispersive plane following the pre-separator is clearly visible.

C.2.3 Secondary Beam Purification

This section provides a brief primer on how secondary beams are purified for experiments at FRIB. Understanding this process is essential context for both rare isotope experiments and the production cross section measurements described throughout this manual.

Secondary beam purification is necessary because projectile fragmentation is an inherently stochastic process. In a high-energy collision between the primary beam and the production target, nucleons are randomly abraded from the projectile nucleus and the resulting excited pre-fragment subsequently ablates particles according to its excitation energy (see subsection 7.3). As a result, a single reaction produces a broad distribution of fragments spanning many atomic numbers, mass numbers, and charge-states. In principle, nearly any lighter combination of protons and neutrons may be produced[34]. The role of the fragment separator is to isolate a specific subset of these fragments – the isotopes of experimental interest – from this overwhelming background.

In practice, secondary beam purification occurs through a combination of two complementary mechanisms: *optical separation* and *physical separation*. These mechanisms are interleaved along the separator and act together to progressively increase the purity of the transmitted beam.

C.2.3.1 Optical Separation

Optical separation exploits the dependence of particle trajectories on magnetic rigidity, $B\rho = p/q$, where p is the fragment momentum along the optical axis and q is the ionic charge. Dipole magnets are tuned to the rigidity corresponding to the fragment of interest. Particles with different A/q values experience different bending angles in the magnetic field and are therefore displaced from the reference trajectory. Fragments whose rigidity differs sufficiently from the tuned value will strike the beam pipe or magnet apertures and be removed from the beam.

---

[34] Nucleon pickup reactions can also occur for large impact parameters, though with much smaller probability at intermediate energies.

This rigidity-based filtering defines one of the primary *selection lines* of a fragment separator. A schematic illustration of these selection lines is shown in Figure 44. While powerful, optical separation alone is insufficient: many fragments with different (A, Z) combinations can share similar A/q values and therefore follow nearly identical trajectories through the dipoles.

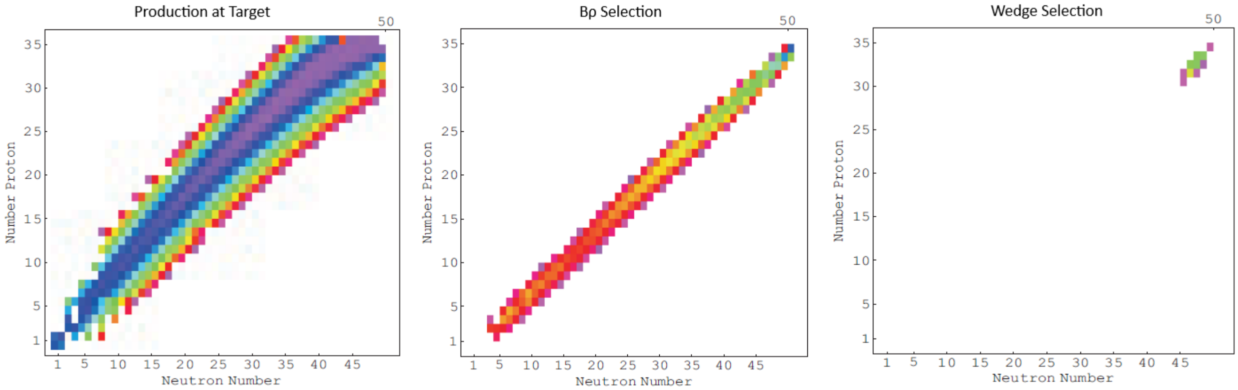

Figure 44: Illustration of selection lines and the resulting increase in beam purity achieved through magnetic rigidity $(B\rho)$ selection and energy-loss degradation (dE). From Ref. [37]

C.2.3.2 Physical Separation

Physical separation relies on the interaction of beam particles with matter to further purify the secondary beam beyond what is achievable through magnetic rigidity selection alone. This is accomplished primarily through energy-loss mechanisms and geometric constraints imposed by the beamline.

The most important physical filtering element is the energy-loss degrader, typically implemented as a wedge-shaped material placed at a dispersive focal plane. As fragments traverse the degrader, they lose energy according to the Bethe–Bloch formalism, with the leading dependence scaling approximately as

$$\frac{dE}{dx} \propto Z_{\text{eff}}^2,$$

where Z_{eff} is the effective ionic charge of the fragment. As a result, fragments with different atomic numbers but similar magnetic rigidities will experience different energy-losses when passing through the degrader. The wedge geometry is chosen such that the fragment of interest emerges with the correct momentum to remain centered in the acceptance of the downstream dipole magnets, while contaminants are over- or under-degraded and subsequently bent out of the beam. This combination of dispersive optics and energy-loss defines a second, independent selection line in the separator.

A further complication in physical separation arises from the presence of multiple ionic charge-states. Following fragmentation and passage through materials in the separator, ions may not be fully stripped of their atomic electrons, especially for higher-Z fragments or at lower beam energies. Since the magnetic rigidity depends on the ratio $B\rho = p/q$, different charge-states of the same isotope follow different trajectories through the separator. In some cases, partially stripped ions can possess nearly identical magnetic rigidities to fully stripped ions of a different isotope, allowing them to survive purely optical selection and contaminate the transmitted beam.

Energy-loss degraders help mitigate charge-state ambiguities because ions with different effective charges lose different amounts of energy in matter, even if their initial magnetic rigidities are similar. Additionally, operation at sufficiently high beam energies strongly favors fully stripped charge-states, reducing the overall complexity of the transmitted beam. Nevertheless, residual charge-state contamination is an intrinsic feature of in-flight separation and must ultimately be resolved during particle identification and transmission analysis. This consideration is particularly important near the limits of separator acceptance and in experiments aimed at discovering or characterizing the most weakly bound isotopes.

As mentioned previously in this manual, beam particles may interact with a wedge not only through energy-loss but also via nuclear reactions, undergoing further fragmentation within the material itself. These secondary reactions contribute to contamination of the transmitted beam and can reduce the yield of the isotope of interest. While optical separation can remove a portion of this contamination, additional physical separation stages are often required to maintain acceptable beam purity. This consideration motivates the use of multiple wedges in ARIS.

Depending on the experimental requirements, two wedges may be present in the system: the primary wedge in the pre-separator and a secondary wedge at DB2. The pre-separator wedge is typically thick and is responsible for momentum compression as well as initial physical separation. In contrast, the DB2 wedge is deliberately made thinner to minimize additional fragmentation while still providing incremental separation of contaminants that survive the first stage. The DB2 wedge does not perform momentum compression; rather, it serves as a refinement stage that improves beam purity at the cost of only a modest reduction in transmission.

The use of multiple wedges therefore represents a balance between purity and yield. For experiments targeting extremely rare isotopes, where background suppression is critical, the additional physical filtering provided by a second wedge can be essential. Conversely, for experiments where maximum transmission is prioritized, the use of the DB2 wedge may be avoided altogether.

In addition to degraders, physical apertures such as slits and collimators may be inserted at strategic locations to block regions of phase space known to be populated by unwanted species. While effective, slits necessarily reduce transmission and must be used judiciously, particularly in experiments targeting extremely rare isotopes. A simplified schematic of a two-dipole, one-wedge purification stage is shown in Figure 45.

C.3 Trajectory Reconstruction

As mentioned previously, trajectory reconstruction improves particle identification (PID) resolution by correcting for event-by-event kinematic variations from the reference trajectory that are not captured by nominal optical settings. In practical terms, it allows one to undo the effects of finite beam emittance, momentum spread, and higher-order optical aberrations by reconstructing the actual path each particle takes through the separator.

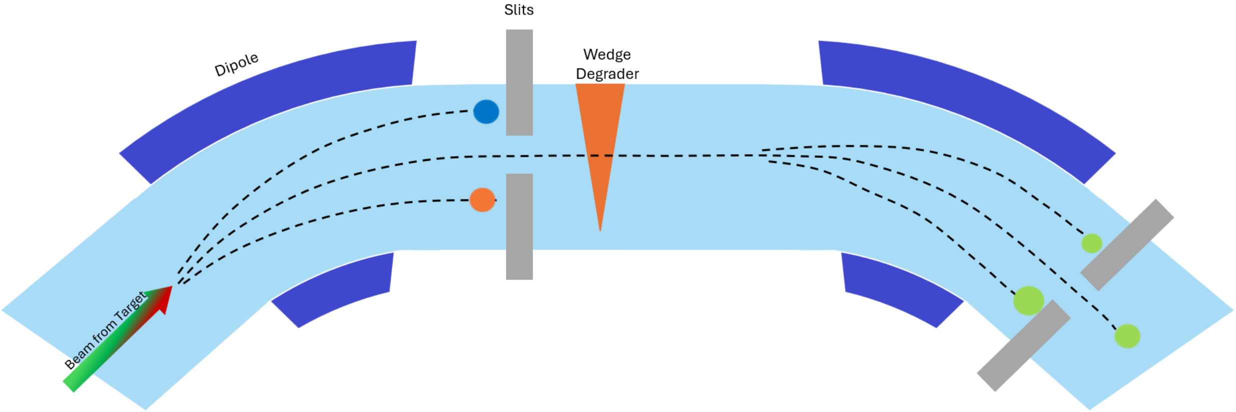

Figure 45: Schematic illustration of secondary beam purification using a wedge degrader between two dipole magnets. This demonstrates the combined action of optical ($B\rho$) and physical (energy-loss) selection lines shown in Figure 44.

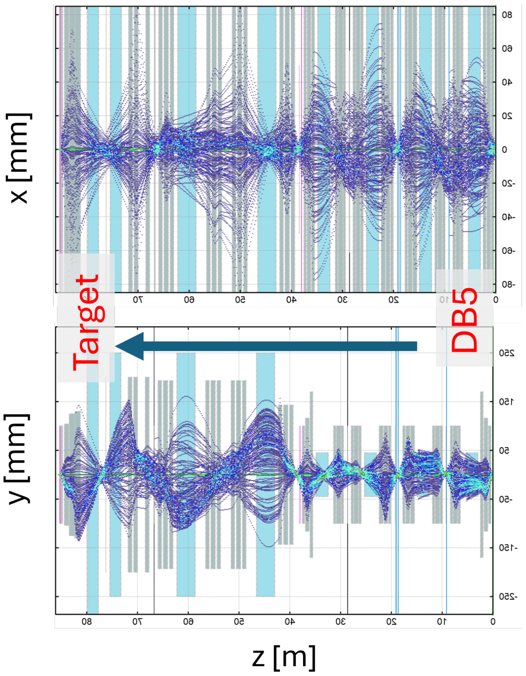

Figure 46: Calculations of particle trajectories traced backward from DB5 to the target position.

In a broad sense, trajectory reconstruction is the process of inferring a particle's full phase-space coordinates at one location in the beamline (typically the production target) from measurements made downstream. This inference relies on precise measurements of final positions, angles, time-of-flight, and energy-loss, together with unambiguous particle identification and detailed knowledge of the magnetic settings and optical response of the system.

While trajectory reconstruction is most often introduced as a tool for improving PID, its utility extends well beyond kinematic corrections. By reconstructing particle trajectories across the acceptance of the separator, one can empirically characterize the optics, dispersion, and effective acceptance of the system. In this way, trajectory reconstruction serves both as a correction technique and as a diagnostic tool for validating optical models.

Work has been conducted to characterize ARIS using this approach. Data collected at DB5 have been traced backward through the system to the production target. In addition to improving PID resolution, these studies provide insight into the transport properties of the separator and the kinematic properties of the reaction products themselves. Preliminary trajectory reconstruction results for ARIS are shown in Figures 46 and 47.

The foundation of trajectory reconstruction as applied to PID lies in the fact that individual particles do not follow the reference trajectory. Each fragment experiences small but measurable deviations in momentum and path length as it traverses the separator. These deviations directly impact two key observables used in PID: time-of-flight and magnetic rigidity.

The path length traversed by a particle is directly tied to the measured time-of-flight. In standard analysis, a fixed path length – corresponding to the reference trajectory – is assumed when converting timing signals to velocity. However, particles that deviate from the reference orbit traverse slightly longer or shorter paths. These differences introduce a systematic broadening of the time-of-flight distribution that cannot be removed by detector resolution alone. By reconstructing the actual trajectory of each particle, event-by-event path length corrections can be applied, significantly improving the intrinsic ToF resolution.

Magnetic rigidity, $B\rho$, quantifies the bending strength required to transport a particle through a magnetic field and is proportional to its momentum divided by its charge. As discussed in Appendix E, $B\rho$ is a critical input to the determination of the mass-to-charge ratio A/q. In analogy to the path length case, particles exhibit event-by-event momentum deviations relative to the reference particle. While the dipole magnets set a global rigidity, local deviations can be inferred from position measurements at dispersive focal planes. In ARIS, these corrections are applied using position measurements at DB4, which is a dispersive focus in the CB2 optics mode.

Corrections to the magnetic rigidity are particularly important when ARIS is operated in CB1 mode, where only a single dispersive focus is available. The impact of these corrections is illustrated in Figure 48. Prior to trajectory reconstruction, the same charge-state appears to populate different values of A/q at different magnetic rigidities – an unphysical result arising from uncorrected momentum deviations. After applying trajectory-based corrections, this correlation is removed, and the expected discrete charge-state structure is recovered.

Additional measurements performed during a ^{198}Pt experiment investigated the consistency of momentum reconstruction across different segments of the separator. The reconstructed momentum deviations for the DB1-3 and DB3-5 sections show a linear correlation with unit slope (Figure 49), indicating good agreement between the calculated dispersions and the measured transport. This agreement provides an important validation of both the optical model and the reconstruction procedure.

As discussed in paragraph 2.2.1.2, `SpecTcl` supports first- and second-order kinematic corrections for trajectory reconstruction. In principle, however, corrections of arbitrary order may be applied. Previous work with the S-800 spectrograph demonstrated trajectory reconstruction to fifth order using COSY Infinity[35] transport maps [7, 38]. These higher-order approaches offer a path forward for further refinement of reconstruction techniques in ARIS as detector resolution and statistics improve.

C.3.1 Detector Calibration and Connection to Transmission

Trajectory reconstruction is only as reliable as the detector information on which it is based. Accurate reconstruction therefore requires that all position-, timing-, and energy-sensitive detectors used in the analysis be well calibrated, stable over time, and correctly aligned within the optical coordinate system of the separator.

---

[35] https://www.bmtdynamics.org/cosy/

Position-sensitive detectors at dispersive and non-dispersive focal planes must be calibrated to convert raw signals into physical coordinates with linear response and minimal distortion across the active area. Any nonlinearity or misalignment directly propagates into reconstructed momentum and path length, degrading both PID resolution and the physical interpretability of reconstructed quantities. Similarly, timing detectors must be precisely calibrated and synchronized, as residual offsets or drifts can mask the improvements gained from path length corrections. Energy-loss detectors used for PID and charge-state determination must also be stable, as miscalibration can introduce ambiguities that cannot be resolved through reconstruction alone.

Beyond its role in improving event-by-event kinematics, trajectory reconstruction provides a powerful mechanism for empirically determining the acceptance and transmission of the separator. By mapping reconstructed trajectories back to the production target, one can determine which regions of phase space are transmitted to the final focal plane and which are lost due to optical constraints, apertures, or higher-order aberrations. This information can be used to construct realistic, data-driven acceptance functions that complement or refine those obtained from ion-optical simulations.

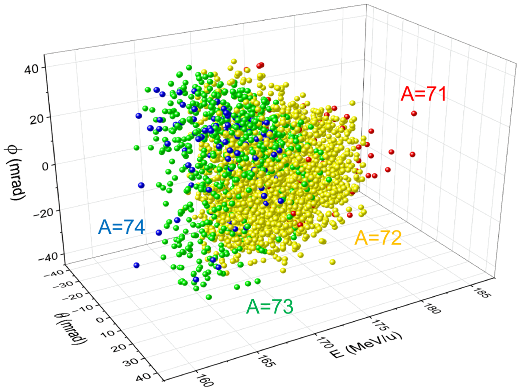

Figure 47: Reconstructed distributions of iron fragments at the target position as a function of energy and transverse angles.

In the context of cross section measurements, this feedback is particularly important. Transmission corrections are a dominant systematic uncertainty, especially for rare isotopes produced near the limits of acceptance. Trajectory reconstruction allows one to quantify these effects experimentally by correlating reconstructed phase-space coordinates with observed yields. In this way, reconstruction serves as a bridge between measured yields and absolute production cross sections, strengthening the connection between experiment and model.

C.3.1.1 Caveats and Limitations

While trajectory reconstruction is a powerful tool, it is not a panacea. The method relies on the accuracy of the underlying optical model, the stability of magnetic fields, and the quality of detector calibrations. Systematic errors in any of these inputs can lead to overcorrection or the introduction of artificial correlations. In addition, finite detector resolution and incomplete phase-space coverage limit the order to which meaningful corrections can be applied; higher-order terms may fit statistical fluctuations rather than true physical effects.

Trajectory reconstruction also implicitly assumes that particles traverse the separator without undergoing additional interactions. Secondary reactions in degraders, detectors, or other materials introduce irreducible uncertainties that cannot be corrected kinematically. As such, reconstruction should be applied judiciously, validated against known benchmarks (e.g., charge-state behavior or rigidity scans), and interpreted in concert with simulation and physical intuition.

When used carefully, trajectory reconstruction significantly enhances the resolving power and quantitative reliability of fragment separators like ARIS. When used uncritically, it can obscure as much as it reveals. As with all correction techniques, its greatest strength lies in informed application and rigorous cross-checking.

C.3.2 Empirical Transfer Matrix Determination

There exists another method to extract transfer matrices between two focal planes at which transverse position and angle measurements are available: regression analysis [39].

In its simplest form, regression is the determination of correlations among measured variables. In the context of ion optics, multivariate regression provides a natural and powerful framework for reconstructing the effective transfer matrix between two locations in the beamline using experimentally measured phase–space coordinates. Given sufficiently precise measurements of transverse positions and angles at two focal planes, the elements of the transport matrix may be inferred directly from the data.

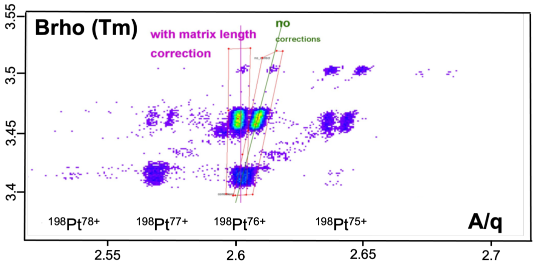

Figure 48: ^{198}Pt charge-states plotted as a function of A/q and $B\rho$ during a momentum scan in CB1 mode. Prior to trajectory reconstruction, an unphysical correlation is observed.

In this approach, each transfer matrix element corresponds to the slope of the correlation between a final coordinate and one of the initial coordinates. For example, the element $(x|x)$ represents the correlation between the final horizontal position and the initial horizontal position, while $(x|\theta)$ quantifies the sensitivity of the final position to the initial horizontal angle. When momentum information is included, dispersion terms such as $(x|\delta)$ can also be extracted.

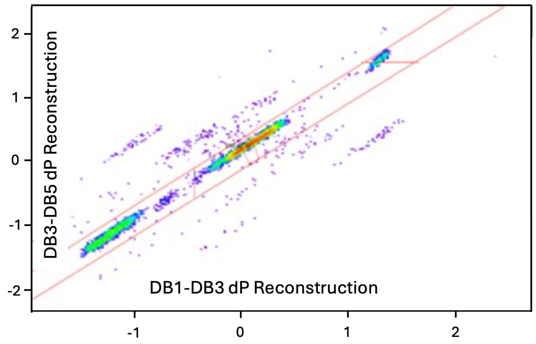

Figure 49: Reconstructed momentum deviations, $\Delta B\rho/B\rho$, for the DB1-3 and DB3-5 segments of the C-Bend for ^{198}Pt fragments.

As emphasized in the previous section, accurate detector calibration is essential. Even small systematic offsets in position or angle measurements can bias the extracted matrix elements. This requirement places stringent demands on both the absolute calibration and the resolution of the position-sensitive detectors. Modern PPAC systems typically achieve millimeter-level position resolution, which is sufficient for this purpose. Although each individual measurement carries an intrinsic uncertainty, these uncertainties are statistically averaged down when a large ensemble of particles is used in the regression.

Assuming well-calibrated detectors, the measured phase–space coordinates encode the true transport of particles through the system, including contributions from optical aberrations of all orders. In practice, however, only first- and second-order matrix elements can be reliably extracted using regression, as higher-order correlations require prohibitively large data sets and rapidly become dominated by detector resolution and unmodeled material effects.

A key point in this analysis concerns the treatment of the momentum deviation δ. In ARIS, the momentum coordinate is commonly expressed operationally as $\delta = \Delta B\rho/B\rho$. For optical segments in which no wedge or significant material is present – such as the DB3–DB5 section of the C-Bend – the fragment momentum is conserved to good approximation. Under these conditions, the momentum deviation at the initial and final focal planes is effectively the same, $\delta_{\text{initial}} \approx \delta_{\text{final}}$. As a result, dispersion-related correlations extracted from regression are not distorted by trajectory reconstruction corrections, which act only as common-mode shifts to δ. This ensures that the regression-derived dispersion matrix elements reflect the true optical response of the system and are not circularly influenced by the simulated transport matrix already implemented in `SpecTcl`.

The principal advantage of extracting transfer matrices through regression is that it provides an empirical cross-check of the ion-optical simulations. Agreement between the simulated and experimentally derived matrices indicates that the optics are well understood and that the dominant transport properties are correctly modeled. Discrepancies between the two are expected to arise from finite detector resolution, energy and angular straggling in materials, and higher-order aberrations that are not explicitly included in first-order simulations. In this way, regression-based matrix extraction serves both as a validation of the optical model and as a diagnostic tool for identifying limitations in the simulated description of the beamline.

Currently, only a single PPAC is installed at DB4. As a consequence, while a complete first-order transfer matrix may be extracted between DB3 and DB5 – where both position and angle measurements are available – only partial transfer matrices can be obtained for the subsegments DB3–DB4 and DB4–DB5.

The planned installation of a second PPAC at DB4 will remove this limitation by enabling direct measurements of both transverse position and angle at that focal plane. This upgrade will unlock an additional and powerful optical consistency check. For a given particle, the transport through the system is deterministic and identical for each event. Consequently, the product of the experimentally extracted matrices for the two subsegments, should reproduce the independently extracted DB3–DB5 transfer matrix within experimental uncertainties:

$$M_{\mathrm{DB3}\to\mathrm{DB5}} = M_{\mathrm{DB4}\to\mathrm{DB5}} \cdot M_{\mathrm{DB3}\to\mathrm{DB4}} \tag{24}$$

Agreement between these matrices would provide a stringent validation of the measured optics, while systematic deviations would offer direct insight into unmodeled aberrations, detector systematics, or material effects localized to a specific segment of the C-Bend.

Appendix D Quantitative Gate Analysis

Quantitative gate analysis is required whenever absolute fragment yields are central to the scientific outcome of an experiment. This situation most commonly arises at low statistics, where small changes in gate placement can produce large fractional changes in extracted counts. In these regimes, visual inspection alone is insufficient; gate performance must be evaluated systematically and quantitatively.

This appendix complements the qualitative cleaning philosophy described in subsubsection 2.2.3. There, gates are introduced as tools to suppress unphysical events while preserving valid fragment counts. Here, the emphasis shifts to measuring gate performance and verifying that final yields are stable under reasonable variations in gate definition.

Quantitative gate analysis becomes especially critical when searching for very exotic isotopes or claiming first observations[36], where statistical margins are small and the consequences of over- or under-cleaning are significant.

D.1 Conceptual Framework

The central idea of quantitative gate analysis is to partition PID space into two classes of regions:

- **Good regions**: gates surrounding identified isotope blobs that contain physically meaningful events.
- **Bad regions**: gates placed between isotope blobs, where events are presumed to be dominated by background, mis-reconstructed particles, or unphysical combinations of observables.

Effective cleaning gates should strongly suppress counts in bad regions while minimally affecting counts in good regions. A gate that reduces both indiscriminately is suboptimal, even if the resulting PID spectrum appears visually clean.

An example of this partitioning is shown in Figure 50, where isotope and bad regions are explicitly marked. The black line separates primary fragments (above) from wedge products and aberration-transported fragments (below), as determined using `LISE`$^{++}$ (see subsection 5.2). Gates should be defined not only on well-populated isotope blobs but also on low-statistics or borderline isotopes, as these are typically the most sensitive to over- or under-cleaning.

D.2 Procedure

The quantitative analysis proceeds as follows:

1. Starting from the final calibrated PID spectrum (with all PID variables validated), define gates around many identified isotope blobs. These constitute the initial set of good regions.
2. Define additional gates in the spaces between isotope blobs. These gates should follow the general topology of the PID spectrum and sample regions where no physical fragments are expected.

---

[36] FRIB maintains a public database of isotope discoveries and researcher rankings: `https://frib.msu.edu/public-engagement/learning-resources-and-programs/brief-history-of-rare-isotopes/rankings`

3. Record the initial event counts in each good and bad region prior to applying additional cleaning gates.
4. Apply one cleaning gate at a time (e.g., timing, energy-loss, position, or dispersion cuts), and record the change in counts for each region.

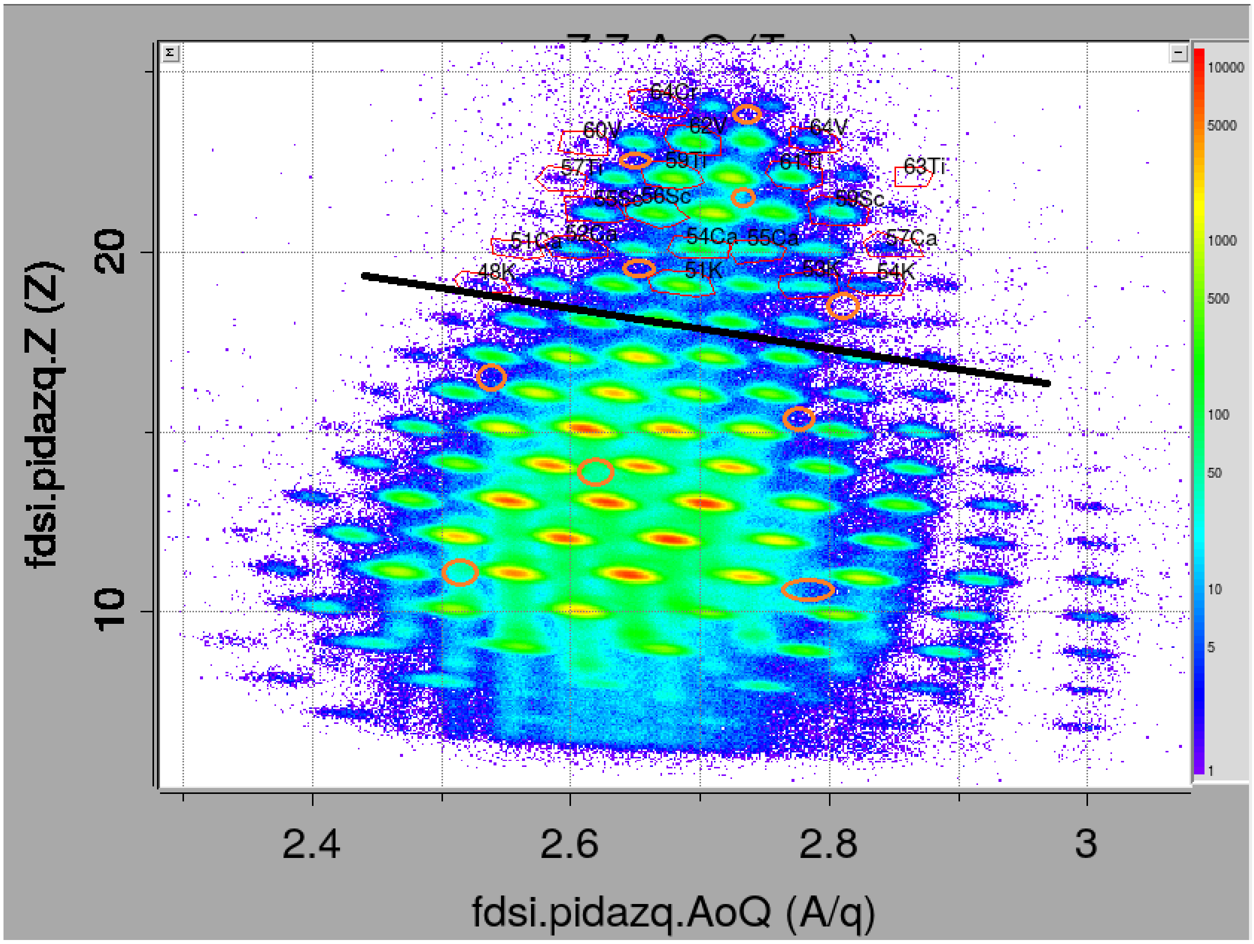

Figure 50: Final calibrated PID spectrum with fragment-identification gates and between-blob ("bad region") gates defined. Orange circles indicate regions between isotope blobs used to quantify background suppression. The black line separates primary fragments (above) from wedge products and aberration-transported fragments (below).

A cleaning gate is considered effective if it produces a substantial reduction in bad-region counts while causing only a small and quantifiable reduction in good-region counts. Because some unphysical events can mimic valid fragment observables, some loss in good regions is unavoidable. The objective is not zero loss, but a loss that is small, understood, and justified.

D.3 Diagnosing Problematic Gates

If a particular cleaning gate produces a large reduction in one or more good regions, further investigation is required. In such cases:

- Project the affected isotope gate onto the spectrum associated with the cleaning cut.
- Examine whether valid events cluster near the gate boundary.
- If so, loosen the gate slightly and repeat the quantitative evaluation.

This process helps ensure that physically meaningful events are not excluded due to overly aggressive gate placement.

Special care is required for energy-loss correlation gates. In ΔE versus ΔE spectra, valid fragments often extend along diagonal ridges corresponding to physically allowed trajectories. As illustrated in Figure 9, legitimate events may lie far from the central density of a blob while remaining aligned with the diagonal trend. Gates in these spaces must therefore be sufficiently elongated to retain such events, particularly for rare isotopes near the limits of acceptance.

D.4 Best Practices

Quantitative gate analysis should be performed after final PID calibration and isotope identification are complete, but before yield extraction and statistical uncertainty assignment. Performing the analysis earlier risks conflating calibration effects with gate performance. Performing it later risks invalidating the yield statistics derived in subsection 3.2.

The results of a quantitative gate analysis should be documented explicitly, including:

- The fractional change in good- and bad-region counts for each cleaning gate.
- Any gates that required modification.
- The final gate definitions used for yield extraction.

This documentation strengthens confidence in reported yields and provides transparency and reproducibility for future re-analyses or independent comparisons.

Appendix E Particle Identification

This appendix summarizes the physical principles, measured observables, and mathematical relationships underlying particle identification (PID) as implemented in this analysis. A complete first-principles derivation of the relevant equations is beyond the scope of this manual.[37] Instead, the emphasis is on clarifying how experimentally measured quantities are combined to infer intrinsic particle properties, and on documenting the assumptions and limitations inherent in this procedure.

---

[37] More detailed derivations are provided in the appendix of Ref. [40].

E.1 Overview of Measured and Derived Quantities

Particle identification proceeds through a strictly ordered chain of dependencies. Magnetic rigidity and time-of-flight determine the mass-to-charge ratio A/q. The total kinetic energy, together with A/q and β, determines the ionic charge-state q. Only after q is established can the atomic mass number A be reconstructed. Finally, the atomic number Z is inferred from energy-loss measurements, which depend explicitly on velocity.

Errors introduced at any stage propagate forward and cannot be corrected downstream. PID calibration must therefore proceed in the order:

$$B\rho,\ \text{ToF} \to \beta, \gamma \to A/q$$

$$\left.\begin{aligned} \text{TKE} &\to q \\ dE &\to Z \\ A/q,\ q &\to A \end{aligned}\right\} \begin{array}{c} \textbf{PID} \\ \textbf{Parameters} \end{array}$$

It is therefore useful to distinguish explicitly between experimentally measured observables and quantities inferred through PID calculations:

- **Measured**: magnetic rigidity $B\rho$, time-of-flight, detector energy-loss signals, and total deposited energy.
- **Derived**: β, γ, A/q, ionic charge-state q, atomic mass A, and atomic number Z.

None of the intrinsic particle properties (A, q, or Z) are measured directly. Instead, they are reconstructed through calibrated combinations of measured quantities and empirical model relations. This distinction is critical when diagnosing PID artifacts, identifying failure modes, or assessing systematic uncertainties.

E.2 Mass-to-Charge Ratio and Mass Reconstruction

Throughout this manual, the quantity used for particle identification and mass reconstruction is referred to as the mass-to-charge ratio, denoted A/q. Strictly speaking, this is an approximation. What is measured experimentally is not the nuclear mass number A, but the total mass M of the ion, including any bound electrons, divided by its charge-state q. The physically correct quantity is therefore M/q.

For an ion with atomic number Z, mass number A, and charge-state q, the total mass can be written as

$$M = M_{\text{nucleus}} + (Z - q)m_e - E_{\text{bind}}/c^2 \tag{25}$$

where m_e is the electron mass and E_{bind} is the total electronic binding energy. In fragment separators operating at intermediate energies, ions are highly stripped, and $q \approx Z$ for most species of interest. As a result, the number of bound electrons is small, and the contribution of electronic binding energies is negligible compared to the nuclear mass.

Quantitatively, the nuclear mass is of order $A \times 931.5\ \text{MeV}/c^2$, while the mass contribution from even several electrons is at the level of a few MeV/c^2. This represents a relative correction of order 10^{-4} or smaller, well below the resolution of in-flight particle identification systems and far below other dominant sources of uncertainty such as time-of-flight resolution, energy-loss straggling, and optical aberrations. Consequently, for the purposes of isotope identification and cross section measurements, the distinction between M/q and A/q is numerically insignificant.

Despite this, the use of A/q rather than M/q is more than a casual shorthand. In experimental practice, the goal of mass reconstruction is to identify the integer mass number A associated with a given nuclear species, independent of its charge-state. Expressing results in terms of A/q makes this goal explicit and aligns naturally with how particle identification plots are interpreted: different charge-states of the same isotope appear as distinct loci in A/q, but they all correspond to the same underlying mass number A. This convention also facilitates direct comparison with reaction models, mass tables, and systematics, which are all formulated in terms of nuclear mass number rather than total ionic mass.

For these reasons, the notation A/q is retained throughout this manual. It should be understood as an experimentally reconstructed proxy for the true mass-to-charge ratio M/q, with the implicit assumption that electronic contributions to the ion mass are negligible at the level relevant for rare isotope production and cross section analysis.

The fundamental relations governing mass and charge reconstruction are:

$$\frac{A}{q} = \frac{B\rho}{3.1071\,\beta\,\gamma}, \tag{26}$$

$$q = \frac{\text{TKE}}{(\gamma - 1)\,u\,A/q}, \tag{27}$$

$$A = \left(\frac{A}{q}\right) q = \frac{\text{TKE}}{(\gamma - 1)\,u}, \tag{28}$$

where

- A/q is the mass-to-charge ratio (amu/e),
- $B\rho$ is the magnetic rigidity (T·m),
- $\beta = v/c$ and $\gamma = (1 - \beta^2)^{-1/2}$ are the relativistic kinematic parameters,
- q is the ionic charge-state,
- TKE is the total kinetic energy of the ion,
- u is the atomic mass unit (931.5 MeV), and
- A is the atomic mass number.

Equation (26) follows directly from the relativistic momentum relation $p = \gamma m v$, rewritten in units appropriate for heavy-ion spectrometers. The numerical constant in the denominator represents the combination uc/e, evaluated such that $B\rho$ is expressed in T·m and A/q is obtained in amu/e. This relation highlights the central role of both magnetic rigidity and time-of-flight measurements in determining A/q.

It should be noted that Equation (26) implicitly assumes that higher-order optical aberrations and large-acceptance effects have been adequately corrected. In fragment separators operating at large momentum or angular acceptance, residual higher-order distortions can introduce correlations that broaden or distort the reconstructed A/q distributions if not properly accounted for. Such effects must be addressed through appropriate optical corrections and validated through PID consistency checks, as performed in subsubsection 2.2.1.

Equation (27) follows from the relativistic kinetic energy expression $T = (\gamma - 1)mc^2$. Determination of the ionic charge-state therefore relies on accurate measurements of A/q, β, and the total kinetic energy. This expression further assumes that the reconstructed total kinetic energy represents the full residual kinetic energy of the fragment after all upstream materials, including degraders and detectors, and that no significant unmeasured energy-loss occurs downstream of the final energy-loss detector.

Equation (28) is algebraically straightforward but physically important: the atomic mass number A cannot be uniquely identified without either a reliable charge-state determination (derived from high quality TKE and ToF measurements) or an explicit assumption about the charge-state of the fragment[38]. This coupling of rigidity–timing information to energy-loss information motivates the emphasis placed on total kinetic energy calibration elsewhere in this manual.

In many intermediate- to high-energy rare-isotope experiments (typically $\gtrsim$ 100–400 MeV/u), fragments are predominantly fully stripped at the final focal plane, such that $q \approx Z$. When this condition is satisfied, the reconstructed charge-state distribution collapses to a single dominant peak, and the assumption $q = Z$ may be safely applied for yield extraction.

For heavier fragments or lower velocities, however, multiple charge-states may be populated. In such cases, explicit charge-state reconstruction using total kinetic energy is essential. Failure to resolve or properly account for partially stripped charge-states can lead to incorrect mass assignments and distorted isotopic yields. The presence of multiple charge-states should therefore always be assessed directly in Z–q or equivalent PID spectra.

E.3 Atomic Number Reconstruction

The final PID observable is the atomic number Z, which is inferred from the measured energy-loss of the ion in silicon detectors. This procedure relies on heavy-ion energy-loss in matter and incorporates both theoretical guidance and empirical calibration. The equations presented here reflect the simplified, implementation-specific forms used internally by `SpecTcl`.

A reduced, velocity-dependent energy-loss term is first defined as

$$dE_v = \frac{1}{\beta^2} \log\left(\frac{5930}{\beta^2 - 1}\right) - 1, \tag{29}$$

which captures the dominant velocity dependence of the stopping power. This expression is inspired by the Bethe-Bloch formalism but does not represent the full stopping-power equation. Rather, it provides a monotonic, velocity-dependent scaling that enables empirical

---

[38] For example, assuming fully stripped ions.

linearization of Z in PID space[39]. The numerical constants have been evaluated for silicon detectors and absorbed into an empirical parameterization optimized for PID calculations.

An intermediate variable is then defined as

$$z_v = \frac{e_{\text{reduced}}}{(dE_v)^{Z_{\log\beta}}}, \tag{30}$$

where e_{reduced} is the measured energy-loss signal and $Z_{\log\beta}$ is a user-defined parameter controlling the velocity dependence of the effective Bragg curve. In `SpecTcl`, the reduced energy-loss may be formed from a PIN detector, silicon stack segment 0, segment 1, or a weighted combination of multiple detectors.

Finally, the atomic number is calculated as

$$Z = z_v\, Z_{\text{slope2}} + \sqrt{z_v}\, Z_{\text{slope}} + Z_{\text{offset}}, \tag{31}$$

where Z_{slope}, Z_{slope2}, and Z_{offset} are user-defined calibration parameters that map the empirical energy-loss variable onto physical atomic numbers. These parameters are detector- and experiment-specific and must be determined through calibration. A discussion of this calibration can be found in subsubsection 2.2.5.

Equations (29)–(31) again highlight the central role of accurate time-of-flight measurements: the inferred atomic number depends explicitly on β, and timing errors will broaden or distort Z distributions if not properly controlled. Additionally, miscalibrated time-of-flight can also shift the Z distribution.

E.4 Assumptions and Validity

The PID formalism described here assumes intermediate- to high-energy heavy ions for which relativistic kinematics are valid and energy-loss follows smooth Bethe-Bloch-like behavior. It further assumes that charge-states are sufficiently well resolved and that detector response is linear and stable over the relevant dynamic range. At low velocities, for very light ions, or in the presence of unresolved multiple charge-states, the reliability of the reconstructed A, q, and Z may degrade. In such cases, additional data cleaning, alternative gating strategies, or more restrictive assumptions may be required to preserve PID integrity.

E.5 Common PID Failure Modes

Several characteristic features in PID spectra indicate underlying problems:

- **Tilted or curved PID bands** typically indicate timing or magnetic-rigidity miscalibration.
- **Broad or asymmetric Z distributions** often reflect poor energy-loss calibration or unresolved charge-states.
- **Multiple parallel mass bands** are usually the result of multiple charge-states being populated.

---

[39] “PID space” here means a region of the observable space.

- **Discontinuities across detector boundaries** suggest mismatched gain or offset calibrations between detector segments.
- **Fragment-dependent offsets** appearing only for specific Z or A values often indicate uncorrected non-linearities or saturation effects in energy-loss detectors.

Diagnosing and correcting these issues at the PID level is essential before proceeding to yield extraction or cross section analysis.

E.6 Identification of Blobs

Correctly assigning physical meaning to clusters (“blobs”) in particle-identification (PID) spectra is a critical step in rare isotope analysis. A PID blob corresponds to a specific combination of atomic number Z, ionic charge-state q, and atomic mass A, as defined by Equations (26)–(28). Misidentification at this stage propagates directly into incorrect yield extraction and cross section determination.

No single observable uniquely identifies all fragments in an in-flight fragmentation experiment. Instead, blob identification relies on a hierarchy of methods, combining definitive physical anchors with supporting consistency checks. These methods are summarized below and should be applied collectively whenever possible.

E.6.1 Primary Identification Methods

The following methods provide the most robust and model-independent identification of PID blobs and should be prioritized whenever available. Note that not every PID method is available for every experiment. Therefore, knowledge of, and ability to perform, each type of particle identification is an invaluable skill both for online and offline analysis.

PID Holes (Unbound Nuclei)

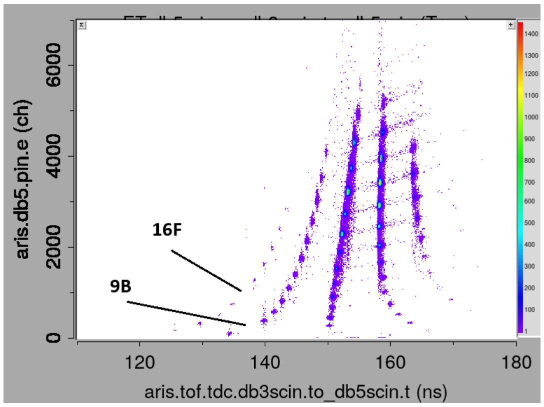

Figure 51: Example of an unbound nucleus PID (^{9}B and ^{16}F).

Certain nuclei are unbound and therefore cannot be produced as transmitted fragments. Their absence manifests as persistent gaps (“holes”) in otherwise smooth isotopic chains in PID space. Because these holes arise from nuclear structure rather than experimental conditions, they provide powerful topological anchors for isotope identification. Once a hole is identified, neighboring blobs can be assigned relative to it with high confidence.

An example of this type of identification is shown in Figure 51. The isotopic line for fluorine is identified. The two isotopes ^{9}B and ^{16}F may be unambiguously identified due to their absence and their relative location. It should be noted that this type of identification requires knowledge of the region in which the fragment separator is tuned (near the boron proton dripline, in this case). This method further assumes that transmission and acceptance are sufficiently smooth that experimental inefficiencies do not mimic physical holes.

Isomer Tagging via γ-Ray Coincidences

When germanium detectors are available, isomeric decays provide unambiguous isotope identification. Coincidences between PID-selected fragments and characteristic γ rays – combined with known half-lives and decay schemes – directly link a PID blob to a specific nuclide. This method is independent of optics modeling and serves as a definitive validation of blob assignments.

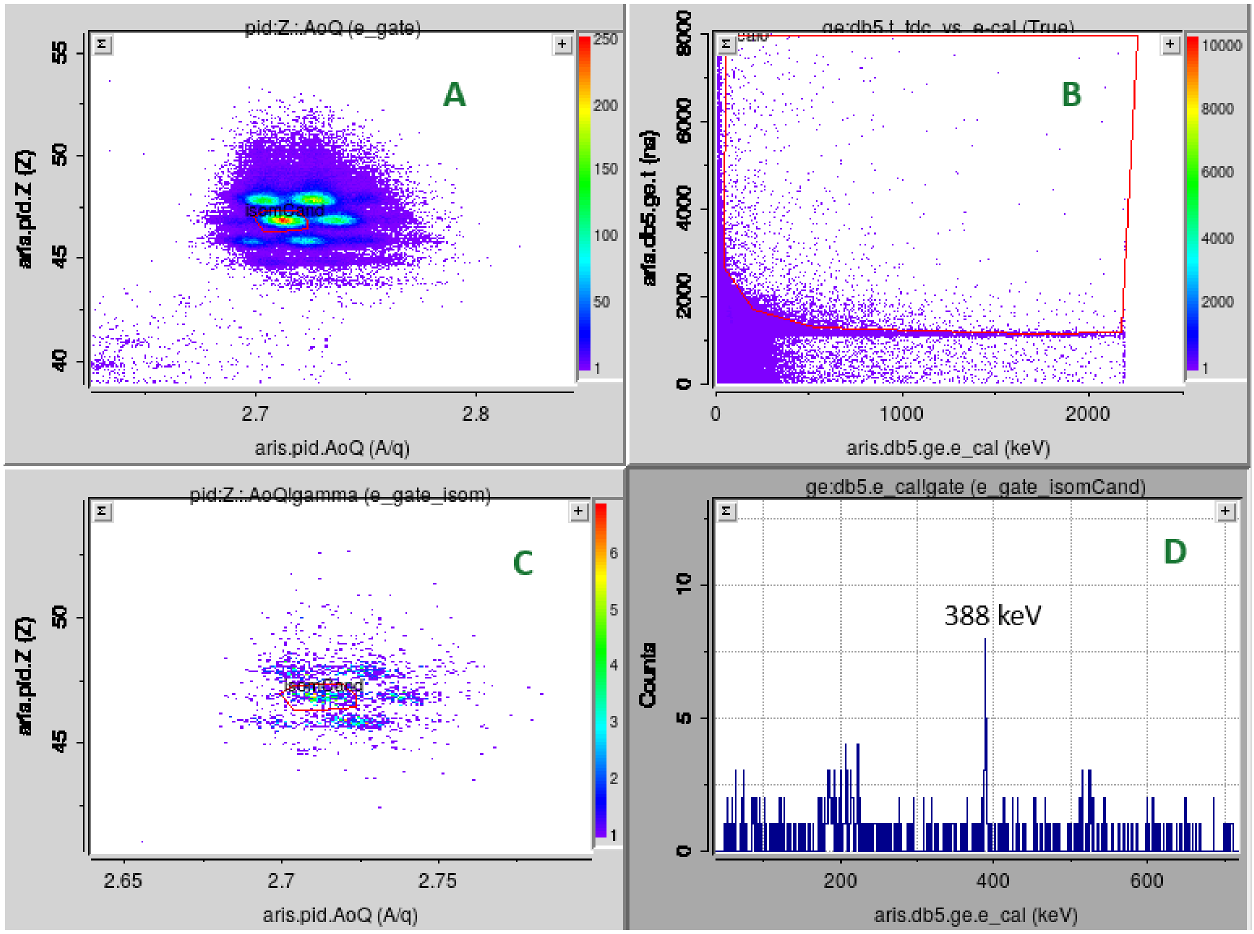

Figure 52: Example of the isomer PID process. Clockwise from top left: (A) finalized and cleaned PID. (B) Germanium detector's registered energy vs time. (C) Isomer gate projected onto PID spectrum. (D) One-dimensional γ-energy spectrum with cleaning and blob gate applied.

Figure 52 shows an example workflow for isomer identification. The analysis starts with a well-resolved PID spectrum (A/q vs Z, Fig. 52, **A**) that has preliminary cleaning gates applied to it. It is important to note that positive isomer identification will *not* identify charge-states, as the isomer is indifferent to the number of electrons orbiting the nucleus[40].

After a high-quality PID spectrum has been made, create a gamma-ray gate (Fig. 52, **B**). This ungated spectrum plots the germanium detector's registered energy vs time. The gate is drawn such that prompt gammas and background are excluded.

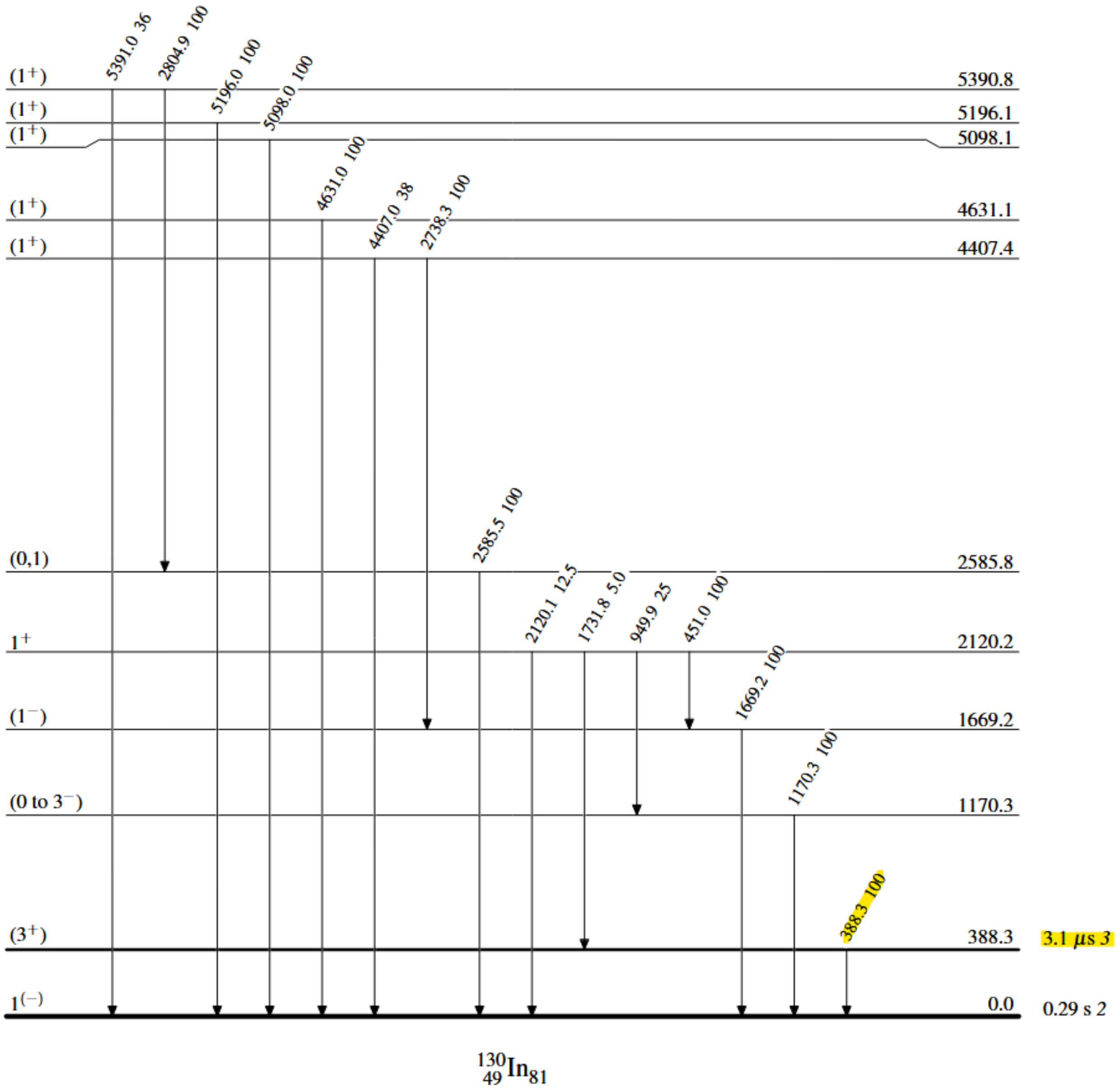

Figure 53: ^{130}In gamma-ray level scheme from the NNDC ENSDF. The detected isomeric state is highlighted.

This isomer gate is then projected back onto the PID plot (Fig. 52, **C**). Candidate iso-

---

[40] This isn't strictly true: for isotopes with a large branching ratio for internal conversion, higher charge-states may impact gamma-ray statistics and mask the identity of the fragment. Consequently, isomer tagging confirms the nuclear identity (A, Z), but does not, by itself, resolve the ionic charge-state.

topes are the remaining bright spots. Gate these with a temporary name (e.g., “isomCand”) and project the corresponding gamma-rays onto a one-dimensional energy spectrum. Sharp peaks with more counts than background are likely the isomeric decays. These gamma energies are compared to known isomers[41] in the region of interest. The isomer detected has an energy of 388 keV. The spectrometer was tuned for ^{130}In, which has a known isomer of that energy. The gamma-ray energy levels are shown in Figure 53. The highlights show the energy and half-life of the state. With this gamma-ray detection, we have confirmed the identity of the gated blob, and may fix the remaining PID accordingly.

The process may also be run in reverse: start with the one-dimensional gamma energy spectrum, gate on large peaks, project those gates onto the PID spectrum and see which, if any, blobs are strong emitters. This method is usually used in regions where isomers are known to exist and be populated (e.g., the strong ^{88}Br 110.9 kev gamma ray).

Important considerations when looking for potential isomeric states is to be aware of the half-life and angular momentum of the decaying state. Isomer tagging is only effective for states with lifetimes comparable to or longer than the flight time from the target to the focal plane (∼550 ns). Similarly, isomers with very large angular momenta are not expected to be populated in great numbers during the fragmentation.

If isomers prove hard to identify, some recommended steps are to change the number of bins in the one-dimensional energy spectrum to potentially resolve multiple overlapping peaks that might conspire together to populate multiple blobs or combine peaks to boost the counts. Additionally, one may change the placement of the isomer gate – if there is too much background, bring the gate up, if there is too few counts, place the gate closer to the prompt gamma blob.

In extremely exotic regions of the nuclear chart, previously unreported isomers may be observed. Unexpected peaks should therefore be investigated carefully rather than dismissed outright.

Once positive isotopic identification has been made, the remaining calibration of the PID may proceed.

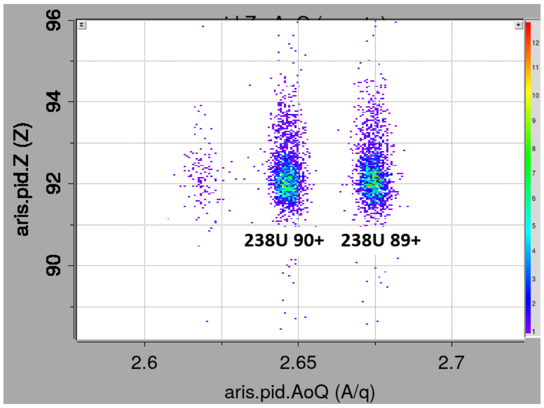

Figure 54: Example of detector calibration and PID using the charge-states of the primary beam (^{238}U).

Primary and Pilot Beam Calibration

Fragments with well-known properties, including the primary beam itself or reference cocktail components, are used to establish absolute calibration of energy-loss, time-of-flight, and magnetic rigidity, including any kinematic or dispersion-dependent corrections applied in the optics model. These anchors validate the PID reconstruction defined by Equations (26)–(31) and ensure that at least one location in PID

---

[41] It is recommended to use the LISE isomer database or the NNDC ENSDF: https://www.nndc.bnl.gov/ensdf/

space is known with certainty. All other assignments are made relative to this calibrated reference.

Figure 54 shows a PID calibration centered around charge-states of the primary beam (^{238}U). The calculated A/q and Z values must match the known cocktail. Once the detectors are calibrated on the primary beam, the secondary fragments may be transmitted and PID may be confirmed.

In a similar manner, a pilot beam, which ideally has characteristics similar to the desired rare isotope beam may be transmitted and calibration performed based on it.

E.6.2 Secondary (Corroborative) Identification Methods

The following methods do not uniquely identify isotopes on their own, but provide strong supporting evidence and consistency checks once at least one anchor has been established.

Isotopic Chain Continuity

Within a given element, isotopes populate smooth, approximately linear trajectories in PID space (e.g., A/q vs. Z, or $A - 3Z$ projections). After anchoring one isotope, neighboring blobs are assigned by continuity, with approximately uniform spacing corresponding to $\Delta A = 1$. Abrupt deviations from these trends often indicate misidentification, contamination, or miscalibration. This is especially diagnostic when comparing neutron-rich and proton-rich sides of the same element.

Comparison to `LISE`$^{++}$ Yield Systematics

Relative fragment intensities may be compared to `LISE`$^{++}$-predicted production rates. While absolute agreement is not expected, the qualitative ordering of yields within an isotopic chain should be physically reasonable. Large discrepancies – such as an apparently exotic isotope being significantly more intense than its neighbors – are strong indicators of incorrect blob assignment. This method should never be used as a primary identifier, but only as a qualitative consistency check once at least one isotope has been anchored experimentally.

In the example presented in Figure 55, the pattern of the relative intensity is compared between experiment and `LISE`$^{++}$ predictions. The cross checking of the observed intensity pattern can help verify that PID is correct.

Charge-State Behavior Consistency

Correct isotope assignments exhibit physically plausible charge-state distributions following total kinetic energy calibration. Fully stripped charge-states dominate at sufficiently high energies, while partially stripped states form predictable, lower-intensity branches. Unphysical behavior (e.g., $q > Z$ or isolated charge-states) signals misidentification or calibration failure. This check is particularly powerful when multiple charge-states of the same isotope are visible simultaneously and directly relies on the charge determination described in Equation (27).

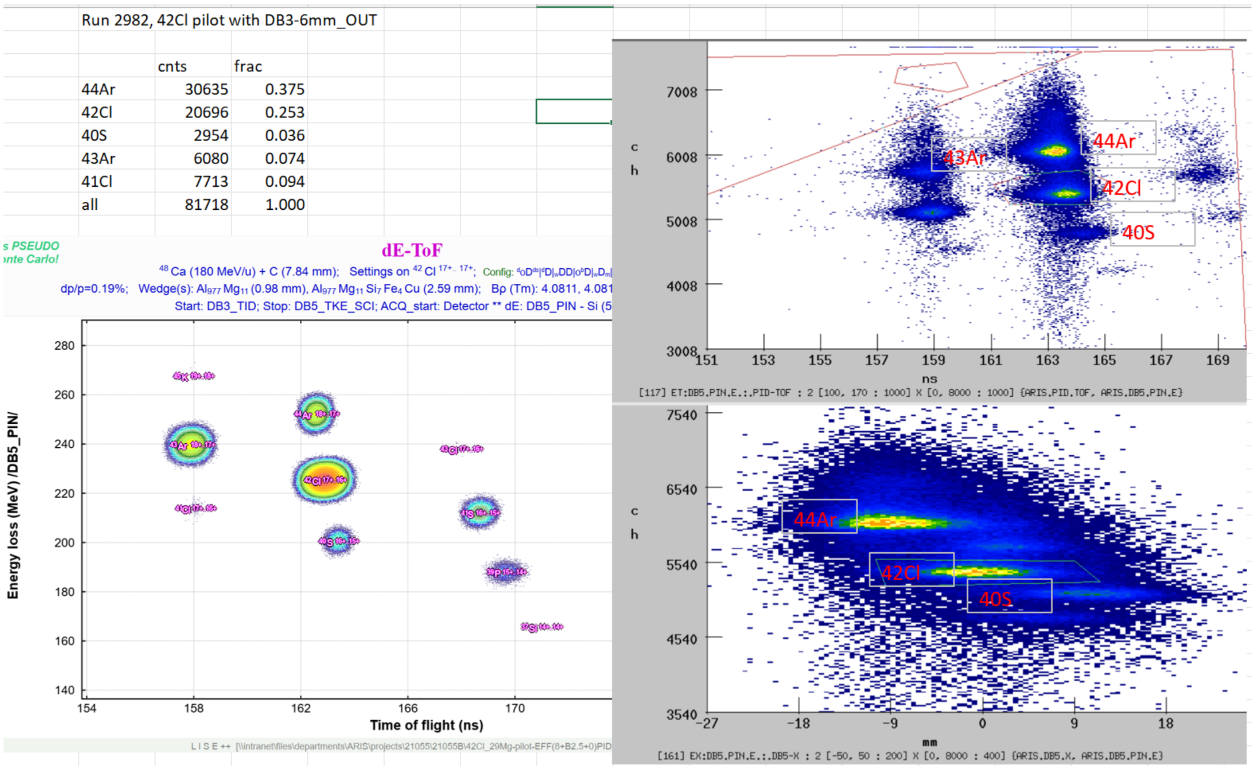

Run 2982, 42Cl pilot with DB3-6mm_OUT

	cnts	frac
44Ar	30635	0.375
42Cl	20696	0.253
40S	2954	0.036
43Ar	6080	0.074
41Cl	7713	0.094
all	81718	1.000

Figure 55: Example of a qualitative comparison of experimental yield to `LISE`$^{++}$-predicted yield.

Transport and Optical Consistency

Fragments correctly identified in PID space should behave consistently throughout the beamline. Correlations between position, angle, dispersion, and transmission across focal planes should align with expectations from ion-optical transport. Anomalous transmission or strong higher-order aberrations associated with a particular blob may indicate secondary reactions or incorrect identification.

E.6.3 Failure Modes and Best Practices

Purely visual alignment of PID blobs, unconstrained Gaussian fitting, or blind reliance on simulation-predicted centroids are insufficient for reliable identification. Assumptions such as $q = Z$ must always be validated experimentally, especially for high-Z beams where incomplete stripping is common.

Best practice is to establish at least one primary identification anchor, then apply multiple corroborative methods to confirm the full isotopic assignment. When ambiguities remain, conservative exclusion of questionable isotopes is preferable to propagating uncertain identifications into cross section results.

E.7 Summary and Recommended Workflow

Reliable particle identification requires a structured and conservative approach. Based on the principles outlined in this appendix, the recommended workflow is as follows:

- Establish and validate timing and magnetic-rigidity calibrations before attempting PID.
- Anchor at least one isotope using a primary identification method (primary beam, pilot beam, PID holes, or isomer tagging).
- Verify charge-state behavior and confirm that reconstructed q values are physically plausible.
- Use secondary methods (isotopic continuity, yield systematics, transport consistency) to corroborate assignments.
- When ambiguities remain, conservatively exclude questionable blobs rather than propagating uncertain identifications into yield or cross section results.

Following this workflow minimizes the risk of systematic PID errors and ensures that subsequent yield extraction and cross section analyses are physically meaningful and reproducible.

Appendix F Momentum Integrated Total Cross Section

As discussed in subsection 7.1, a distinction must be made between partial and total production cross sections. This appendix formalizes the procedure used to determine total production cross sections from experimentally measured partial cross sections.

A *partial cross section* is the production cross section measured at a single magnetic rigidity setting. Because a given $B\rho$ selects a narrow interval in longitudinal momentum, each partial measurement samples only a slice of the fragment's longitudinal momentum distribution. For a fixed fragment and charge state, larger $B\rho$ values correspond to fragments that retain more longitudinal momentum (i.e., that have dissipated less energy in the reaction).

The *total production cross section* integrates over the full longitudinal momentum distribution of the fragment and is therefore independent of the specific separator tuning:

$$\sigma_{\mathrm{tot}} = \int \sigma(P) d(P). \tag{32}$$

For rare isotopes, the total cross section is the physically meaningful observable: it determines absolute production rates and provides a direct benchmark for reaction models.

Physical Motivation

In projectile fragmentation, separators such as ARIS transmit only a limited $B\rho$ acceptance at a time. Consequently, the yield measured at any single setting represents only a fraction of the total production. Determining the total cross section therefore requires:

1. Measuring partial cross sections at multiple $B\rho$ settings.

2. Reconstructing the fragment's momentum distribution.
3. Integrating that distribution over momentum.

The magnetic rigidity,

$$B\rho = \frac{p}{q},$$

provides the link between separator settings and fragment kinematics. For fixed charge state q, varying $B\rho$ scans the longitudinal momentum distribution. Low-$B\rho$ settings probe the low-momentum tail; high-$B\rho$ settings probe the high-momentum tail. Near the centroid, transmission is typically largest and most stable; toward the tails, acceptance effects and model sensitivity increase.

The shape of the momentum distribution reflects underlying reaction dynamics, including Fermi motion, abrasion recoil, evaporation, and target energy-loss effects. Deviations from Gaussian behavior—such as asymmetry or enhanced tails—may indicate additional reaction mechanisms. Thus, a $B\rho$ scan is not only required for integration, but also provides diagnostic information about the reaction mechanism.

Model Dependence

`LISE`$^{++}$ includes several parameterizations of projectile-fragmentation momentum distributions, most commonly the Universal Parameterization [19]. During partial cross section extraction, the assumed momentum distribution determines the calculated transmission and therefore directly affects the reported cross section. Partial cross sections are therefore inherently model-dependent.[42]

One purpose of the total cross section analysis is to test whether the assumed momentum distribution reproduces the experimentally measured yields across the $B\rho$ scan.

Fitting and Integration Procedure

For fragments with sufficient transmission, partial cross sections measured at multiple $B\rho$ settings are fit to a parameterized momentum distribution. In practice:

- The vertical error bars reflect the propagated uncertainties from partial cross section analysis.
- The horizontal error bars represent the spectrometer's momentum acceptance at each setting.

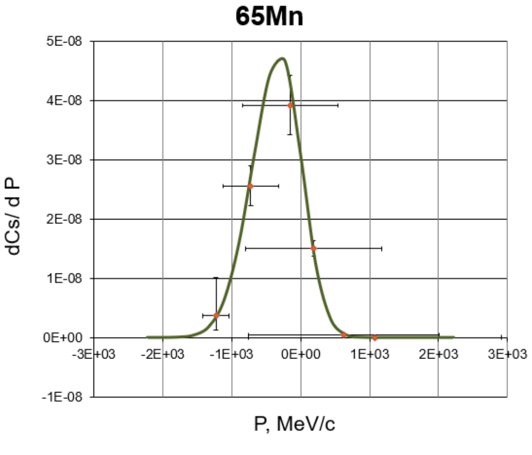

Figure 56: Example of a fitted momentum distribution from six partial cross section measurements.

---

[42] Advanced users may vary the momentum model or adjust Universal Parameterization parameters during analysis.

The fit is performed using a dedicated Excel workbook (Figure 57), which incorporates the cross section uncertainties determined earlier in the analysis chain.

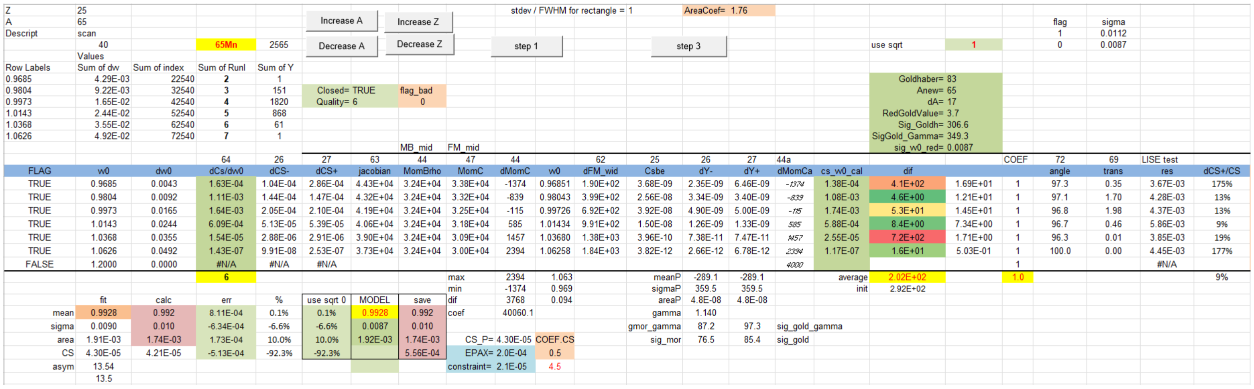

Z 25
A 65
Descript scan
40 65Mn 2565
stdev / FWHM for rectangle = 1
AreaCoef= 1.76

Row Labels	Sum of dw	Sum of index	Sum of RunI	Sum of Y
0.9685	4.29E-03	22540	2	1
0.9804	9.22E-03	32540	3	151
0.9973	1.65E-02	42540	4	1820
1.0143	2.44E-02	52540	5	868
1.0368	3.55E-02	62540	6	61
1.0626	4.92E-02	72540	7	1

Closed= TRUE
Quality= 6
flag_bad 0

flag	sigma
1	0.0112
0	0.0087

use sqrt 1

Goldhaber= 83
Anew= 65
dA= 17
RedGoldValue= 3.7
Sig_Goldh= 306.6
SigGold_Gamma= 349.3
sig_w0_red= 0.0087

							MB_mid	FM_mid															
			64	26	27	63	44	47	44		62	25	26	27	44a				COEF	72	69	LISE test	
FLAG	w0	dw0	dCs/dw0	dCS-	dCS+	jacobian	MomBrho	MomC	dMomC	w0	dFM_wid	Csbe	dY-	dY+	dMomCa	cs_w0_cal	dif			angle	trans	res	dCS+/CS
TRUE	0.9685	0.0043	1.63E-04	1.04E-04	2.86E-04	4.43E+04	3.24E+04	3.38E+04	-1374	0.96851	1.90E+02	3.68E-09	2.35E-09	6.46E-09	-1374	1.38E-04	4.1E+02	1.69E+01	1	97.3	0.35	3.67E-03	175%
TRUE	0.9804	0.0092	1.11E-03	1.44E-04	1.47E-04	4.32E+04	3.24E+04	3.32E+04	-839	0.98043	3.99E+02	2.56E-08	3.34E-09	3.40E-09	-839	1.08E-03	4.6E+00	1.21E+01	1	97.1	1.70	4.28E-03	13%
TRUE	0.9973	0.0165	1.64E-03	2.05E-04	2.10E-04	4.19E+04	3.24E+04	3.25E+04	-115	0.99726	6.92E+02	3.92E-08	4.90E-09	5.00E-09	-115	1.74E-03	5.3E+01	1.45E+01	1	96.8	1.98	4.37E-03	13%
TRUE	1.0143	0.0244	6.09E-04	5.13E-05	5.39E-05	4.06E+04	3.24E+04	3.18E+04	585	1.01434	9.91E+02	1.50E-08	1.26E-09	1.33E-09	585	5.88E-04	8.4E+00	7.34E+00	1	96.7	0.46	5.86E-03	9%
TRUE	1.0368	0.0355	1.54E-05	2.88E-06	2.91E-06	3.90E+04	3.24E+04	3.09E+04	1457	1.03680	1.38E+03	3.96E-10	7.38E-11	7.47E-11	1457	2.55E-05	7.2E+02	1.71E+00	1	96.3	0.01	3.85E-03	19%
TRUE	1.0626	0.0492	1.43E-07	9.91E-08	2.53E-07	3.73E+04	3.24E+04	3.00E+04	2394	1.06258	1.84E+03	3.82E-12	2.66E-12	6.78E-12	2394	1.17E-07	1.6E+01	5.03E-01	1	100.0	0.00	4.45E-03	177%
FALSE	1.2000	0.0000	#N/A	#N/A	#N/A										4000				1			#N/A	
			6									meanP	-289.1	-289.1		average	2.02E+02		1.0				9%

	fit	calc	err	%	use sqrt 0	MODEL	save
mean	0.9928	0.992	8.11E-04	0.1%	0.1%	0.9928	0.992
sigma	0.0090	0.010	-6.34E-04	-6.6%	-6.6%	0.0087	0.010
area	1.91E-03	1.74E-03	1.73E-04	10.0%	10.0%	1.92E-03	1.74E-03
CS	4.30E-05	4.21E-05	-5.13E-04	-92.3%	-92.3%		5.56E-04
asym	13.54						
	13.5						

max 2394 1.063
min -1374 0.969
dif 3768 0.094
coef 40060.1
CS_P= 4.30E-05 COEF.CS
EPAX= 2.0E-04 0.5
constraint= 2.1E-05 4.5

sigmaP 359.5 359.5
areaP 4.8E-08 4.8E-08
gamma 1.140
gmor_gamma 87.2 97.3 sig_gold_gamma
sig_mor 76.5 85.4 sig_gold
init 2.92E+02

Figure 57: Excel workbook used to fit the momentum distribution from the partial cross section measurements.

To stabilize the fit and maintain physical consistency, it is recommended to fix either the centroid or the width of the distribution using established systematics (e.g., Morrissey [41], Goldhaber [42], or the Universal Parameterization), and fit the remaining parameters. This prevents over-fitting and facilitates quantitative comparison with reaction models.

The total production cross section is then obtained by integrating the fitted distribution over momentum.

Practical Constraints and Limitations

Only fragments with sufficiently high transmission should be used for total cross section determination. When transmission is very small, the extracted partial cross sections become highly sensitive to simulated optical conditions, leading to large propagated uncertainties. A reliable total cross section requires controlled and well-understood transmission corrections across the scan.

Target thickness also directly affects the momentum distribution through energy-loss, straggling, and reaction-depth effects. A change in target thickness effectively changes the phase space being sampled and should be treated as a separate experimental condition.

Operational Insight

Empirically locating the centroid of the measured momentum distribution provides immediate operational guidance. If measured partial cross sections do not peak near the chosen $B\rho$ setting (as in Figure 56), beam tuning can be adjusted to maximize production of the isotope of interest. In this way, total cross section analysis informs both physics interpretation and separator optimization.

Notation and Terminology Reference

This supplemental reference summarizes the symbols, variables, and terminology used throughout this manual. The goal is to provide a quick reference for new practitioners of fragmentation analysis.

Mathematical and Physical Notation

Symbol	Definition
$B\rho$	Magnetic rigidity of a charged particle in a magnetic field
p	Fragment momentum along the optical axis
q	Ionic charge state of the fragment
β	Velocity in units of the speed of light, $\beta = v/c$
γ	Lorentz factor, $\gamma = 1/\sqrt{1-\beta^2}$
A	Mass number (total nucleons)
Z	Atomic number (proton number)
A/q	Mass-to-charge ratio reconstructed from ToF and $B\rho$
ΔE	Measured energy loss in detector material
ToF	Time-of-flight between two points along the beamline (DB3-5)
$\sigma(B\rho)$	Partial production cross section at a given magnetic rigidity
σ_{tot}	Momentum-integrated total production cross section
ξ	Simulated transmission through the separator
$\Delta\sigma$	Uncertainty in a cross section measurement

Key Relationships

Magnetic rigidity connects fragment kinematics to separator settings:

$$B\rho = \frac{p}{q}.$$

Throughout this manual, the term "momentum distribution" refers specifically to the longitudinal momentum distribution (along the optical axis of the separator).

The total production cross section is obtained by integrating the momentum-dependent partial cross sections:

$$\sigma_{\text{tot}} = \int \sigma(B\rho)\, d(B\rho),$$

where the integration spans the full transmitted momentum range of the fragment.

Glossary of Terms

Abrasion-ablation model: A theoretical description of projectile fragmentation. In the abrasion stage, nucleons are removed from the projectile during the collision. In the ablation stage, the excited pre-fragment cools by evaporating light particles.

Acceptance: The range of phase space (momentum and angle) transmitted by the separator at a given optics setting.

Atomic number (Z): The number of protons in the nucleus. Determines the chemical element.

Charge state (q): The net ionic charge of a fragment after passing through the target and degraders. Fully stripped ions have $q = Z$.

Cross section: A measure of the probability that a specific reaction produces a given fragment. It has units of area (typically millibarns).

Energy loss (ΔE): The energy deposited by a charged particle as it passes through detector material. Used to determine atomic number.

Fragment separator: A magnetic system (e.g., ARIS) that selects reaction products based on magnetic rigidity and transports them to a focal plane.

Focal plane: A location in the separator where particles with a given magnetic rigidity are spatially focused and measured.

Magnetic rigidity ($B\rho$): The product of magnetic field strength and bending radius. Determines which momentum-to-charge ratio is transmitted by the separator.

Momentum distribution: The distribution of longitudinal momenta of a fragment species produced in a reaction.

Partial cross section ($\sigma(B\rho)$): The production cross section measured at a single magnetic rigidity setting.

PID (Particle Identification): The procedure used to determine A, Z, and q from measured observables such as time-of-flight and energy loss.

Production rate: The number of fragments produced per unit time. Proportional to beam intensity, target thickness, transmission, and cross section.

Total production cross section (σ_{tot}): The cross section integrated over the full longitudinal momentum distribution of the fragment.

Transmission: The fraction of produced fragments that are transported through the separator and detected.

Time-of-flight (ToF): The time required for a fragment to travel between two timing detectors. Used to determine velocity.

Units

Unless otherwise stated:

- Cross sections are reported in millibarns (mb).
- Magnetic rigidity is reported in T·m.
- Momentum is expressed in MeV/c when needed.

Conceptual Distinction

It is important to distinguish between:

- $\sigma(B\rho)$ – what is directly measured at a given optics setting.
- σ_{tot} – the physics observable independent of separator tuning. This is obtained by integrating over the longitudinal momentum of the fragment.

The former depends on transmission and model assumptions; the latter represents the intrinsic production probability in the reaction.

FAQ

- **Why do we care about total cross sections if the experiment only runs at one $B\rho$ setting?**

  A partial cross section, $\sigma(B\rho)$, measures only the fraction of the fragment momentum distribution transmitted at that specific magnetic rigidity. It therefore depends on the separator tuning. The total cross section, σ_{tot}, represents the intrinsic production probability of the fragment in the reaction and is independent of optics settings. Even if an experiment runs at a single $B\rho$, understanding how that measurement relates to the full distribution is essential for interpreting production rates and comparing to models.

- **Why are partial cross sections model dependent?**

  Extraction of $\sigma(B\rho)$ requires correcting for transmission. Transmission calculations depend on an assumed momentum distribution model (e.g., Universal Parameterization). Because that model influences the calculated fraction of fragments transmitted through the separator, the resulting partial cross section is not purely experimental – it carries implicit model assumptions.

- **Why can't we determine charge state from γ-ray tagging?**

  Delayed γ-rays uniquely identify the nuclear species (A, Z) but do not determine the ionic charge state q. Different charge states of the same isotope produce identical γ-ray spectra. The charge state must therefore be determined independently using kinematic observables such as $B\rho$, time-of-flight, and total kinetic energy.

- **What physical processes determine the width of the momentum distribution?**

  The width reflects several contributions: Fermi motion of nucleons in the projectile, recoil and friction from the abrasion process, evaporation of particles during de-excitation, and energy-loss effects in the target. Models such as Goldhaber and Morrissey provide systematics relating the width to the number of removed nucleons.

- **Why does the target thickness change the momentum distribution shape?**

  A thicker target increases energy loss and energy-loss straggling. Fragments are produced at different depths within the target, leading to variations in post-reaction energy and momentum. As a result, the centroid may shift and the width may broaden. Changing target thickness effectively changes the observed momentum distribution.

- **How do I know if my PID is "good enough"?**

  A reliable PID spectrum shows clear separation between neighboring isotopes, minimal overlap, and stable centroids across runs. Background within gates should be small compared to signal. If blob boundaries are ambiguous or strongly dependent on small gate adjustments, the PID calibration should be revisited.

- **When should a cross section be omitted from a data set?**

  - Transmission is extremely low and highly model sensitive.
  - Charge state assignment is ambiguous.
  - Background dominates signal within the gate.
  - Uncertainties exceed the physical meaning of the result.

  These conditions are usually fulfilled by isotopes at the edge of the separator acceptance or those dominated by contamination from wedge reactions or high-order optical aberrations.

- **Why do different charge states sometimes have different apparent widths?**

  Different charge states experience slightly different energy-loss histories and transmission efficiencies. Acceptance effects can also differ across charge states. As a result, reconstructed momentum widths may vary even for the same isotope. This is particularly true of species whose charge state changed via reactions in detector or wedge materials.

- **Why does my total cross section change when I include or exclude one data point?**

  Momentum distribution fits, especially in sparsely sampled tails, can be sensitive to individual points. Data taken at low transmission or large uncertainty may disproportionately influence fitted parameters. Stability tests should be performed to ensure the result is not driven by a single measurement.

- **Why do horizontal error bars matter in longitudinal momentum fitting?**

  Each $\sigma(B\rho)$ point represents an average over a finite momentum acceptance, not a delta function at a single rigidity. Ignoring horizontal acceptance width can bias the fit, especially in regions where the distribution slope is steep.

- **Why does transmission uncertainty dominate the cross section uncertainty?**

  In nearly all fragmentation-based cross section measurements, the uncertainty associated with the transmission ξ dominates the total uncertainty budget. This is not an artifact of poor analysis practice; rather, it is a direct consequence of both the physics of fragment production and the practical limitations of modeling particle transport through a complex beamline.

  First, the transmission is not a directly measured quantity. Unlike the yield Y or the beam integral B_{int}, which are derived from experimentally recorded signals, ξ must be inferred from simulations. These simulations rely on an idealized description of the experimental setup, including material thicknesses, reaction models, charge-state distributions, and ion-optical properties. Even when carefully tuned, such models cannot fully capture the true, event-by-event complexity of fragment transport from the target to the final focal plane.

Second, transmission is intrinsically sensitive to many coupled parameters. Small changes in target thickness, wedge thickness, material defects, slit positions, or optical settings can alter angular acceptance, momentum acceptance, or charge-state survival probabilities. While each parameter may be known to within a few percent (or better), their combined effect on transmission is often nonlinear. As a result, even modest, physically reasonable parameter variations can lead to percent-level or larger changes in ξ for individual fragments.

Third, transmission effects are fragment dependent. Fragments near the center of the acceptance typically exhibit relatively stable transmission, while fragments near acceptance edges – such as those with extreme A/Z, large momentum offsets, or unusual charge-state populations – can show strong sensitivity to higher-order optics, material interactions, and secondary reactions. Consequently, the transmission uncertainty varies from isotope to isotope and must be evaluated individually, further increasing its contribution to the overall error.

In contrast, the other terms in the cross section equation are generally better constrained. Statistical uncertainties on the yield Y decrease rapidly with increasing counts and are often subdominant except for the rarest fragments. The target areal density N_t is usually measured with high precision, and its uncertainty is bounded by manufacturing tolerances and direct metrology. Similarly, the beam integral B_{int} benefits from long integration times and redundancy in power measurements, resulting in relatively small fractional uncertainties.

Finally, because the transmission enters multiplicatively in the denominator of Equation (15), any fractional uncertainty in ξ directly propagates to the same fractional uncertainty in the cross section. When $\Delta\xi/\xi$ is at the 5–15% level, it will exceed the combined contribution of all other uncertainty sources.

For these reasons, the transmission uncertainty sets the ultimate precision limit of most cross section measurements. A careful, physically motivated transmission analysis, coupled with conservative but reasonable uncertainty estimates, is therefore the most critical component of a credible cross section result.

- **How many $B\rho$ points are enough for a total cross section?**

  At minimum, three points are required to constrain a Gaussian shape. Five to seven points provide better stability and allow detection of asymmetries. The number should balance beam time constraints with fitting reliability.

- **Why does transmission drop quickly in the low-momentum tail?**

  Fragments in the low-momentum tail often have larger angular spreads and greater correlation between angle and momentum. Optical aberrations and slit limitations reduce transmission efficiency away from the central rigidity.

- **Why are the longitudinal momentum distributions asymmetric?**

The longitudinal momentum distribution has an asymmetric low-energy tail because of the energy-loss straggling in the target material as well as friction and dissipative forces that occur during the abrasion process. These conspire to elongate the low-energy tail. Conversely, there are no known effects that broaden the high-energy tail, which is generally assumed to follow a Gaussian taper.

- **What assumptions underlie this entire analysis chain?**

  The analysis assumes:

  - Clean and stable PID separation.
  - Accurate optics modeling and transmission calculations.
  - Valid momentum distribution parameterization.
  - Reliable beam normalization and target thickness measurement.
  - Proper detector calibration.

- **Kinematic corrections don't seem to enhance the A/q resolution. What's going on?**

  Kinematic corrections improve resolution only if kinematic broadening is a dimonant contribution to the observed width. If the reconstructed A/q peak is already dominated by other effects – such as timing resolution, detector position resolution, higher-order optical aberrations, or charge-state mixing – then correcting for trajectory-dependent path length or angle will produce little visible improvement.

  In practice, this usually means one of the following things:

  1. The optics are already well-tuned. If path length variations across the acceptance are small, the additional resolution gained is marginal.
  2. Resolution is detector-limited. If ToF or position resolution dominates the width, kinematic corrections cannot recover information that was never measured precisely.
  3. The correction is improperly applied. If correlations between position and reconstructed momentum are weak or incorrectly parameterized, the applied correction may not target the true source of broadening.
  4. PPAC performance is degraded by high rates Position-sensitive detectors such as PPACs can be significantly affected by large rates of light-Z fragments. These fragments often have much higher production rates and can:

     - Increase baseline noise and electronics pile-up,
     - Reduce effectivel signal-to-noise ratio,
     - Distort timing or position signals,
     - Intorduce event-by-event jitter.

     When PPAC signals are degraded in this way, reconstructed positions and angles become noisier. Since kinematic corrections rely directly on accurate position and angle measurements, degraded PPAC performance can wash out any potential improvement in A/q resolution.

A useful diagnostic is to examine correlations between reconstructed A/q and dispersive position. If no clear correlation exists before correction, then little improvement should be expected.

In short: kinematic corrections can only improve resolution if the dominant broadening mechanism is geometric. If detector noise or high-rate effects (such as PPAC saturation from light fragments) dominate, little improvement should be expected. Retuning the beam or tightening slits can reduce the rate of light-Z fragments and can consequently increase the fidelity of the PID.

- **Why does unit slope of reconstructed momentum between optical segments indicate good reconstruction?**

  In a properly reconstructed separator, the fragment momentum determined in one optical segment should match the momentum reconstructed in a downstream segment, apart from well-understood energy losses.

  If you plot reconstructed momentum in segment 3 versus reconstructed momentum in segment 1, a unit slope indicates:

  - Transfer matrices are correctly applied.
  - Position and angle measurements are properly calibrated.
  - The optics model accurately describes the beam transport.
  - No artificial scaling or distortion has been introduced during reconstruction.

  A slope different from unity suggests a systematic scaling error. For example:

  - Slope > 1 may indicate overestimation of dispersion.
  - Slope < 1 may indicate incorrect magnetic field normalization.
  - Nonlinear deviations may indicate higher-order optical aberrations.

  In short, unit slope means that the same physical quantity (momentum) is being reconstructed consistently in both segments. It is a strong internal consistency check of the optics model and calibration.

References

[1] M. Hausmann et al., “Design of the advanced rare isotope separator ARIS at FRIB,” Nuclear Instruments and Methods in Physics Research Section B: Beam Interactions with Materials and Atoms **317**, 349–353 (2013).

[2] M. Portillo et al., “Commissioning of the advanced rare isotope separator ARIS at FRIB,” Nuclear Instruments and Methods in Physics Research Section B: Beam Interactions with Materials and Atoms **540**, 151–157 (2023).

[3] S. Di Carlo and M. Cortesi, “Parallel-plate avalanche counters for heavy-ion beam tracking: history and mysteries,” Phys. Rev. Accel. Beams **27**, 044801 (2024).

[4] H. Kumagai et al., “Development of parallel plate avalanche counter (PPAC) for BigRIPS fragment separator,” Nuclear Instruments and Methods in Physics Research Section B **317**, 97–107 (2013).

[5] O. B. Tarasov et al., “Discovery of new isotopes in the fragmentation of ^{82}Se and insights into their production,” Phys. Rev. C **112**, 034604 (2025).

[6] O. B. Tarasov, *Quantifying Detector Contributions to PID Resolution in Rare-Isotope Experiments*, Workshop presentation, Workshop on New Generations of Detector and Data Aquisition Systems for Nuclear Physics, East Lansing, MI USA, 2025.

[7] M. Bowry et al., “Abrasion-fission reactions at intermediate energies,” Phys. Rev. C **108**, 034604 (2023).

[8] K. Sümmerer and B. Blank, “Modified empirical parametrization of fragmentation cross sections,” Phys. Rev. C **61**, 034607 (2000).

[9] K. Sümmerer, “Improved empirical parametrization of fragmentation cross sections,” Phys. Rev. C **86**, 014601 (2012).

[10] G. J. Feldman and R. D. Cousins, “Unified approach to the classical statistical analysis of small signals,” Phys. Rev. D **57**, 3873–3889 (1998).

[11] H. Suzuki et al., “Discovery of new isotopes ^{81,82}Mo and ^{85,86}Ru and a determination of the particle instability of $^{\mathbf{103}}$**Sb**,” Phys. Rev. C **96**, 034604 (2017).

[12] O. Tarasov and D. Bazin, “Development of the program LISE: application to fusion–evaporation,” Nuclear Instruments and Methods in Physics Research Section B: Beam Interactions with Materials and Atoms **204**, 174–178 (2003).

[13] O. Tarasov and D. Bazin, “LISE++: radioactive beam production with in-flight separators,” Nuclear Instruments and Methods in Physics Research Section B: Beam Interactions with Materials and Atoms **266**, 4657–4664 (2008).

[14] O. Tarasov and D. Bazin, “LISE++: exotic beam production with fragment separators and their design,” Nuclear Instruments and Methods in Physics Research Section B: Beam Interactions with Materials and Atoms **376**, 185–187 (2016).

[15] O. Tarasov et al., “LISE cute++, the latest generation of the LISE ++ package, to simulate rare isotope production with fragment-separators,” Nuclear Instruments and Methods in Physics Research Section B: Beam Interactions with Materials and Atoms **541**, 4–7 (2023).

[16] O. B. Tarasov et al., “Production cross sections from ^{82}Se fragmentation as indications of shell effects in neutron-rich isotopes close to the drip-line,” Phys. Rev. C **87**, 054612 (2013).

[17] M. Mocko et al., “Projectile fragmentation of ^{40}Ca, ^{48}Ca, ^{58}Ni, and ^{64}Ni at 140 MeV/nucleon,” Phys. Rev. C **74**, 054612 (2006).

[18] O. Tarasov et al., “A new approach to measure momentum distributions and production cross-sections of neutron rich nuclei using fragment separators,” Nuclear Instruments and Methods in Physics Research Section A: Accelerators, Spectrometers, Detectors and Associated Equipment **620**, 578–584 (2010).

[19] O. B. Tarasov, “Analysis of momentum distributions of projectile fragmentation products,” Nuclear Physics A **734**, 536–540 (2004).

[20] K. Haak, “Production of neutron-rich rare isotopes near N = 126 via medium energy fragmentation,” PhD thesis (Michigan State University, 2024).

[21] J. D. Bowman, W. J. Swiatecki, and C. F. Tsang, *Abrasion and Ablation of Heavy Ions*, tech. rep. (Lawrence Berkeley Laboratory, 1973).

[22] L. F. Oliveira, R. Donangelo, and J. O. Rasmussen, “Abrasion-ablation calculations of large fragment yields from relativistic heavy ion reactions,” Phys. Rev. C **19**, 826–833 (1979).

[23] J. W. Wilson, L. W. Townsend, and F. Badavi, “A semiempirical nuclear fragmentation model,” Nuclear Instruments and Methods in Physics Research Section B: Beam Interactions with Materials and Atoms **18**, 225–231 (1986).

[24] M. Wang, W. Huang, F. Kondev, and S. Naimi, “The AME 2020 atomic mass evaluation (ii). tables, graphs and references,” Chinese Physics C **45**, 536–540 (2021).

[25] S. Goriely, S. Hilaire, M. Girod, and S. Péru, “First gogny-hartree-fock-bogoliubov nuclear mass model,” Phys. Rev. Lett. **102**, 242501 (2009).

[26] J.-J. Gaimard and K.-H. Schmidt, “A reexamination of the abrasion-ablation model for the description of the nuclear fragmentation reaction,” Nuclear Physics A **531**, 709–745 (1991).

[27] L. Audirac et al., “Evaporation-cost dependence in heavy-ion fragmentation,” Phys. Rev. C **88**, 041602 (2013).

[28] O. B. Tarasov, *LISE++ v.17.17.53*, `LISE`$^{++}$ documentation, 2025.

[29] D. S. Ahn et al., “Location of the neutron dripline at fluorine and neon,” Phys. Rev. Lett. **123**, 212501 (2019).

[30] A. Gade and T. Glasmacher, “In-beam nuclear spectroscopy of bound states with fast exotic ion beams,” Progress in Particle and Nuclear Physics **60**, 161–224 (2008).

[31] B. A. Brown et al., “Motivations for early high-profile FRIB experiments,” Journal of Physics G: Nuclear and Particle Physics **52**, `10.1088/1361-6471/adb449` (2025).

[32] K. L. Brown, *A First- and Second-Order Matrix Theory for the Design of Beam Transport Systems and Charged Particle Spectrometers*, Stanford Linear Accelerator Center (1982).

[33] H. Wollnik, *Optics of charged particles* (Academic Press, 2021).

[34] D. C. Carey, *The optics of charged particle beams* (Harwood Academic Publishers, 1987).

[35] L. Bandura et al., “Fragment separator momentum compression schemes,” Nuclear Instruments and Methods in Physics Research Section A: Accelerators, Spectrometers, Detectors and Associated Equipment **645**, 182–186 (2011).

[36] V. Maradia et al., “Demonstration of momentum cooling to enhance the potential of cancer treatment with proton therapy,” Nature Physics **19**, `10.1038/s41567-023-02115-2` (2023).

[37] D. J. Morrissey and B. M. Sherrill, "In-Flight Separation of Projectile Fragments," in The euroschool lectures on physics with exotic beams, vol. i. (2004).

[38] M. Berz et al., "Reconstructive correction of aberrations in nuclear particle spectrographs," Phys. Rev. C **47**, 537–544 (1993).

[39] N. Fukuda et al., "Identification and separation of radioactive isotope beams by the BigRIPS separator at the RIKEN RI beam factory," Nuclear Instruments and Methods in Physics Research Section B: Beam Interactions with Materials and Atoms **317**, 323–332 (2013).

[40] O. B. Tarasov et al., "Production of very neutron-rich nuclei with a ^{76}Ge beam," Phys. Rev. C **80**, 034609 (2009).

[41] D. J. Morrissey, "Systematics of momentum distributions from reactions with relativistic ions," Phys. Rev. C **39**, 460–470 (1989).

[42] A. Goldhaber, "Statistical models of fragmentation processes," Physics Letters B **53**, 306–308 (1974).

Suggested Further Reading

The following list of references are recommended reading which supplements and augments the content of this manual. Note that this is in no way meant to be complete; if one desires a complete summary of low energy nuclear physics research, begin with L. Meitner and O. Hahn, "Products of the Fission of the Uranium Nucleus," Nature **143**, 471–472 (1939) and proceed chronologically!

[43] A. K. Anthony, C. Y. Niu, R. S. Wang, J. Wieske, K. W. Brown, Z. Chajecki, W. G. Lynch, Y. Ayyad, J. Barney, D. Bazin, and S. Beceiro-Novo, "Beam particle identification and tagging of incompletely stripped heavy beams with heist," Review of Scientific Instruments **93**, 013306 (2022).

[44] D. Bazin et al., "Radio frequency fragment separator at nscl," Nuclear Instruments and Methods in Physics Research Section A **606**, 314–323 (2009).

[45] J. R. Cummings et al., "Determination of the cross sections for the production of fragments from relativistic nucleus-nucleus interactions. i. measurements," Physical Review C **42**, 2508 (1990).

[46] M. de Jong et al., "Fragmentation cross sections of relativistic 208Pb projectiles," Nuclear Physics A **628**, 479–504 (1998).

[47] W. A. Friedman, "Heavy ion projectile fragmentation: a reexamination," Physical Review C **27**, 569 (1983).

[48] H. Geissel et al., "Ion-optical layout of a powerful next-generation pre-separator for in-flight separation of relativistic rare isotopes," Nuclear Instruments and Methods in Physics Research Section B **247**, 1–15 (2006).

[49] H. Geissel et al., “Ions penetrating through ion-optical systems and matter — non-liouvillian phase-space modelling,” Nuclear Instruments and Methods in Physics Research Section A **282**, 247–253 (1989).

[50] M. Giacomelli et al., “Projectilelike fragment emission angles in fragmentation reactions of light heavy ions in the energy region 200MeV/nucleon: modeling and simulations,” Physical Review C **69**, 064601 (2004).

[51] A. S. Goldhaber, “Statistical models of fragmentation processes,” Physics Letters B **53**, 306–308 (1974).

[52] R. Grzywacz et al., “Identification of μs-isomers produced in the fragmentation of a 112Sn beam,” Physics Letters B **355**, 439–444 (1995).

[53] K. Haak et al., “Production and discovery of neutron-rich isotopes by fragmentation of 198Pt,” Physical Review C **108**, 034608 (2023).

[54] C.-W. Ma et al., “Nuclear fragments in projectile fragmentation reactions,” Progress in Particle and Nuclear Physics **121**, 103911 (2021).

[55] P. N. Ostroumov et al., “Acceleration of uranium beam to record power of 10.4 kW and observation of new isotopes at facility for rare isotope beams,” Physical Review Accelerators and Beams **27**, 060101 (2024).

[56] R. Pfaff et al., “Projectilelike fragment momentum distributions from 86Kr + Al at 70 MeV/nucleon,” Physical Review C **51**, 1348 (1995).

[57] H. Suzuki et al., “Production cross section measurements of radioactive isotopes by BigRIPS separator at RIKEN RI beam factory,” Nuclear Instruments and Methods in Physics Research Section B: Beam Interactions with Materials and Atoms **317**, 756–768 (2013).

[58] H. Suzuki et al., “Discovery of 72Rb: a nuclear sandbank beyond the proton drip line,” Physical Review Letters **119**, 192503 (2017).

[59] O. B. Tarasov et al., “New isotope 44Si and systematics of the production cross sections of the most neutron-rich nuclei,” Physical Review C **75**, 064613 (2007).

[60] H.-L. Wei et al., “Cross-section prediction for isotopes near neutron drip line in 70, 80Zn projectile fragmentation reactions,” Chinese Physics C **43**, 074103 (2019).

[61] J. W. Wilson et al., “A semiempirical nuclear fragmentation model,” Nuclear Instruments and Methods in Physics Research Section B **18**, 95–134 (1987).

[62] D. J. Morrissey, W. R. Marsh, R. J. Otto, W. Loveland, and G. T. Seaborg, “Target residue mass and charge distributions in relativistic heavy ion reactions,” Phys. Rev. C **18**, 1267–1274 (1978).

[63] L. W. Townsend et al., *An Abrasion-Ablation Model Description of Galactic Heavy-Ion Fragmentation*, tech. rep. (NASA, 1984).

[64] J. Benlliure, K.-H. Schmidt, D. Cortina-Gil, T. Enqvist, F. Farget, A. Heinz, A. Junghans, J. Pereira, and J. Taieb, “Production of neutron-rich isotopes by cold fragmentation in the reaction 197Au + Be at 950 A MeV,” Nuclear Physics A **660**, 87–100 (1999).

[65] K.-H. Schmidt et al., “Proton removal in peripheral nuclear collisions at relativistic energies,” Nuclear Physics A **542**, 699–714 (1992).

Acknowledgments

This material is based upon work supported by the U.S. Department of Energy, Office of Science, Office of Nuclear Physics and used resources of the Facility for Rare Isotope Beams (FRIB) Operations, which is a DOE Office of Science User Facility under Award No. DE-SC0023633, and by the US National Science Foundation under Grants No. PHY-20-12040 and 23-10078 “Windows on the Universe: Open Quantum Systems in Atomic Nuclei at FRIB”.

I would like to thank the Rare Isotope Research Group and the ARIS Group. In particular, Oleg Tarasov, who was the driving force behind this manual.